SEARCH FOR THE HIGH-SPIN MEMBERS OF THE α:2n:α BAND IN ^{10}Be

A Dissertation

by

SRITEJA UPADHYAYULA

Submitted to the Office of Graduate and Professional Studies of
Texas A&M University
in partial fulfillment of the requirements for the degree of

DOCTOR OF PHILOSOPHY

Chair of Committee,	Grigory V. Rogachev
Committee Members,	Charles M. Folden III
	Jeremy W. Holt
	Dan G. Melconian
Head of Department,	Grigory V. Rogachev

May 2020

Major Subject: Physics

ABSTRACT

There is strong evidence that some states in ^{10}Be exhibit a molecular-like α:2n:α configuration. Based on theoretical studies, it appears that the 6.179 MeV 0^+ state in ^{10}Be has a pronounced α:2n:α configuration with an α-α inter-distance of 3.55 fm. This is 1.8 times more than the corresponding value for the ^{10}Be ground state. The 2^+ state at 7.542 MeV in ^{10}Be is believed to be the next member of this rotational band. The state at 10.2 MeV was identified as a 4^+ member in recent experiments. The algebraic model predicts that the next member of this band is the 6^+ state that should be found around 13 MeV.

An experiment was performed to search for the 6^+ state in ^{10}Be at around 13 MeV excitation energy in the excitation function for ^{6}He+α scattering, which populated states in the excitation energy range from 4.5 MeV to 8 MeV in ^{10}Be using a ^{6}He rare-isotope beam and a thick helium gas target. No new excited states in ^{10}Be have been observed. However, stringent limitation on the possible degree of α-clustering of the hypothetical yrast 6^+ state has been obtained using Monte Carlo methods. We concluded that the high-spin members of the α:2n:α molecular-like rotational band configuration, that is considered to have a 0^+ bandhead at 6.18 MeV, either do not exist or have small overlap with the ^{6}He(g.s.)+α channel.

To my parents and grandparents,

for their unwavering love and support.

ACKNOWLEDGMENTS

Although my name appears on the title page, this dissertation would not have been possible without the tireless efforts of my colleagues at the Cyclotron Institute. I owe a huge debt to my group members Drs. Evgeniy Koshchiy, Ethan Uberseder, Sunghoon (Tony) Ahn, Jack Bishop, Joshua Hooker and Heshani Jayatissa. They have all made significant contributions to my progress at one point or another. I am very thankful to Drs. Brian Roeder and Antti Saastamoinen for not only tuning the beam for my ^{10}Be project, but also for many meaningful discussions throughout my time at the Cyclotron Institute. I would like to express my gratitude to the staff at the Cyclotron Institute for helping sort out all the little details when needed and making me feel welcome here.

The largest influence on my work through out the years came from my superlative advisor, Prof. Grigory V. Rogachev (Grisha or ГРР). Grisha is one of the hardest-working, most dedicated and brilliant people I've had the privilege of meeting. I am very fortunate to have been under his tutelage. I could wax lyrical about Grisha to no end, but I'll simply say that he is a "typical" advisor. Those that understand what I mean by that will surely appreciate it.

Another important person without whom this would not have been possible is Dr. Heshani Jayatisa. She introduced me to Grisha, whose group I eventually joined, during a rather trying time in my graduate studies. In the same vein of importance, I acknowledge Dr. Josh Hooker. When I joined Grisha's group, Heshani and Josh created a positive, welcoming environment and showed me the ropes. It was a blast setting up for experiments and tearing things down after. We chased leaks, noise and segmentation faults alike together over the years. My analysis would not have progressed nearly as fast as it did without valuable guidance from Josh. I want to thank you two profusely!

I'd also like to acknowledge and thank my committee members - Profs. Cody Folden, Jeremy Holt and Dan Melconian. I would like to give special thanks to Dan for not only

serving on my committee, but also for his friendship over the years.

This large undertaking couldn't have been successful without the constant support of Dr. Evgeniy I. Koshchiy. Evgeniy's tenure in the group precedes mine. It is safe to say that he is the heart of the group. Not a single experimental campaign run by our group would have enjoyed any degree of success without Evgeniy's work. I am also very grateful to Dr. Ethan Uberseder. Ethan was yet another hard-working and inspiring figure in the group. He introduced me to many new computing concepts that I have not encountered before, including many SRE concepts. He is now enjoying much success in private industry and I wish him all the best. I've had many fruitful discussions with Dr. Vladilen Z. Goldberg (Vlad) over the years regarding my work. His knowledge of the subject and the interesting stories he told always made for fun conversations. I've always viewed him as my academic grandfather (since he's also Grisha's doctoral advisor). I wish Vlad all the best in his retirement.

Around the commissioning of TexAT, our group picked up a new important member - Dr. Sunghoon (Tony) Ahn. Tony has been very helpful in helping me with some of my analysis, as well as my cluster administration responsibilities. His calm demeanor also made him a good person to be around during times of stress. About a year and a half ago, Dr. Jack E. Bishop joined us from across the pond as a postdoc. He contributed to all aspects of my ^{10}Be analysis, including proofreading my manuscripts and offering valuable suggestions. Whilst I originally thought it was shared common interest in cluster physics that united us, I now realize it is in fact our fiery passion for T-Swizzle (Taylor Swift). I also owe Jack a huge debt for keeping me calm during my thesis writing and defense prep. Over the summer, we picked up a couple of stray physicists from the Cyclotron Institute (Dr. Cody Parker and Michael Roosa). Michael is a friend, neighbor and a like-minded vegan with similar values. I enjoyed doing some "light" vegan activism with him over the past year (Fight the power!). During the stressful time of writing this manuscript, Cody has gone out of her way to make sure I was taking care of myself, and eating well. She brought me home-made food and a

bag of assorted fruits from time to time.

Outside of my research group, I'd like to thank my friends who started graduate school with me... the friends with whom I spent many sleepless nights working on homework, studying for exams, or simply arguing about physics. Drs. Petr Zhokhov (who was also my roommate and Russian tutor/spy), Dawson Nodurft, Jacob Gayles, and many others; thank you for everything!

Midway through graduate school, I decided to cultivate a life outside the confines of the Mitchell Physics and Cyclotron Institute buildings, and picked up healthy cycling addiction. I want to thank all the people that have ridden with me over the years, specifically, Willie Allen, Eames Bennett, Danny Wright, and Profs. Edward Vargo and Christopher Menzel. Thank you for helping me stay sane through graduate school, and for many fun conversations over the long hours on the saddle.

I owe a debt of gratitude to Dr. Terrance O'Neill and Michael Montano at Riverside Community College for getting me interested in physics and Profs B.M.K. Nefkens for his mentorship while I was at UCLA.

Finally, my loving and encouraging family, I owe more than I can say for all the support they have given me over the years. Suryaprakash V. Upadhyayula (dad), Sridevi Upadhyayula (mom), Prof. Srigokul Upadhyayula (brother), and Dr. Jaclyn Lock (sister-in-law), your hard work and dedication has long served as an inspiration for me.

CONTRIBUTORS AND FUNDING SOURCES

Contributors

This work was supported by a dissertation committee consisting of Professor Grigory V. Rogachev [advisor] and Professors Jeremy W. Holt, Dan G. Melconian of the Department of Physics & Astronomy and Professor Charles M. Folden III of the Department of the Chemistry.

All other work conducted for the dissertation was completed by the student independently.

Funding Sources

Graduate study was supported by teaching assistantship from the Department of Physics & Astronomy and research assistantship from the Cyclotron Institute. The dissertation work was funded in part by the U.S. Department of Energy, Office of Science under Grant DE-FG92-93ER40773.

TABLE OF CONTENTS

Page

LIST OF FIGURES

FIGURE Page

LIST OF TABLES

TABLE Page

1. INTRODUCTION

Nuclear physics began with the discovery of radioactivity by Henri Becquerel in 1896 [1]. Radioactive decay is a stochastic process by which an unstable nucleus transitions to a lower energy state by decaying or disintegrating. The following year, J. J. Thomson discovered the electron, leading him to postulate the existence of an internal structure for an atom [2]. In 1904, the "plum pudding" model was put forth by Thomson, that described an atom as consisting of a positively-charged core with negatively-charged electrons that occupy the inside of the core. Following this, extensive understanding of radioactivity was elucidated by Thomson's student, Ernest Rutherford, by interpreting the results of the Geiger-Marsden experiment [3]. By the 1900s, they had discovered three types of radiation emerging from an atom. These were named α, β and γ respectively. By performing experiments with α-particles passing through air, foil and gold leaf, Rutherford conjectured that the atom consisted of a small, dense nucleus making up most of its mass. To balance out the overall charge to be neutral, a dense negatively-charged cloud of electrons orbit the nucleus. This, combined with the discovery of the neutron, allowed for a rudimentary understanding of the nuclear force [4, 5].

Our rudimentary understanding of the nucleus follows from Weizsäcker's liquid-drop model. The liquid-drop model is also able to predict the nuclear binding energies (the binding energy of a nucleus is the difference between the mass energy of the nucleus and its constituent nucleons) as well as the fission barrier. A representation of these three models is shown in Figure 1.1. To expand on this further, one must look at the semi-empirical mass formula, which can predict the binding energy of a nucleus [7]. The binding energy form is shown in Equation 1.1. The liquid-drop model assumes all the nucleons behave similar to droplets and just coalesce together to form a sphere.

$$E_B = a_V A - a_S A^{2/3} - a_c Z(Z-1)A^{-1/3} - a_{sym}\frac{(A-2Z)^2}{A} + \delta \tag{1.1}$$

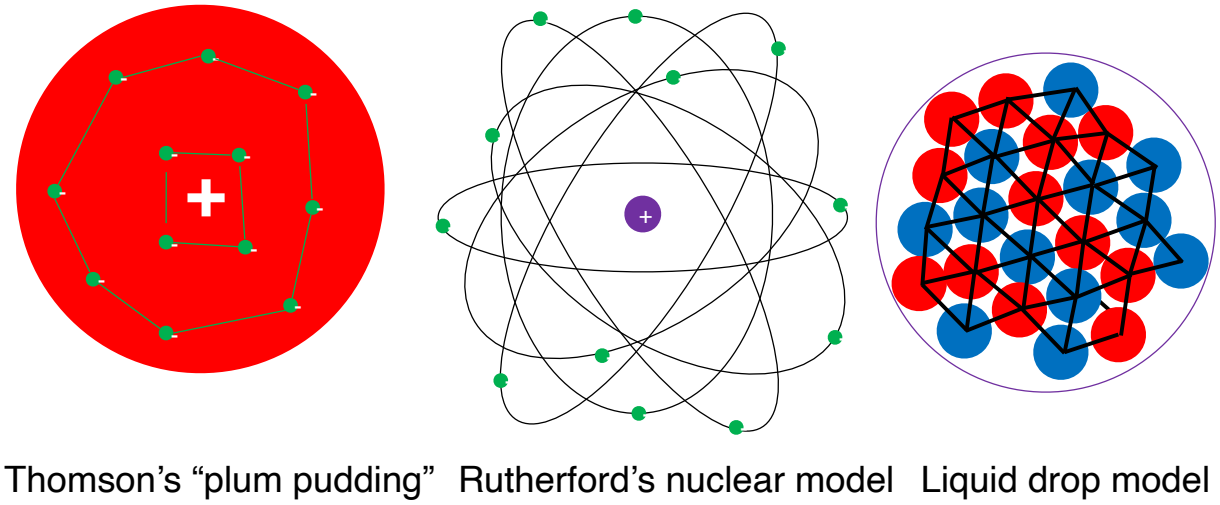

Figure 1.1: The evolution of the nuclear theory is shown here. The "plum pudding" model by Thomson described the nucleus as having a rather large positively charged core with negatively-charged electrons inside it. Rutherford's nuclear model comprised of a positively charged core that is rather small, being orbited by electrons. The last iteration of this is the liquid drop model. This model gave us a rudimentary understanding of the atom. This model is able to reconstruct nuclear binding energies as well as the fission barrier. Reprinted with permission from [6].

The first term, $a_V A$ is the volume term that arises due to the strong nuclear force. The coefficient a_V is empirically determined to be around 15.5 MeV/A [8]. E_B scales linearly with A, suggesting that each of the nucleons only attracts its closest neighbors. Since the nucleons on the surface of a sphere do not have nearest neighbors on all sides, a correction in the form of the second term ($a_S A^{2/3}$), is introduced which is proportional to the surface area of a sphere. The third term is the Coulomb term, to account for the electrostatic repulsion between protons in the nucleus. The next term is known as the asymmetry term or Pauli term as it is derived in part due to the Pauli Exclusion Principle (PEP). The Pauli Exclusion Principle states that a state cannot be occupied by any two identical fermions with the same quantum numbers. At a given energy, there are only a finite amount of quantum

states available for the particles. Consequently, as more nucleons are added to the nucleus, they must occupy higher energy levels, thus, increasing the total energy of the nucleus and decreasing the binding energy. The final component, δ, is the pairing term, accounting for the spin-coupling, where nucleons prefer to couple in a spin-singlet state, so $s = 0$, which is given by Equation 1.2. The shell model, which deals with individual nucleons is partly responsible for the last two terms, along with the Pauli Exclusion Principle.

$$\delta = \begin{cases} +\delta_0 & Z, N \text{ even} \\ 0 & A \text{ odd} \\ -\delta_0 & Z, N \text{ odd} \end{cases} \tag{1.2}$$

Here, δ_0 is empirically determined to be 1 MeV, slowly decreasing as A increases. The pairing term, δ, suggests that like nucleons couple pairwise to form an energetically favorable configuration. This suggests a two-fold degenerate energy level, which indicates that any coupling between the two states lowers the energy of the ground state of the system, thus increasing their attraction, making it more stable. The binding energy from Equation 1.1, plotted against mass number A, is shown in Figure 1.2.

In order to describe the nuclear structure, one must construct a nuclear model that still contains the essentials of nuclear physics. One such model is the nuclear shell model. The nuclear shell model has developed the formulation of the nuclear energy levels and their degeneracies. It starts with the harmonic oscillator and uses the Pauli exclusion principle to describe the energy levels of a nucleus, and thus its structure. While this is the starting point of the shell model, one can use more realistic potentials to get the proper single-particle energy levels. When these energy levels or shells are fully occupied, "magic numbers" are expected. This is discussed in further detail in Section 2.3.1. These are a set of numbers (A) where the next nucleon requires a lot more energy to be added, resulting in an increased binding energy. This is described in more detail in Section 2.3.1.

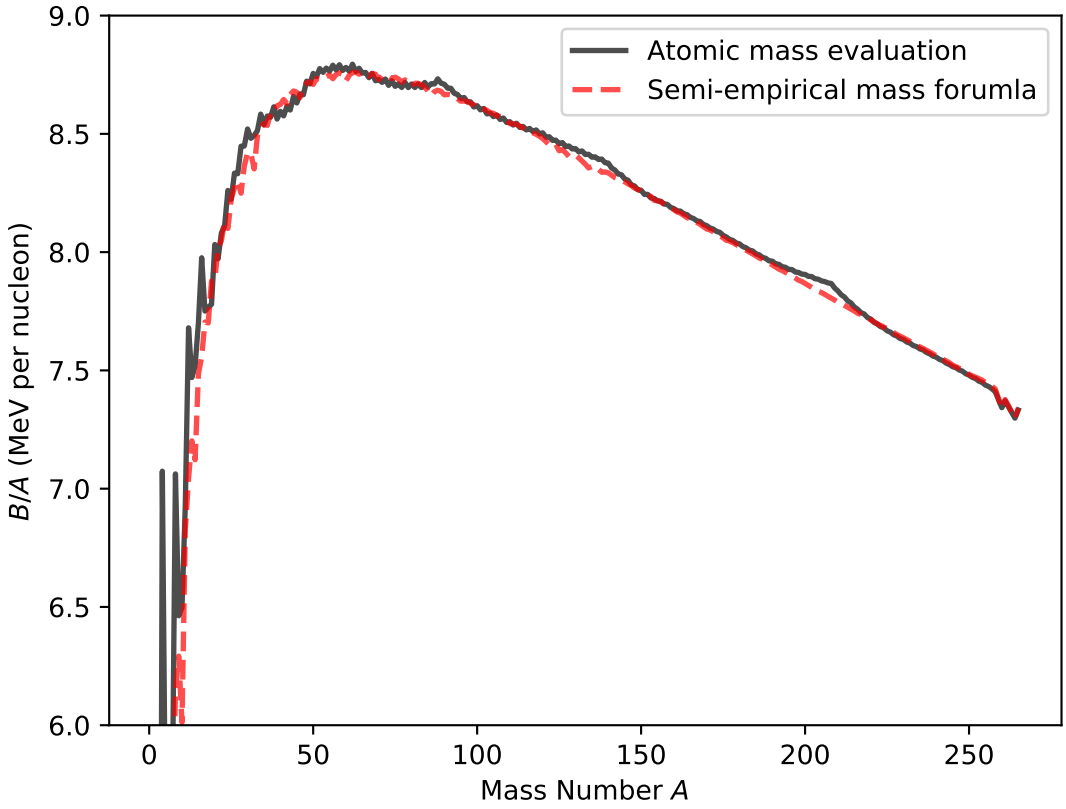

Figure 1.2: Binding energy per nucleon plotted for a range of masses using the semi-empirical mass formula and data available from the Nuclear Energy Agency. This plot shows the close agreement of mean binding energies between the approximation of the semi-empirical mass formula and published values for these binding energies.

1.1 Dissertation work

One of the main goals of nuclear physics is to develop a comprehensive understanding of nuclear structure. The nuclear shell model, introduced almost 70 years ago, provided a useful framework and became the leading nuclear structure model. In order to make quantitative predictions in this framework, it was necessary to introduce many parameters that had to be fitted to the experimental data. For example, in the most simple case of p-shell nuclei, there are 15 independent parameters for residual interactions (two body matrix elements) and 2 single-particle energies (for $p_{3/2}$ and $p_{1/2}$ shells). Calculations that include p-s-d shells

require 203 independent parameters in total. Naturally, as one moves away from well-studied stable nuclei, toward more exotic nuclear species, predictions of the "stable" nuclear shell model that are based on phenomenological fits become less reliable.

Nuclear clustering is the coalescing of nucleons that leads to interesting structures in nuclei [9]. Clustering has long been known to be influential in the structure of ground and excited states of $N = Z$ (self-conjugate) nuclei, and more specifically, $4n$ ($n = 2, 3, 4, ...$), self-conjugate nuclei, otherwise referred to as α-conjugate nuclei. Nuclear clustering is described in further detail in Section 2.3.2.

The high binding energy of the α-particle results in the formation of cluster structures in light nuclei such as ^{6}Li, which display an $\alpha + d$ structure. We can also look at the α-conjugate nuclei, of which the two α-particle system ^{8}Be is the simplest case. This nucleus has a dumbbell structure that gives rise to rotational bands where there is a deformation that can only be described by clustering. The high binding energies of the α-particle and a few of the α-conjugate nuclei are shown in Figure 1.3. The binding energy of these nuclei further increases as they form additional bonds with α-particles. This relationship is shown in Figure 1.4.

Recent theoretical advances open up an exciting prospect of being able to make robust nuclear structure and nuclear reactions calculations starting from "bare" nucleon-nucleon and three-nucleon interactions, or from interactions derived in the framework of Effective Field Theory and constrained to nucleon-nucleon scattering phase shifts and the triton binding energy. The development of powerful theoretical machinery, such as Green's Function Monte Carlo (GFMC), No Core Shell Model (NCSM), Antisymmetrized Molecular Dynamics (AMD, see Section 2.3.3) , Coupled Clusters and other approaches provide a variety of theoretical tools and methods for predicting phenomena in atomic nuclei from first principles. Experimental verification of these predictions is, of course, paramount. Further details on some of these models are presented in Chapter 2.

The focus of this dissertation is on clustering phenomenon in light nuclei. There is strong

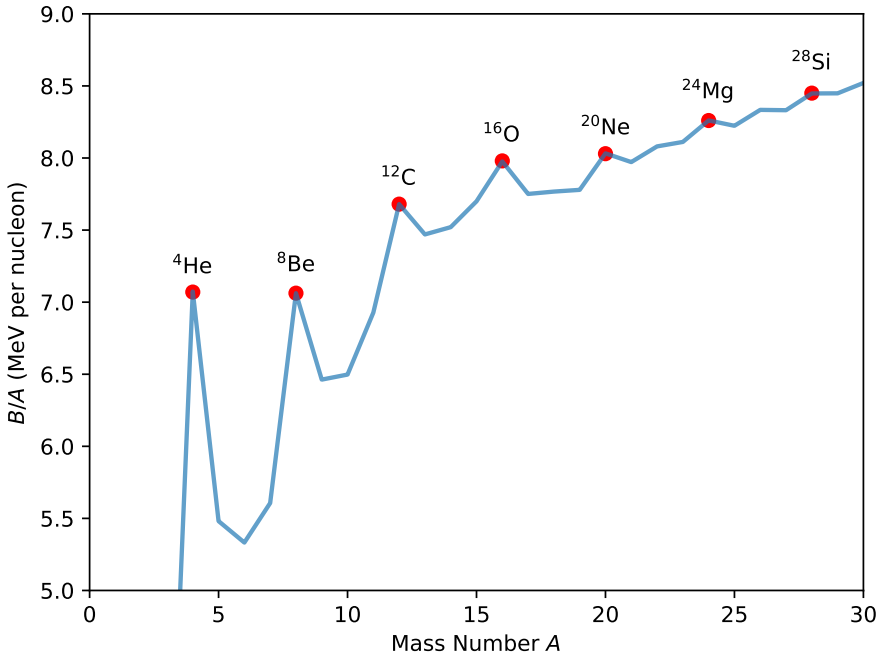

Figure 1.3: The binding energies per nucleon for light beta-stable nuclides (subset of Figure 1.2), with α-conjugate nuclei highlighted. The spikes in binding energies per nucleon can be observed for these α-conjugate nuclei.

experimental and theoretical evidence that some states in ^{10}Be exhibit molecular-like α:2n:α configurations. Recent NCSM calculations provide additional support for this idea.

The role of clustering in ^{10}Be has been studied extensively both theoretically and experimentally since the inception of the Molecular Orbital (MO) model, which described the structure of neutron-rich Be and B isotopes [12, 13, 14]. The dimer $\alpha + \alpha$ core structure of ^{10}Be bound states has been discussed in Ref. [15], and confirmed by AMD calculations [16]. More details about this method is discussed in Section 2.3.3.

There is strong experimental and theoretical evidence that some states in ^{10}Be exhibit molecular-like $\alpha : 2n : \alpha$ configurations. This appears to be a robust prediction of Orbital Molecular theory and AMD. Recent No Core Shell Model calculations provide additional support for this idea. Experimental searches for the 0^+, 2^+ and 4^+ members of the $\alpha : 2n : \alpha$

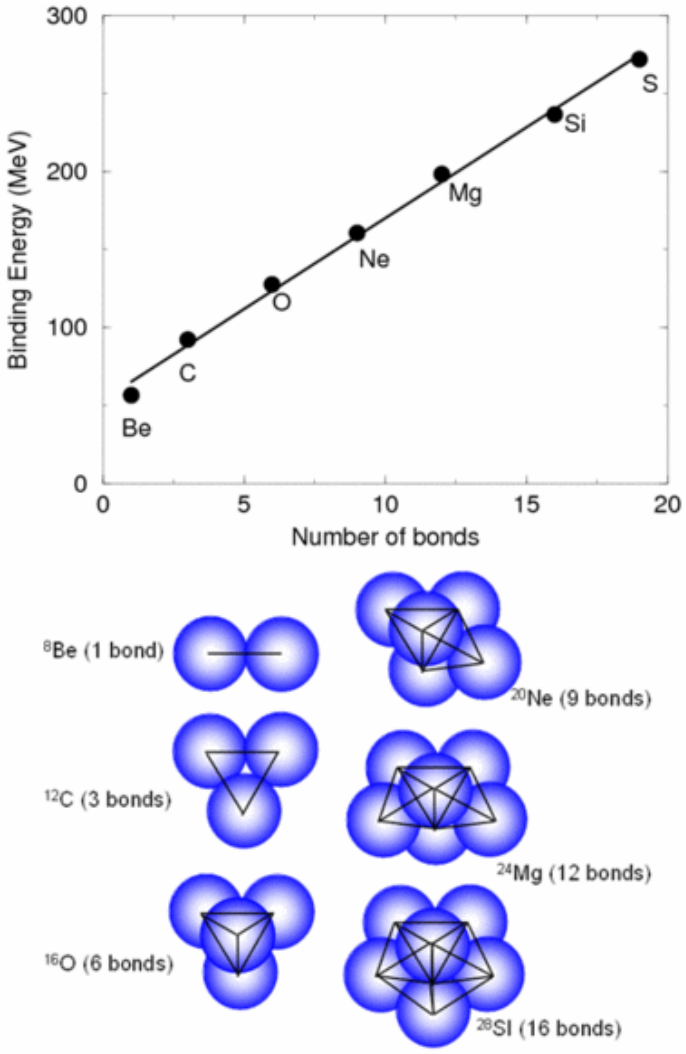

Figure 1.4: Binding energies vs. number of α-particle bonds is shown in the top figure and was originally suggested by Ref. [10]. The proposed arrangements of the α-particle in the molecules is shown in the bottom figure. Reprinted from Ref. [11] (CC BY-NC-SA 3.0).

band in ^{10}Be has been performed and results are reported in Ref. [17, 18, 19]. Experiments searching for the yet unobserved, but predicted, 6^+ member of the α:2n:α rotational band have been performed and their results are reported in Ref. [20, 21]. We performed an experiment to search for the 6^+ state in ^{10}Be at around 13 MeV excitation energy using ^{6}He + α scattering at the Cyclotron Institute. Details about the experimental setup are presented in Chapter 3. The results from this measurement as well as a comparison of our

results with previous measurements are presented here in Chapters 4 and 5.

2. THEORY

Clustering aspects in the nuclear structure of ^{10}Be are studied in this work using nuclear reactions between a rare-isotope beam of ^{6}He and α-particles. An introduction to nuclear reaction and nuclear structure theory that is relevant for this work is provided below in this chapter. In particular, the R-Matrix approach (Section 2.2) that is commonly used to describe resonance reactions is reviewed. I also focus on classical shell model description of nuclear structure (Section 2.3.1) and review some of the modern microscopic theoretical models (Sections 2.3.3 and 2.3.4) that can be used to reproduce clustering phenomena in atomic nuclei. Contemporary understanding of clustering in beryllium isotopes is reviewed at the end of this chapter (Section 2.4).

2.1 Nuclear reactions

A reaction that involves a projectile a impinging on a target A, resulting in two products, b and B, can be conveyed by two different notations. The more explicit notation is written as

$$a + A \rightarrow b + B, \tag{2.1}$$

whereas a more compact notation can be expressed as

$$A(a, b)B. \tag{2.2}$$

In its simplest form, a nuclear reaction is a process by which two nuclei interact to produce nuclides that are often different from the parent nuclei. If the nuclei resulting from the reaction are the same nuclei in the same states as the parent nuclei, the process is called elastic scattering. The time scale of the reaction discriminates the type of reaction that proceeds. Reactions that take place on a faster time scale (of the order of magnitude that it takes the nucleons to traverse the reaction nucleus, 10^{-22} s) are named direct reactions.

Reaction that are comparatively slower are known as compound nucleus reactions, where the reaction proceeds through an intermediate state, forming a compound nucleus.

2.1.1 Direct reactions

Direct reactions are the fastest reactions that occur between two nuclei (on the order of 10^{-22} s) , where the interaction between the incident particle and the target particle happens primarily at the surface of the target particle. These reactions tend to occur at higher energies with fewer internal collisions. As the incident particle energy increases, the de Broglie wavelength decreases. At higher energies (20 MeV proton has a de Broglie wavelength of 1 fm), the incident particle is more likely to interact with nucleon rather than nucleus sized objects. This allows for direct processes which interacts with a single nucleon on valence nucleons at the surface of the target nuclei [8]. The initial direction and energy of the incoming particle generally plays a big role in the final energy and direction of the resulting particle. If, during this type of reaction, both the interacting nuclei are the same before and after the reaction albeit left in an excited state, this is known as inelastic scattering.

Another type of direct reaction is a transfer reaction. This is where one or more nucleons from the projectile or target nuclei are transferred to the other nuclei. A common type of transfer reaction that often occurs through a direct process is a (d, p) reaction. Here, an incoming deuteron particle collides with the target, transferring a neutron to the target. In these reactions, at lower energies, formation of a compound nucleus is still possible. However, the compound nucleus decays isotropically in the center of mass (for L=0 decays), whereas a direct (d, p) reaction has a forward-focused cross section, allowing it to be distinguished from the compound nucleus formation.

Another type of direct reaction is when a projectile or a target nucleus can break apart, resulting in three or more final particles, without going through a compound nucleus. This type of reaction is known as a breakup reaction. A schematic of the three different types of direct reactions is shown in Figure 2.1.

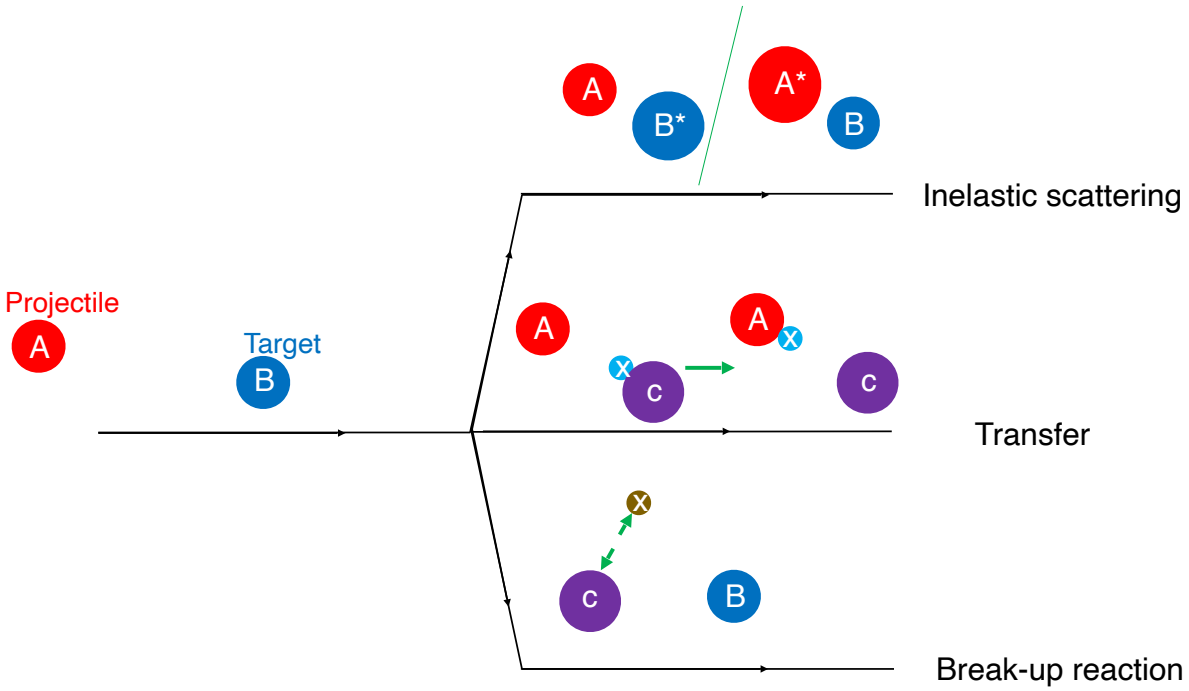

Figure 2.1: Schematic illustrating the three different types of direct reactions. Reprinted with permission from Ref. [6].

2.1.2 Compound nucleus reactions

Compound nucleus reactions proceed through an intermediate state - compound nucleus. As a result, the decays of the compound nucleus are independent of the initial conditions. Symbolically, the reaction

$$a + X \rightarrow Y + b \tag{2.3}$$

becomes

$$a + X \rightarrow C^* \rightarrow Y + b \ , \tag{2.4}$$

where C^* represents a compound nucleus. This process is illustrated in Figure 2.2. This concept of the *independence hypothesis* was originally postulated by Niels Bohr. These reactions involve all the nucleons from the projectile and target nuclei. Many nucleon-nucleon scatterings will take place, dispersing the kinetic energy from the initial nuclei to all

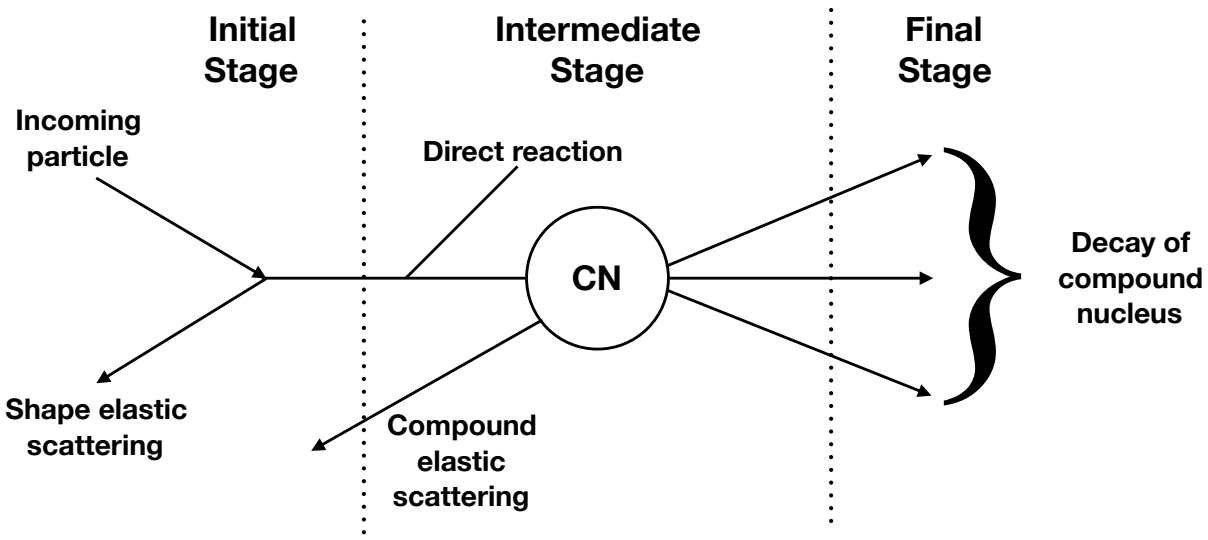

Figure 2.2: Illustration of the stages of a compound nucleus (adopted from Ref. [22]).

the nucleons of a compound nucleus. Example of a compound nucleus reaction is shown in Figure 2.3

$$\begin{matrix} p + {}^{63}\mathrm{Cu} \\ \alpha + {}^{60}\mathrm{Ni} \end{matrix} \rightarrow {}^{64}\mathrm{Zn}^{*} \begin{cases} \rightarrow {}^{63}\mathrm{Zn} + n \\ \rightarrow {}^{62}\mathrm{Cu} + n + p \\ \rightarrow {}^{62}\mathrm{Zn} + 2n \end{cases}$$

Figure 2.3: Examples of reactions forming the compound nucleus ^{64}Zn*, and subsequent decays [8].

A special type of compound nucleus reaction is resonance scattering. At relatively low c.m. energies of colliding nuclei, a few resonances in the compound system can dominate the reaction cross section and form a distinct pattern of "peaks" in the cross section as a function of energy (excitation function). In situations like this the cross section can be described by R-Matrix formulation (see. Section 2.2). The R-Matrix approach is particularly relevant for the results presented in this work and it is reviewed in the next section (Section 2.2).

2.2 *R*-Matrix theory

R-Matrix theory, pioneered by Wigner and Eisenbud [23, 24], puts forth an effective framework to characterize resonance reactions. *R*-Matrix theory can be phenomenological and calculable. The basic goal of phenomenological *R*-Matrix is to fit experimental data to calculate phase shifts and cross sections. This allows the extraction of nuclear structure information from the observables (excitation functions and angular distributions). Calculable *R*-Matrix provides an effective way to solve the Schrödinger equation to calculate phase shifts and cross sections. An outline of this is shown in Figure 2.4.

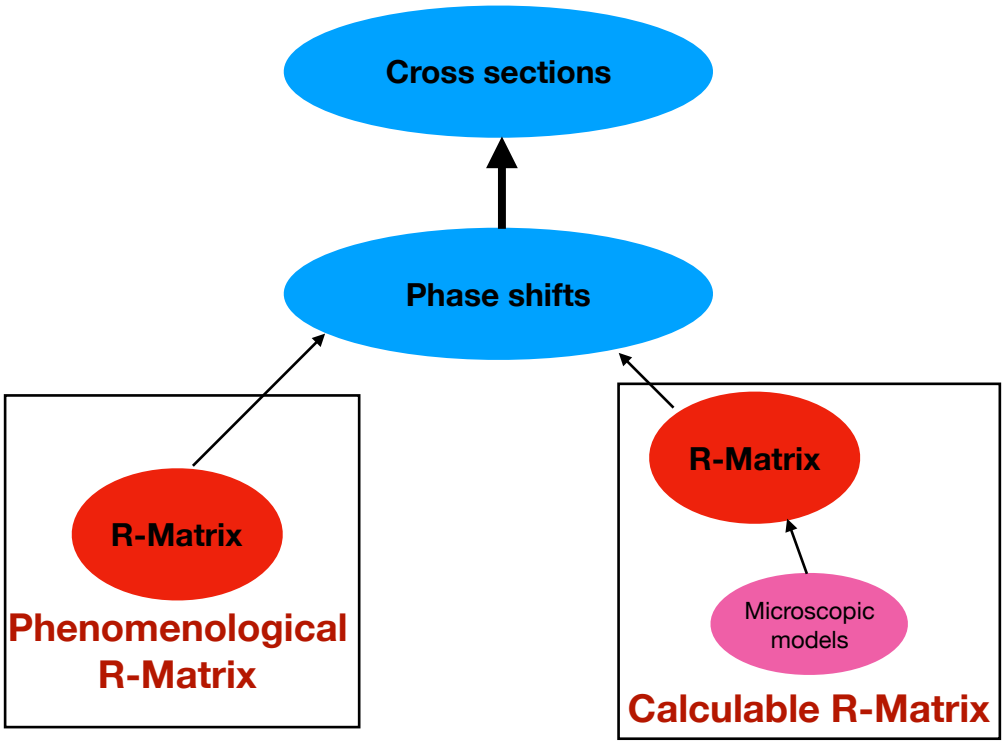

Figure 2.4: Flow chart describing the general overview of *R*-Matrix theory. In the case of phenomenological *R*-Matrix, experimental data are used to calculate the *R*-Matrix, which is then used to calculate phase shifts and cross sections. For calculable *R*-Matrix, parameters from models are used to calculate the *R*-Matrix, which is then used to calculate phase shifts and cross sections.

At its core, the nuclear potential is divided into two separate regions as shown in Figure

2.5. The first is the internal region ($r \leq a$), which contains the nuclear and Coulomb interactions. The second region is the external region ($r > a$), that contains Coulomb interactions only. This radius r must therefore be chosen to be sufficiently far away from the core of the nucleus that the nuclear force is no longer felt.

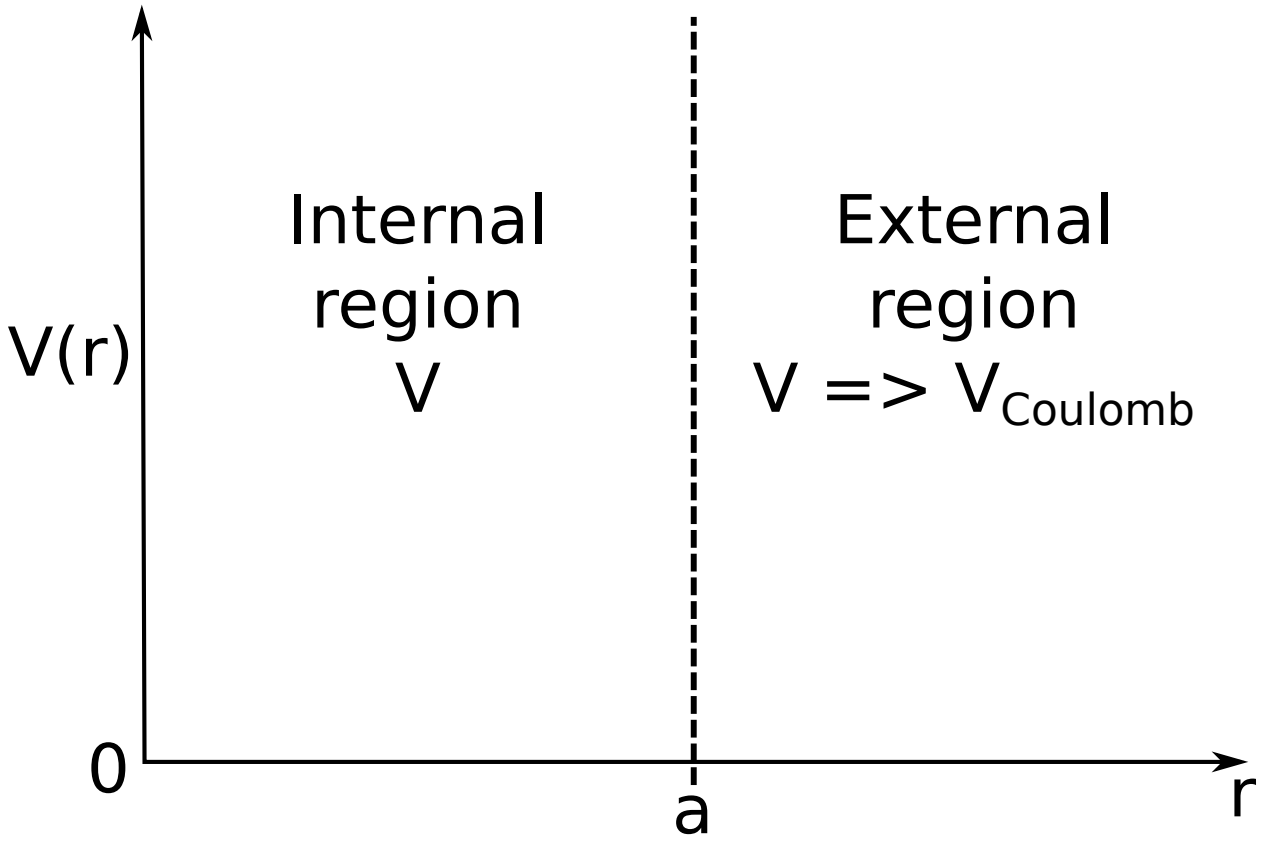

Figure 2.5: *R*-Matrix formulation for the compound nucleus divides the nuclear potential into two regions (internal and external). The internal region is where $r < a$. The external region is $r > a$. The nuclear force is no longer felt in the external region and the contributions for the potential come from the Coulomb and the centrifugal forces.

In its simplest form, *R*-Matrix theory reduces to the Breit-Wigner equation for a single resonance shown in Equation 2.5,

$$\sigma_{if} = \frac{\pi(2J+1)}{k^2(2S_i+1)(2S_f+1)} \frac{\Gamma_i \Gamma_f}{(E_i - E_c)^2 + (\Gamma/2)^2}, \tag{2.5}$$

where, Γ_i is the partial width for the incoming channel, Γ_f is the partial width for the outgoing channel and Γ is the total width of the resonance, E_i and E_c are the energy and resonance energy in the center of mass reference frame, k is the wave number (radians per unit distance), J is the spin of the resonance, S_i is the spin of the incoming channel, and S_f is the spin of the outgoing channel. For a full derivation and further details not presented in this work, see Ref. [23]. We consider a system of nucleons that has two solutions, Ψ_i and Ψ_2. We can define the Schrödinger equations as shown in Equations 2.6 and 2.7,

$$H\Psi_1 = E_1\Psi_1, \tag{2.6}$$

and

$$H\Psi_2 = E_2\Psi_2, \tag{2.7}$$

where the Hamiltonian operator for the $a + A$ channel, H is defined as

$$H = H_0 + H_{rel} + H_a + H_A, \tag{2.8}$$

with,

$$H_0 = \frac{-\hbar^2}{2(m_a + m_A)}\nabla_R^2, \tag{2.9}$$

describing the motion of $a + A$, where masses m_a and m_A are the masses of the respective particles.

$$H_{rel} = \frac{-\hbar^2}{2\mu_a A}\nabla_{r_{aA}}^2 + V_{rel}(r_{aA}) \tag{2.10}$$

Equation 2.10 describes the relative motion of the two particles with

$$\mu_{aA} = \frac{m_a m_A}{m_a + m_A}, \tag{2.11}$$

being the reduced mass, r_{aA} is the distance between a and A. The internal Hamiltonians for

a and A are

$$H_a = (T_{internal})_a + (V_{internal})_a, \tag{2.12}$$

$$H_A = (T_{internal})_A + (V_{internal})_A. \tag{2.13}$$

Similar to Equation 2.8, the total wave function Ψ for a given channel is expressed as

$$\Psi = \Phi(\mathbf{R})\chi(\mathbf{r}_{aA})\psi_a(r_a)\psi_A(r_A), \tag{2.14}$$

where the wave functions Φ, χ, $\psi_a(r_a)$, and $\psi_A(r_A)$ describe the centroid motion, the relative motion of a and A and the internal states of a and A respectively. Here, $\mathbf{R}$ is the centroid position vector of the whole system, $\mathbf{r}_{aA}$ is the radius vector between a and A. r_a and a_A are the radial coordinates of a and A respectively.

If we multiply Equation 2.6 by Ψ_2^*, and the complex conjugate of Equation 2.7 by Ψ_1, we have

$$H\Psi_1\Psi_2^* = E_1\Psi_1\Psi_2^* \tag{2.15}$$

$$H^*\Psi_2^*\Psi_1 = E_2\Psi_2^*\Psi_1^*. \tag{2.16}$$

If we subtract Equation 2.16 from Equation 2.15 and integrate over the internal region τ, we get

$$(E_2 - E_1)\int_\tau \Psi_2^*\Psi_1 d\tau = \int_\tau (H^*\Psi_2^*\Psi_1 - \Psi_2^* H\Psi_1)d\tau. \tag{2.17}$$

Considering Equation, 2.8, 2.9 and 2.10, as well as assuming that the potentials $V_{internal}$ and V_{rel} are self-adjoint as in

$$\int_\tau [(V\Psi_2)^*\Psi_1 - \Psi_2^* V\Psi_1]d\tau = 0, \tag{2.18}$$

and using Green's Theorem ($\oint_S LdS = \int_\tau (\partial L/\partial y)d\tau$)

$$\int_\tau (\nabla\cdot\nabla\Psi_2)^*\Psi_i d\tau = \oint_S (\nabla_n\Psi_2)^*\Psi_1 dS, \tag{2.19}$$

where $\nabla_n \perp S$, to integrate the kinetic energy terms. The following can be derived

$$(E_2 - E_1) \int_\tau \Psi_2^* \Psi_1 d\tau = \frac{-\hbar^2}{2\mu_c} \int_{S_c} (\Psi_2^* \nabla_n \Psi_1 - \Psi_1 \nabla_n \Psi_2^*) dS_c = \sum_c (\gamma_{2c}^* D_{1c} - \gamma_{1c} D_{2c}^*), \quad (2.20)$$

where $aA = c$, and $\gamma_{\lambda c}$ is the c^{th} channel of the λ^{th} resonance, and is defined as,

$$\begin{aligned} \gamma_{\lambda c} &= \left(\frac{\hbar^2}{2\mu_c a_c} \right)^{\frac{1}{2}} u_c(a_c) \\ &= \left(\frac{\hbar^2}{2\mu_c a_c} \right)^{\frac{1}{2}} \int_{S_c} \varphi_c^* X_{\lambda JM} dA \ , \end{aligned} \quad (2.21)$$

and the derivative of the radial part of the wave function (Eq. 2.14) at the surface $D_{\lambda c}$, and is defined as,

$$D_{\lambda c} = \left(\frac{\hbar^2}{2\mu_c a_c} \right)^{\frac{1}{2}} \left[\frac{du_c}{dr} \right]_{r=a_c} , \quad (2.22)$$

φ_c and $X_{\lambda JM}$ from Eq. 2.21 are the channel wave function and a set of states for the channel, respectively. The radial part of the relative motion wave function, χ is $u_c(r)$, and the channel radius a_c is defined as

$$a_c = r_0 (A_1^{1/3} + A_2^{1/3}) \ , \quad (2.23)$$

which, at the surface has $r_0 \equiv 1.4$ fm [23].

We now define boundary conditions that are satisfied by a complete set of states $X_{\lambda JM}$ on the surface S_c and are independent of λ. This boundary condition is of the form

$$B_c = \frac{D_{\lambda c}}{\gamma_{\lambda c}}. \quad (2.24)$$

When this boundary condition (Eq. 2.24) is applied to Eq. 2.20 to two proper solutions X_λ

and $X_{\lambda'}$, they are mutually orthogonal and normalized

$$\int_{\tau} X^*_{\lambda'} X_{\lambda} d\tau = \delta_{\lambda\lambda'} \ . \tag{2.25}$$

The wave function Ψ can then be expressed in terms of these solutions as

$$\Psi = \sum_{\lambda} A_{\lambda} X_{\lambda} \ , \tag{2.26}$$

where A_{λ} are coefficients defined as

$$A_{\lambda} = \int_{\tau} X^*_{\lambda} \Psi d\tau. \tag{2.27}$$

Eq. 2.20 can be applied to the wave function Ψ with energy E and solution X_{λ} with energy E_{λ}, which yields:

$$A_{\lambda} = (E_{\lambda} - E)^{-1} \sum_{c} D^0_{\lambda c} \gamma_{\lambda c} \ , \tag{2.28}$$

where, $D^0_{\lambda c} = D_{\lambda c} - B_c \gamma_{\lambda c}$.

A rather important quantity here is $\gamma_{\lambda c}$, which is the reduced width amplitude and is related to the partial decay with by

$$\Gamma_{\gamma c} = 2 P_c(ka_c) \gamma^2_{\lambda c} \ , \tag{2.29}$$

where, $P_c(ka_c)$ is the penetrability factor, defined as

$$P_c(ka_c) = \frac{ka_c}{F^2_l(\eta, ka_c) + G^2_l(\eta, ka_c)}. \tag{2.30}$$

Here F_l and G_l are the regular and irregular Coulomb wave functions, respectively, k is the wave number and a_c is the channel radius. Now the expansion for Ψ can be expressed as

$$\sum_c D_c^0 \left(\sum_\lambda \frac{X_\lambda \gamma_{\lambda c}}{E_\lambda - E} \right). \tag{2.31}$$

By using Eq. 2.21 on Eq. 2.31, the fundamental R-Matrix relation can be extracted, which is:

$$\gamma_c^{'} = \sum_c R_{c'c} D_c^0 \ , \tag{2.32}$$

which can be simplified into a matrix notation

$$\boldsymbol{\gamma = RD^0} \ , \tag{2.33}$$

where $\boldsymbol{R} \equiv R_{c'c}$ is the R-Matrix, and is defined as

$$R_{c'c} = \sum_\lambda \frac{\gamma_{\lambda c'} \gamma_{\lambda c}}{E_\lambda - E}. \tag{2.34}$$

In the external region, shown in Figure 2.5, the solution Ψ can be expanded in terms of the incoming and outgoing waves (I_c and O_c respectively), expressed as

$$\Psi = \sum_c (x_c O_c + y_c I_c) \ . \tag{2.35}$$

Hence, the γ_c and D_c are defined as

$$\gamma_c = \left(\frac{\hbar}{2\rho_c} \right)^{\frac{1}{2}} (x_c O_c + y_c I_c) \tag{2.36}$$

$$D_c = \left(\frac{\hbar \rho_c}{2} \right)^{\frac{1}{2}} (x_c O_c^{'} + y_c I_c^{'}) \ , \tag{2.37}$$

where $\rho_c \equiv k a_c$. The collision matrix $U_{c'c}$, is expressed in terms of the wave coefficients x_c and y_c, such that,

$$x_{c'} = -\sum_c U_{c'c} y_c. \tag{2.38}$$

This can be expressed in matrix notation as

$$\boldsymbol{x} = -\boldsymbol{U}\boldsymbol{y} \tag{2.39}$$

We can combine Equations 2.33, 2.36, 2.37 and 2.39 and solve for a relationship between R-Matrix and the collision matrix, which is expressed as

$$\boldsymbol{U}^J = \frac{\boldsymbol{I}\boldsymbol{\rho}^{-1/2} - \boldsymbol{R}^J\boldsymbol{I}'^0\boldsymbol{\rho}^{1/2}}{\boldsymbol{O}\boldsymbol{\rho}^{-1/2} - \boldsymbol{R}^J\boldsymbol{O}'^0\boldsymbol{\rho}^{1/2}} \tag{2.40}$$

The general form for the differential cross section for a particle with channel spin s, component v, and type α is given by

$$d\sigma_{\alpha sv,\alpha' s' v'} = \left|A_{\alpha sv,\alpha' s' v'}(\Omega_{\alpha'})\right|^2 d\Omega_{\alpha'} \ , \tag{2.41}$$

where $A_{\alpha sv,\alpha' s' v'}(\Omega_{\alpha'})$ is the scattering amplitude and is defined as

$$A_{\alpha sv,\alpha' s' v'}(\Omega_{\alpha'}) = \frac{\pi^{1/2}}{k_\alpha}\{-C_{\alpha'}(\theta_{\alpha'})\delta_{a' s' v',\alpha sv} + i\sum_{l'm'} l(2l+1)^{\frac{1}{2}} \times [e^{2i\omega}\alpha^{'}\delta_{a' s' v' l' m',\alpha svl0} - U_{a' s' v' l' m',\alpha svl0}]\}Y_m^{(l)}(\Omega_{\alpha'}), \tag{2.42}$$

where C represents the Coulomb amplitude,

$$C_\alpha(\theta_\alpha) = (4\pi)^{-\frac{1}{2}}\eta_\alpha csc^2\left(\frac{\theta_\alpha}{2}\right)\exp\left\{-2i\eta_\alpha \log sin\left(\frac{\theta_\alpha}{2}\right)\right\}. \tag{2.43}$$

The total cross section for most reactions (except charged-particle elastic scattering) is extracted by summing over all the $\alpha^{'}$,

$$\sigma_\alpha^{Total} = \frac{\pi}{k_\alpha^2}\sum_J \frac{2J+1}{(2I_1+1)(2I_2+1)}\sum_{sls'l'}[1 - \mathrm{Re}(U^J_{\alpha sl,\alpha' s' l'})], \tag{2.44}$$

where I_i is the spin of the i^{th} channel. For further details of this derivation and formalism,

refer to Ref. [23, 24].

2.3 Nuclear structure

Certain aspects of nuclear structure theory that are relevant for the experimental work presented in this thesis are reviewed in this section. Discussion of the nuclear shell model is followed by a general overview of clustering phenomena in atomic nuclei and a brief introduction to modern theoretical approaches that are capable of describing nuclear clusters starting from nucleon-nucleon and three-nucleon forces. Finally, a more detailed discussion of clustering in beryllium isotopes is presented.

2.3.1 Shell model

The nuclear shell model is a very successful, semi-phenomenological model of nuclear structure that has been extensively used for more than 60 years. The main starting point of this theory is to consider nuclei as quantum many-body systems that consist of independent nucleons moving within the confines of a common potential. Nucleons in a nucleus have quantized energy levels, defined by this common potential, as well as varying degrees of degeneracy, allowed by Pauli exclusion principle, that gives rise to a shell structure.

The average nuclear force felt inside a nucleus by a nucleon can be approximated as a simple harmonic oscillator potential shown in Equation 2.45, where m is the reduced mass, ω is the angular frequency and r is the distance from the center of the system. While this is a simplification, this potential is used because the Schrödinger equation with this potential has an analytical solution, and is still able to represent the overall behavior of the system.

$$V(r) = \frac{1}{2} m\omega^2 r^2 \tag{2.45}$$

Beyond that, the Woods-Saxon potential is a more realistic potential to use [25], taking the form:

$$V(r) = \frac{-V_0}{1 + \exp[(r - R)/a]}\,, \tag{2.46}$$

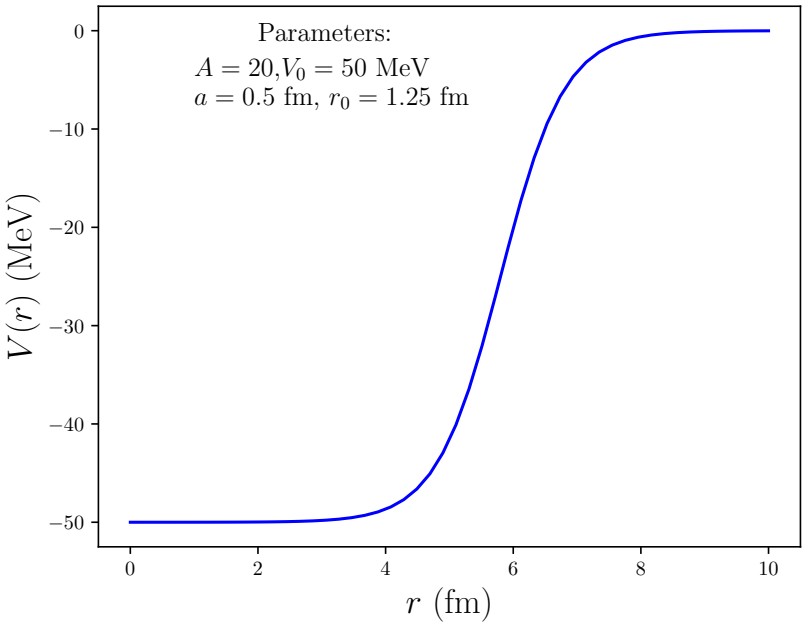

Figure 2.6: A plot of the Woods-Saxon potential using the parameters specified on the plot. This plot shows that the $V \to 0$ as $r \to \infty$. This further demonstrates the short-range nature of the strong nuclear force.

where V_0 is the strength or depth of the potential well and is on order of 50 MeV, a is the diffuseness parameter of the nuclear surface (describing the range of the strong force) and R is the nuclear radius, which varies with mass number as

$$R = r_0 A^{1/3}, \tag{2.47}$$

where r_0 varies between 1.2 to 1.4 fm. A harmonic oscillator potential does not remain finite as $r \to \infty$, but rather, $V \to \infty$. This is different with the Woods-Saxon potential however, as shown in Figure 2.6. As $r \to \infty$, the Woods-Saxon potential $V \to 0$. Therefore, the harmonic oscillator potential cannot be expected to reproduce the asymptotic behavior ($r \to \infty$) of nuclear wave functions, but provides a reasonable approximation in the nuclear interior.

The Schrödinger equation in spherical coordinates is defined and solved as follows:

$$\hat{H}\Psi = (\hat{T} + \hat{V})\Psi = E\Psi \tag{2.48}$$

The solution to the Schrödinger equation in spherical coordinates (r, θ, ϕ) can be expressed as a product of the radial part and the angular parts:

$$\Psi(r, \theta, \phi) = R(r)\Theta(\theta)\Phi(\phi). \tag{2.49}$$

The product of Θ and Φ is defined as a spherical harmonic $Y_{\ell m}$, and thus, Equation 2.49 can be rewritten as

$$\Psi(r, \theta, \phi) = R(r)Y_{\ell m}(\theta, \phi). \tag{2.50}$$

And thus with $V = \frac{1}{2}m\omega^2 r^2$,

$$\left[-\frac{\hbar^2}{2\mu r^2}\frac{d}{dr}\left(r^2\frac{d}{dr}\right) + \frac{\hbar^2\ell(\ell+1)}{2\mu r^2} + \frac{1}{2}\mu\omega^2 r^2 \right] R(r) = ER(r), \tag{2.51}$$

with μ being the reduced mass. This is the radial wave equation and can be solved using power series, yielding discrete energy eigenvalues:

$$E = \left(2n + \ell + \frac{3}{2}\right)\hbar\omega, \tag{2.52}$$

where the principle quantum number n represents the number of nodes in the radial wave function, and ℓ is the orbital angular momentum. The energy is independent of m_l, which can be any value between $\pm\ell$. This leads to $(2l+1)$ projections of m_l for each ℓ. The orbital angular momentum, ℓ, is denoted by s, p, d, f,... for $\ell = 0, 1, 2, 3, ...$ and is known as the spectroscopic notation. The parity of the wave function is determined by Y_{lm} and is $(-1)^l$. Since the nucleons also have two possible spin projections $(\pm 1/2)$, we have a degeneracy of $2(2\ell + 1)$, neglecting the spin-orbit interaction. Looking at the first few energy levels: $\frac{3}{2}\hbar\omega$, $\frac{5}{2}\hbar\omega$, $\frac{7}{2}\hbar\omega$, $\frac{9}{2}\hbar\omega$, yields degeneracies of 2, 6, 12, 20 for the respective energy levels. This gives

us magic numbers of 2, 8, 20, 40. However, since the spin-orbit coupling effects are neglected, these (beyond 20) are ultimately incorrect. The shells in the shell model are organized by their quantum numbers. These quantum numbers are properties of the spherical harmonic function Y_{lm}.

The spin-orbit coupling interaction term can be written as $V_{ls}\vec{l}\cdot\vec{s}$, where $l\cdot s$ is responsible for the reordering of the levels. In the presence of spin-orbit coupling, states are written in terms of total angular momentum $\vec{j} = \vec{l} + \vec{s}$. A single nucleon has a spin $s = \frac{1}{2}$. Therefore, the possible values of the total angular momentum quantum numbers are $j = l + 1/2$ or $j = l - 1/2$. In the case of $l = 0$, $j = 1/2$ is the only allowed value. The magic numbers that follow now are: 2, 8, 20, 28, 50, 82, 126 and 184. A level scheme can be seen in Figure 2.7 showing the degeneracy modification of this additional term.

The model space in the shell model comprises of three regions, which are the core, valence space and the external space. The core region consists of the inert core with fully-filled orbitals. The valence space, as the name suggests, consists of valence nucleons, which are nucleons outside the filled orbitals. When a nucleus has more than one valence nucleon in the valence space, a residual two-body interaction term must be included. The residual interaction term is not included in the central potential. As such, these interactions are treated as free parameters and phenomenological [26]. Extending the valence space to the inert core and using realistic ("bare") nucleon-nucleon and three-nucleon forces leads to a development of the so called *ab initio* models, which is a significant contemporary breakthrough for nuclear theory made during the last three decades.

To summarize, despite starting from rudimentary assumptions of the nuclear potential, the shell model provides a reasonable prediction for the ground states across the chart of nuclides. In an excited nucleus, protons or neutrons move to a higher shell, leaving a vacant shell space, known as a hole. Whilst this provides a reasonable description of low-lying states, predictions of higher states are often incorrect since the shell model treats these nucleons as independent. However, in reality, these nucleons interact with each other. A preferential

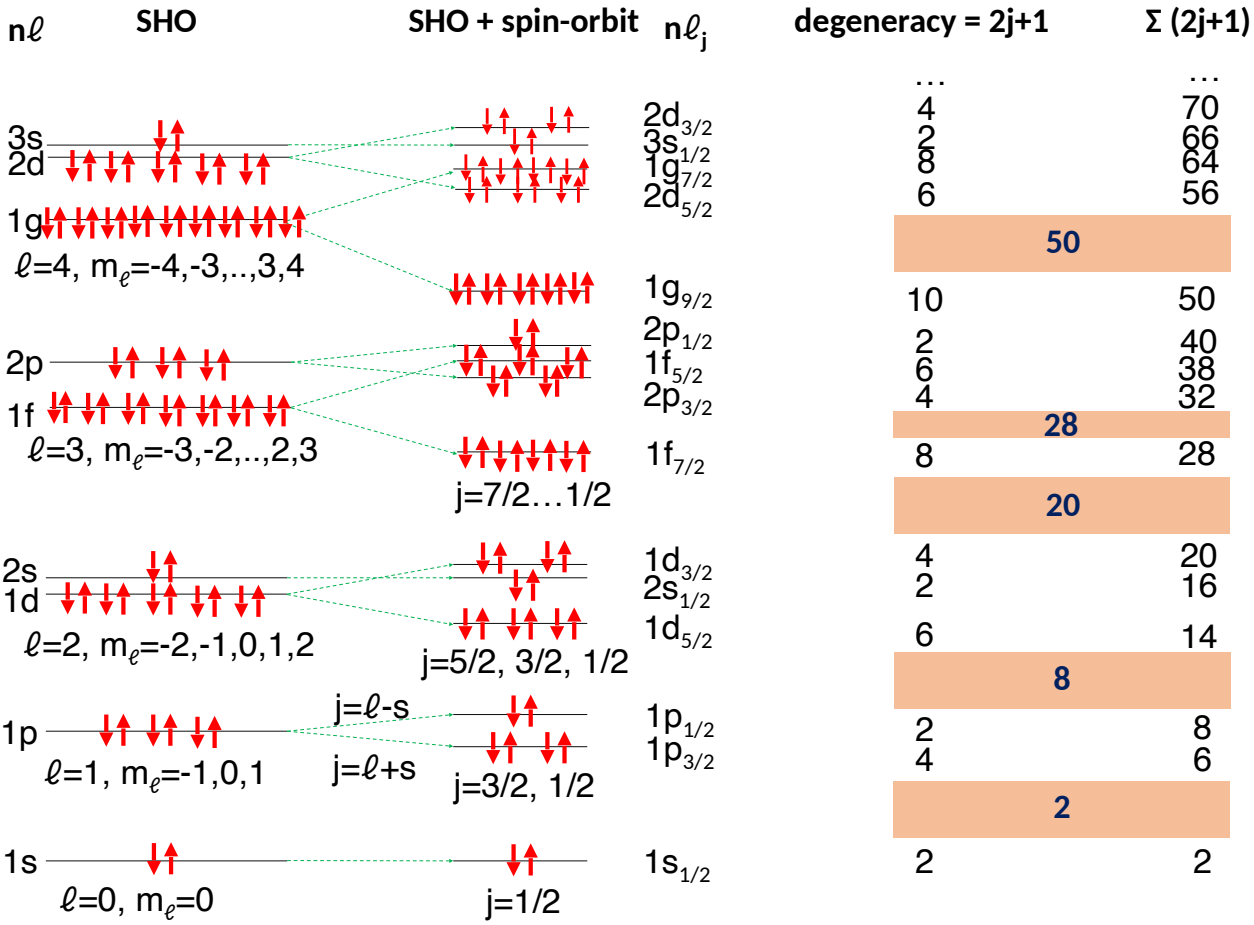

Figure 2.7: Shell model level scheme. At the left are the energy levels calculated with the harmonic oscillator potential and their degeneracies. In the middle we have the effect of the spin-orbit interaction, which splits levels with $l > 0$ into two new levels. On the right are the magic numbers (orange). Adopted from Ref. [6].

excitation may therefore involve the movement of multiple nucleons to a higher shell.

2.3.2 Nuclear clustering

Clustering phenomena has long been known to be influential in determining the structure of light nuclei, and more specifically, the structure of ground and excited states of $N = Z$ nuclei. The idea of nuclear clustering was put forth in light of the discovery of α-decay of heavy nuclei. Looking at the binding energy per nucleon of various nuclei, one can observe a maxima for nuclei that are self-conjugate ($N = Z$) with an even number of protons and neutrons. These nuclei such as, ^{4}He, ^{8}Be, ^{12}C, ^{20}Ne and ^{24}Mg, are known as the $4n$-type nuclei (where n = 1,2,3,4...), and exhibit interesting features that are not explained by simple shell-model theories [27].

The best examples of clustering revolve around α-particles, and specifically α-conjugate nuclei. The famous Ikeda diagram (Figure 2.8) shows the cluster configurations and the excitations at which they are expected to manifest. Since the residual interactions are predicted to be weak around the decay threshold, cluster structures are expected to manifest themselves near these energies. α-conjugate nuclei can manifest as N-α clustering, which is where the nucleus is made up solely from α-particles. This structure manifests just above the decay threshold of these α-particles. The seminal example of this is the 3-α cluster structure of ^{12}C. This specific cluster structure was predicted to manifest above the 3-α decay threshold energy of 7.27 MeV. The Hoyle state, which is a 0^{+} state of great astrophysical importance has been discovered at 7.65 MeV, and has been shown to have a 3-α cluster structure [28].

Experimental observations show that cluster structures are very common in light nuclei. The earliest models that described these observations used α-particle cluster models. An α particle also acts as an inert core since its first excited state is above 20 MeV. Cluster structures can be found in ground states as well as excited states. In excited states, the structures tend to be more deformed and form rotational bands. Here, due to the effective potential, the α-particles act as pseudo-bosons, since $s_{\alpha} = 0$. However, in the ground state, as the α-particles are closer to each other, the underlying protons and neutrons are resolved,

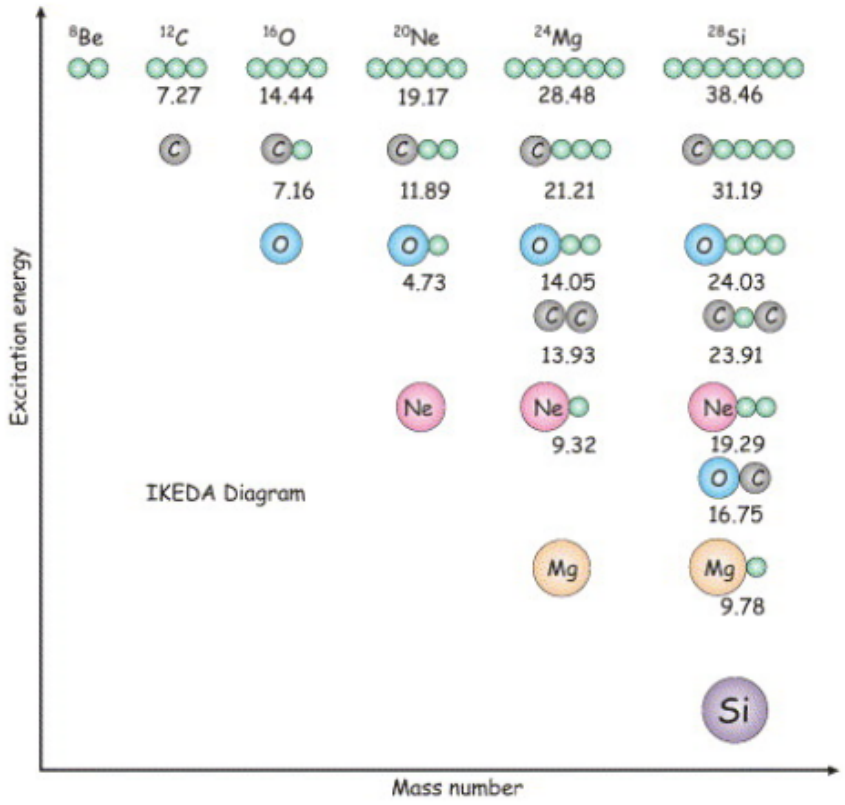

Figure 2.8: The Ikeda diagram shows the different cluster configurations in α-conjugate nuclei at various excitation energies (Image adapted from [29] by Ref. [6]. Reprinted with permission.)

resulting in a more compact cluster structures where the nucleons are influenced by the Pauli Exclusion Principle.

When the nucleons in a system can be well described by mean field characteristics, the shell model can be used to describe it well. However, α-clusters exhibit deformations, which play a crucial role in determining its structure. Therefore, the deformed harmonic oscillator is used to characterize the α-particle motion. The energy levels of the deformed harmonic oscillator are given by:

$$E = \hbar\omega_{\perp} n_{\perp} + \hbar\omega_z n_z + \frac{3}{2}\hbar\omega_0, \tag{2.53}$$

where we now include oscillator frequencies in the perpendicular ($\perp$) and parallel (z) planes to the deformed axis. There are now constraints placed on ω_0 as well, which is now defined

by:

$$\omega_0 = 2\omega_\perp + \omega_z, \tag{2.54}$$

and the quadrupole deformation is:

$$\epsilon = \epsilon_2 = \frac{\omega_\perp + \omega_z}{\omega_0}. \tag{2.55}$$

Quadrupole deformation changes the degeneracy of the system. Oscillations along n_z will have different energy contributions from $n_\perp$. Depending on if the quadrupole deformation is positive, negative or zero, the nucleus deformation will be prolate, oblate or spherical, respectively. At deformations of $j : 1$ (j = 1,2,3,...), the deformations are illustrated in Figure 2.9. These deformations repeat $j : 1$ times, indicating that the $j : 1$ system is made up of j interacting spherical potentials.

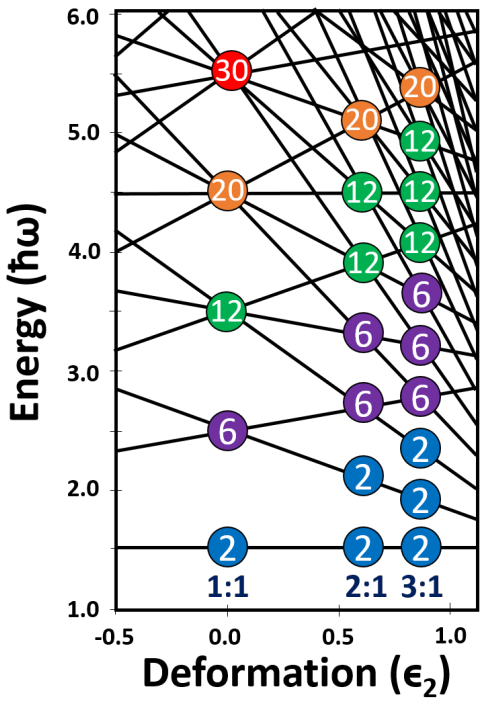

Figure 2.9: The energy levels of the deformed harmonic oscillator and the degeneracies at deformations of 1:1, 2:1 and 3:1. Reprinted with permission from Ref. [6].

These deformed harmonic oscillator calculations further demonstrate that linear chain configurations in α-conjugate nuclei could also be described. The densities of 2:1, 3:1, and 4:1 deformations are shown in Figure 2.10.

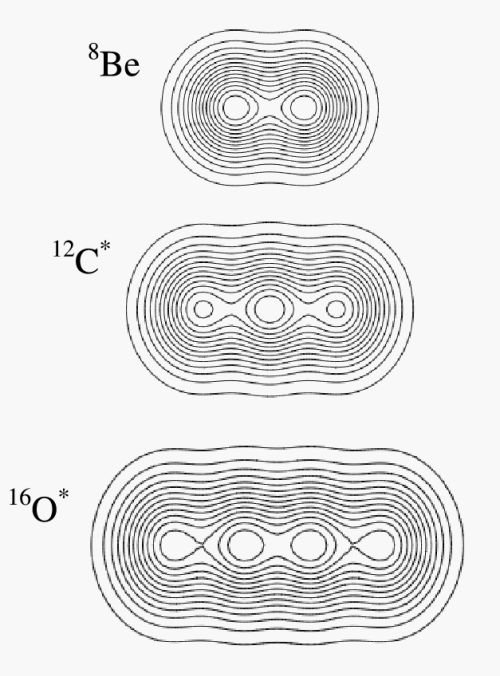

Figure 2.10: Density calculations of 2:1, 3:1, and 4:1 deformed harmonic oscillators showing 2, 3, and 4-fold degeneracy patterns. This shows the α cluster structures. Reprinted with permission from [9].

So far, we've discussed α-conjugate nuclei and their propensity of exhibiting cluster structures, specifically in light nuclei. However, there is significant evidence to show pronounced cluster structures of these nuclei with the addition of neutrons to the system. For many of these nuclei, the additional neutrons are labeled as "valence" neutrons, and their behavior is not dissimilar to valence electrons in an atomic compound. A representation of these states is shown in Figure 2.12.

These nuclei with additional neutrons form more tightly-bound molecular structures with deformed structures and rotational bands. If we consider the neutron-rich beryllium isotopes,

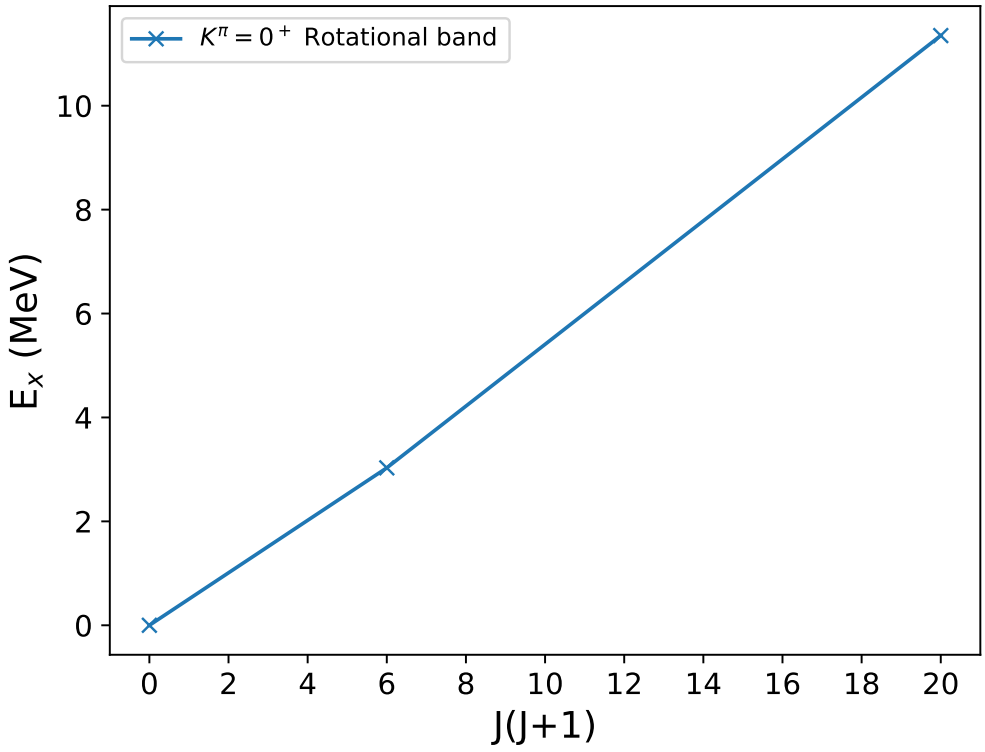

Figure 2.11: The rotational band with the band-head at 0^+ ground state, of which 2^+, and 4^+ states are members of, is shown here. A linear relationship between the excitation energy and angular momentum of these states can be observed.

the valence neutrons orbit the $\alpha + \alpha$ core. The molecular orbital approach was successful in describing low-lying states in these types of nuclei that have two cores with additional neutrons that make up rotational bands of π and σ orbitals, similar to the ones in atomic molecules [30, 14]. In the π orbital, the valence neutrons traverse in a perpendicular direction to the plane in which the α-cores lie, and in the σ orbital, the valence neutrons traverse in the same plane as the α-cores. These two types of orbitals yield different deformations of the nucleus. A representation of the two types of orbitals is shown in Figure 2.13.

The existence of molecular-type structures has garnered much theoretical and experimental efforts to describe these systems. These rotational bands have been explained in terms

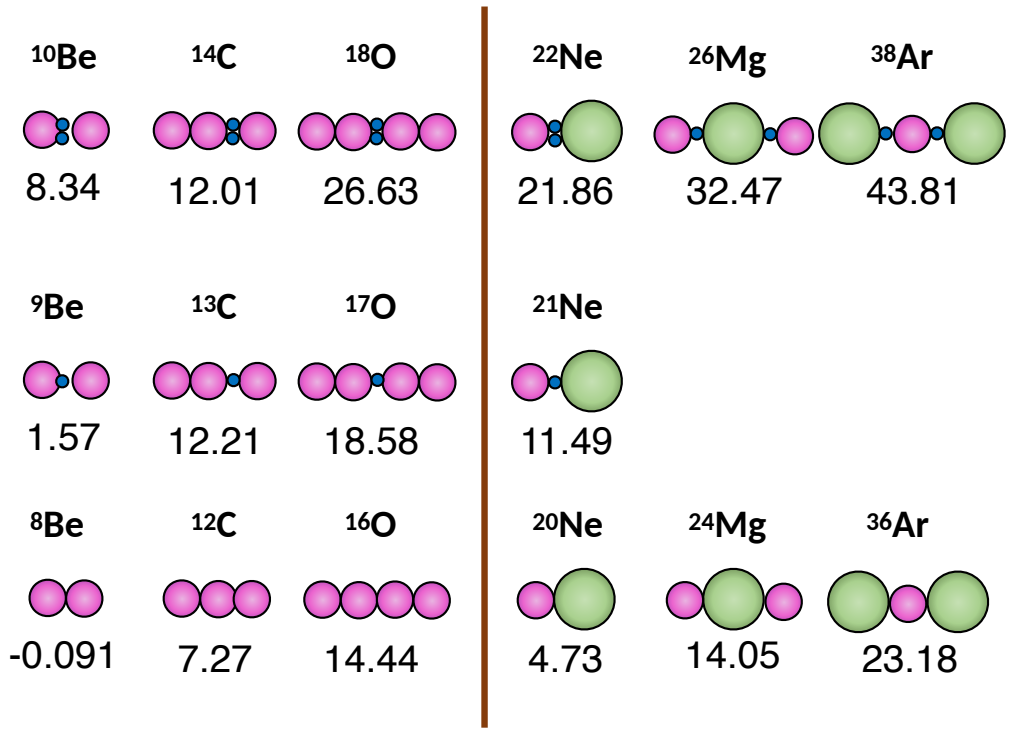

Figure 2.12: The extended Ikeda diagram is an extension of the Ikeda diagram shown in Figure 2.8. This shows the cluster structures that can emerge when "valence" neutrons are added to the α-conjugate nuclei. Reprinted with permission from Ref. [6].

of exchange nucleons in either π or σ orbitals. The rotational energy is defined by

$$E_{rot} = E_0 + \frac{\hbar^2}{2I} J(J+1), \tag{2.56}$$

where J is the total angular momentum quantum number $\vec{J} = \vec{L} + \vec{S}$ ($\vec{L}$ is the orbital angular momentum and $\vec{S}$ is the spin angular momentum), E_0 is the bandhead energy and I is the moment-of-inertia of the system. These states form rotor-like rotational structures where the excitation energies of the states that are part of a rotational bands are proportional to $J(J+1)$. This is shown for the rotational band built on the ground state of ^{8}Be in Figure 2.11. Similar relationships can be observed for other nuclei that exhibit cluster structures and rotational bands as well.

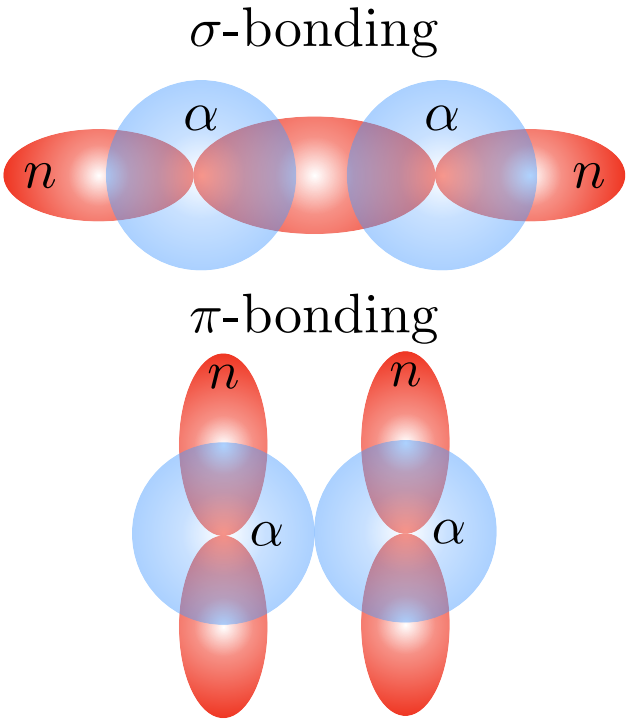

Figure 2.13: A representation of the π and σ bonding or neutrons to the α-particles for ^{10}Be. The ground state manifests as a $(\pi)^2$ configuration, while the 0^+ excited state is expected to manifest as a $(\sigma)^2$ configuration.

2.3.3 Antisymmetrized Molecular Dynamics (AMD)

Antisymmetrized molecular dynamics (AMD) is a useful theoretical tool for studying cluster structures. In AMD, the basis wave function is that which describes an A nucleon system Φ and is formulated by a Slater determinant, which is an expression that satisfies the antisymmetry requirements of the Pauli principle, of single particle wave functions φ_i as [31, 32]

$$\Phi_{AMD}(Z) = \frac{1}{\sqrt{A!}}\mathcal{A}\{\varphi_1, \varphi_2, ..., \varphi_1\}, \tag{2.57}$$

with $\mathcal{A}$ being the antisymmetrization operator and,

$$\varphi_i = \phi_z \chi_i \tau_i, \tag{2.58}$$

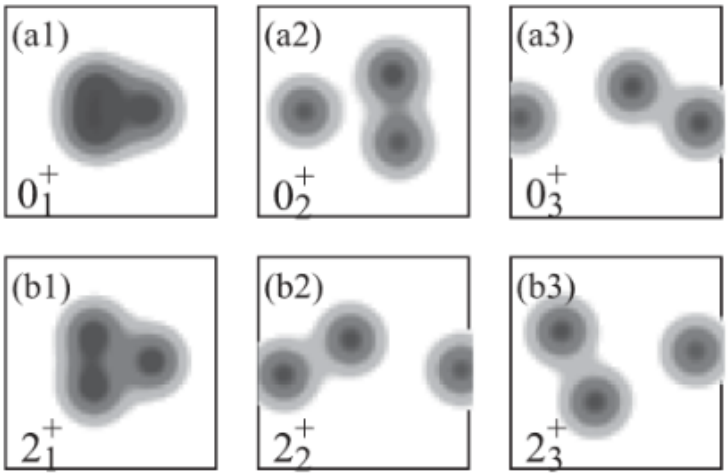

Figure 2.14: AMD calculations showing density distributions for the first few excited states in ^{12}C. Image taken from Ref. Reprinted with permission from [31].

where ϕ is the spatial part, χ is the spin and τ the isospin components of the wave function. The spatial part is defined by a Gaussian wave packet centered at $\mathbf{Z}_i/\sqrt{\nu}$ as

$$\phi_{z_i} \propto \exp\left[-\nu\left(\mathbf{r}_j - \frac{\mathbf{Z}_i}{\sqrt{\nu}}\right)\right], \tag{2.59}$$

where ν is the diffuseness of the Gaussian. This wave function is then used to minimize the energy by varying $\mathbf{Z}$. The energy-minimized wave function can then be used to study the properties of a given state. AMD has successfully been used in cluster physics. The results of an AMD density distribution calculation for some of the excited states of ^{12}C are shown in Figure 2.14. This shows strong evidence of clustering, including a highly-clustered Hoyle state (^{12}C(0_2^+)) without assuming any clustering *a priori*. We can see the ^{8}Be + α structure for the higher order states.

For neutron rich isotopes of beryllium, theoretical frameworks such as molecular-orbital models and AMD have been used to study the cluster structure. While molecular-orbital models assume the existence of $\alpha + \alpha$ clusters *a priori*, AMD makes no such assumptions. Despite this, AMD calculations show a clear cluster structure with $\alpha + \alpha$ core surrounded

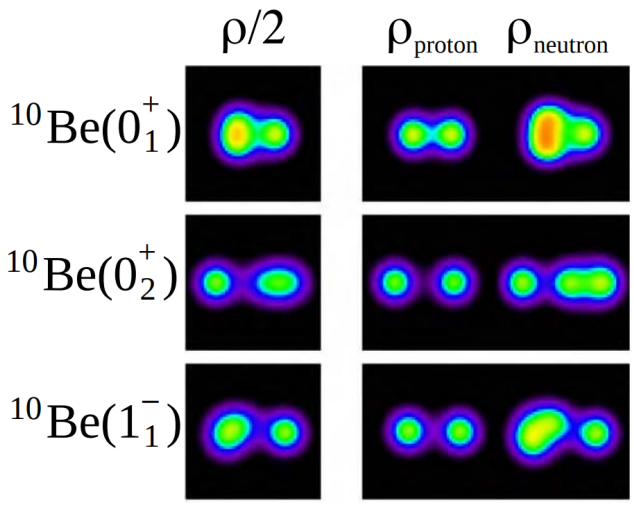

Figure 2.15: Density distributions for the band-head states of ^{10}Be calculated using AMD. The integrated densities of matter and the proton and neutron densities are shown in the left and right panels respectively. Reprinted from [32] (CC BY).

by valence neutrons for molecular orbitals in low lying states [32].

For the specific case of ^{10}Be, AMD calculations show the valence neutron configurations of ^{10}Be(0^+_1), regarded as π^2, ^{10}Be(1^-), regarded as $\pi\sigma$, and ^{10}Be(0^+_2), regarded as σ^2. This means that in the case of π^2, both the valence neutrons occupy the π orbitals; $\pi\sigma$ is where one valence neutron occupies the π oribital and the other occpuies the σ orbital; and in σ^2 both the valence neutrons occupy the σ oritals. The density distributions for some states in ^{10}Be are shown in Figure 2.15 and the spatial density distributions of the π^2 and σ^2 orbitals are shown in Figure 2.16.

2.3.4 Resonating group method

Resonating group method (RGM) comes about from the coupling of many-body structures to cluster reactions [33, 34]. This method has been successful in describing structure-reaction interface in microscopic many-body calculations. RGM describes the nucleus as a clustered state, while providing a microscopic description for the cluster fragments while using an antisymmetrized wave function.

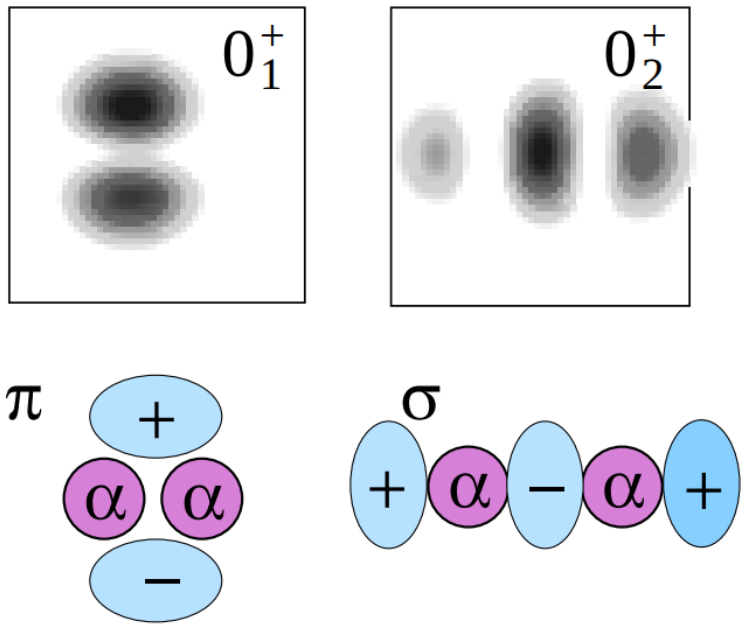

Figure 2.16: Spatial density distributions for valence neutrons in ^{10}Be(0_1^+) and ^{10}Be(0_2^+). These occupy the π and σ orbitals respectively. A representation of the π and σ orbitals are shown with the $\alpha + \alpha$ core. Reprinted from Ref. [32] (CC BY).

We can construct the variational channel wave function,

$$|\Psi^{(\zeta,\mathrm{RGM})}\rangle = \sum_n \chi_n \, |\Phi_{n\zeta}\rangle \,, \tag{2.60}$$

where χ_n is the RGM equation for the amplitudes, and can be written as

$$\sum_{n'} \mathcal{H}_{nn'} \chi_{n'} = E \sum_{n'} \mathcal{N}_{nn'} \chi_{n'}, \tag{2.61}$$

and ζ is the asymptotic channel. In Equation 2.61, $\mathcal{H}$ is the Hamiltonian, $\mathcal{N}$ is the norm kernel and χ is a variational amplitudes vector. The kernels of the matrix in the channel basis are:

$$\mathcal{H}_{nn'\langle\Phi_{n\zeta}|H|\Phi_{n'\zeta}\rangle}, \quad \mathcal{H}_{nn'\langle\Phi_{n\zeta}|\Phi_{n'\zeta}\rangle} \tag{2.62}$$

The RGM wave functions derived in this form obey the symmetries of the Hamiltonian

and are fully antisymmetrized. This wave function can further be used to enhance the spectroscopic factor definition as

$$\mathcal{S}^{(\mathrm{RGM})}_{\beta,\zeta} \equiv |\left\langle \Psi^{(A)} | \Psi^{(\zeta,\mathrm{RGM})} \right\rangle|^2, \tag{2.63}$$

where β represents a particular RGM solution to Equation 2.61.

2.4 Clustering in beryllium isotopes

As extolled in Section 2.3.2, clustering phenomena play an important role in structure of light nuclei, and has been studied extensively [35].

2.4.1 ^{8}Be

The simplest case of an α-core cluster structure is ^{8}Be. With a deformation of 2:1 [9], a dumbbell like deformation appears. This has a well defined cluster structure and a rotational band built on the ground state. ^{8}Be is positioned above the $\alpha + \alpha$ threshold as per Ref. [29] (see Figure. 2.8) Ikeda suggested the cluster structures would appear about the cluster breakup thresholds [29]. This can be seen here with the ^{8}Be nucleus as the predicted energies of the cluster states and the B(E2) electromagnetic transition strengths are in agreement with experimental data. This can be used to measure the width, which can be used to examine the ratio to the Wigner limit. The moment of inertia gives you the alpha-alpha separation distance.

2.4.2 ^{9}Be

When a neutron is added to a ^{8}Be nucleus, it forms a stable ^{9}Be nucleus. The additional valence neutron forms either π or σ type orbitals about the $\alpha + \alpha$ core, thus increasing the binding energy, resulting in a stable nucleus in its ground state. There are three known rotational bands in ^{9}Be. Experimental evidence has shown the ground state of ^{9}Be ($3/2^-$) to form π-type orbital. This is the most compact arrangement, and therefore has a small deformation and moment of inertia. The first excited state, $1/2^+$, forms a σ-type orbital

configuration. This is more deformed and thus has a larger moment of inertia. Consistent with Figures 2.13 and 2.16, the σ type orbital formed by this $1/2^+$ state has a higher neutron density in the center that acts to separate the $\alpha + \alpha$ core. The known spectrum of ^{9}Be less than 12 MeV has been separated into three rotational bands [36].

2.4.3 ^{10}Be

The role of clustering in ^{10}Be has been a subject of extensive experimental and theoretical scrutiny for the past four decades, since the Molecular Orbital (MO) model was introduced to describe the structure of neutron-rich Be and B isotopes [12, 13, 14]. The dimer $\alpha + \alpha$ structure of ^{10}Be bound states has been qualitatively discussed by W. von Oertzen in Ref. [15] and confirmed by microscopic antisymmetrized molecular dynamics (AMD) calculations [16], that do not make any *a priori* assumptions of clustering. A detailed review paper on the chemical bonding (molecular-like) structures in ^{10}Be and ^{12}Be has been published by Ito and Ikeda [37].

It is generally believed that the level structure of ^{10}Be can be described reasonably well as having the two-center α+α structure bonded together by two neutrons that are orbiting the two α-particle clusters. The single-particle levels of neutrons in this two-center system are then analogous to the molecular orbitals of electrons in diatomic molecules like H_2. The levels in ^{10}Be can then be assigned to specific molecular orbital configurations. For example, the ground state of ^{10}Be would correspond to the $(\pi^-_{3/2})^2$ configuration, in which both neutrons orbit the two-center α+α system in the plane perpendicular to the axis that connects the two α-particles (see [37] for a detailed discussion). Of particular interest for this work is the $(\sigma^+_{1/2})^2$ MO configuration that corresponds to the two neutrons orbiting the two α-particles along the α+α axis. The inter-cluster distance for this configuration is large due to energy gain associated with the increased radius of $\sigma^+_{1/2}$ orbitals. The moment of inertia of the states that belong to this rotational band is therefore large compared to the ground state. Using the more conventional language of shell model, in the limit of zero inter-cluster distance, the $(\sigma^+_{1/2})^2$ configuration becomes $\nu(2s1d)^2$, or $(1p)^4(2s1d)^2$ if p-shell nucleons are included. The

2-particle-2-hole (2p2h) configuration in ^{10}Be is illustrated in Figure 2.17.

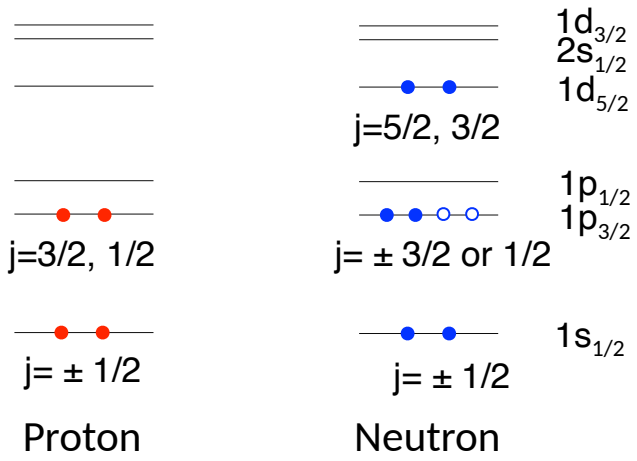

Figure 2.17: The 2p2h configuration in ^{10}Be that presumably dominates for the states in the α:2n:α rotational band.

There is strong experimental evidence that some states in ^{10}Be exhibit molecular-like α:2n:α configuration [38]. Theoretically, these exotic structures can be explored microscopically in the antisymmetrized molecular dynamics plus Hartree-Fock approach [39] or in a Molecular Orbital model [30]. Based on these theoretical studies, it appears that the 6.179 MeV 0^+ state in ^{10}Be has a pronounced α:2n:α configuration with an α-α inter-distance of 3.55 fm. This is 1.8 times more than the corresponding value for the ^{10}Be ground state. The 2^+ at 7.542 MeV in ^{10}Be is believed to be the next member of this rotational band [40].

The state at 10.2 MeV was identified as the next 4^+ member [41]. This state was confirmed by [42] using a ^{7}Li(^{7}Li,α) reaction. While alternative, 3^-, spin-parity assignments has been made for this state before from the correlation of α + ^{6}He particles following the α decay [43], we believe that the later experiments [18, 17] provide a more reliable 4^+ spin-parity assignment. Ref [18] made the spin-parity assignment from a ^{6}Li(^{6}He,d)^{10}Be measurement, while Ref. [17] performed a measurement to populate the 10.2 MeV state in ^{10}Be using the ^{6}He + α resonant scattering. Subsequently two more ^{6}He + α resonant scattering experi-

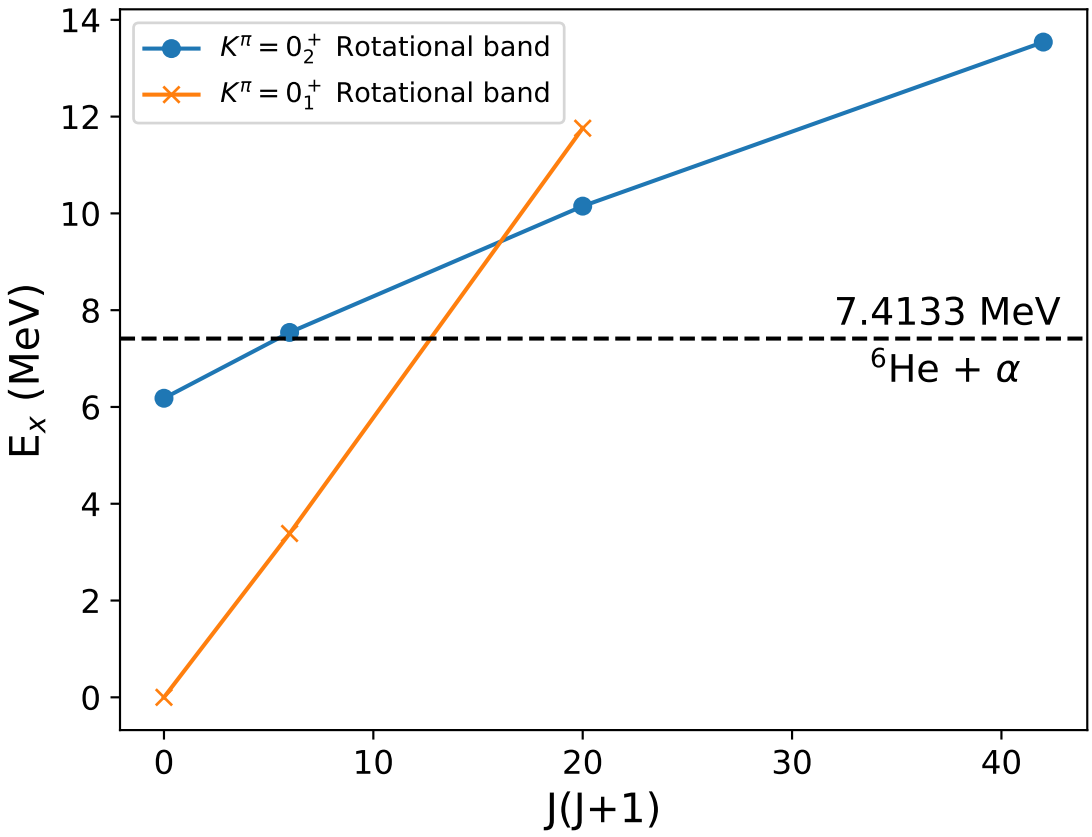

Figure 2.18: The energy-spin systematics for states in the $K^\pi = 0_1^+$ and $K^\pi = 0_2^+$ rotational band. The excitation energies are plotted as a function of the angular momentum $J(J+1)$.

ments were performed by [19, 44], further confirming the existence of the 4^+ member of the $K^\pi = 0_2^+$ rotational band.

Experimental data on α-reduced widths [17] and spectroscopic factors for the 6.179, 7.542, and 10.2 MeV states are consistent with the highly-clustered nature of these states and support assigning them to a single rotational band. Provided that these three states are indeed the members of the same rotational band, the moment of inertia of this band is very large, which supports the molecular-like α:2n:α picture for this band. However, the 4^+ at 10.2 MeV is not the band-terminating state. The algebraic model based on SU(3) symmetry [45] predicts that this rotational band (with the bandhead at 6.179 MeV) should

be designated as (λ,μ)=(8,0) and therefore should contain the 6^+ and 8^+ states, which are predicted to be the yrast states (lowest energy for a given angular momentum) in ^{10}Be. Experimental observation of the 6^+ state and a measurement of its width is the main goal of this work. Figure 2.18 shows the energy-spin systematics of the rotational bands built on the 0^+ ground state as well as the 0_2^+ bandhead at 6.18 MeV. The first indication for a structure that could be interpreted as a relatively narrow high-spin, positive parity state at 13.4 MeV excitation energy in ^{10}Be were obtained in the excitation function for ^{6}He+α resonance elastic scattering measured at angles close to 90° in the center of mass (c.m.) [46, 44]. The excitation function from this measurement at 90° in the center of mass is shown in Figure 2.19. Due to a limited measured angular range and the dominance of what

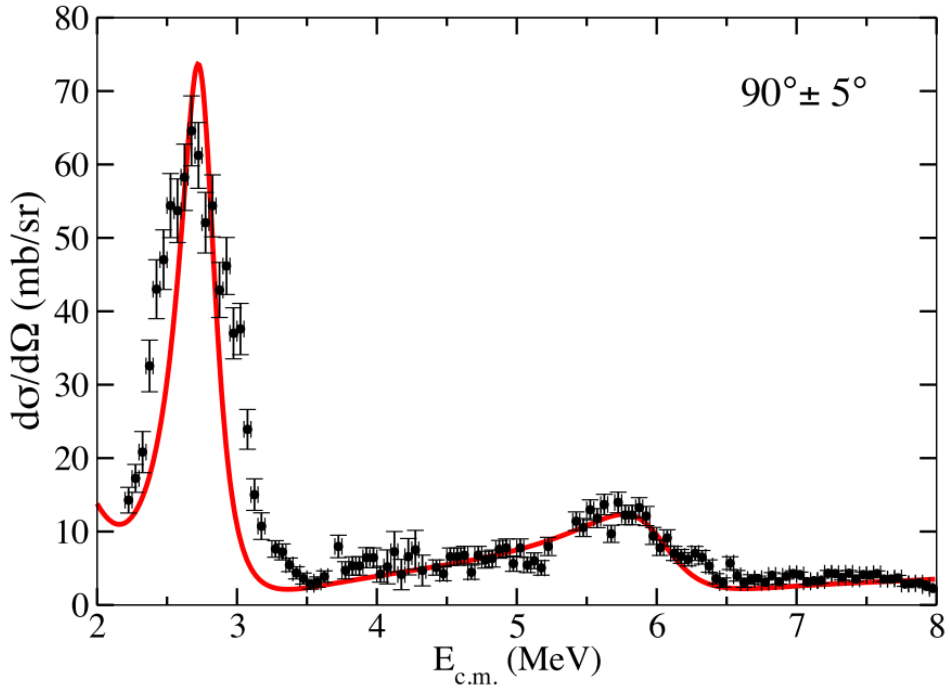

Figure 2.19: Excitation function for ^{6}He+α resonance elastic scattering at 90° ± 5° between 2-8 MeV (center of mass). An R-Matrix fit (red line) includes a 4^+ state at $E_{c.m.}$ = 2.79 MeV and a 6^+ state at $E_{c.m.}$ = 6.13 MeV. A broad 0^+ resonance at lower energy and a broad 2^+ at higher energy were included in the fit. Reprinted with permission from Ref. [44].

appears to be non-resonant elastic scattering, the authors of [46] were not able to make firm conclusions and they made a statement that "new experimental data at angles close to 180° may be necessary to confirm or rule out the existence of this state". There have been more observations of a state around 13 MeV more recently. It was observed in ^{10}Be breakup to α and ^{6}He [20, 21]. The tentative spin-parity assignment was performed in [20] and it was consistent with 6^+. A CH_2 target was used to induce the breakup of the incoming ^{10}Be beam ions and they were only sensitive to the elastic channel due to the requirement to measure both ^{4}He and ^{6}He and reconstruct their relative energies. However, their results do not have sufficient statistics to claim there is a state above the strong background, and if there is a state that it is a 6^+. In Figure 2.20, the peak at 13.5 MeV can be seen to have an excess of about 10 counts above a background taken from either side of the peak suggesting perhaps the event mixing does not accurately represent their experimental background. In the angular correlation distribution in [20], we can see that there is an excess of yield at 11.8 MeV at $cos(\phi)$=0.5 and 0.85, which is what the 6^+ assignment at 13.5 MeV is based on. There is also no background angular distribution study included in Ref. [20]. Calculations from Ref. [47] show that this state would be dominant in the inelastic channel. Since this measurement is not sensitive to the inelastic channel, the yield of the state at 13.5 MeV would be expected to be considerably smaller than that of the 4^+ state seen here although the two peaks are of the same order of magnitude.

The experimental data presented here provide a stringent test on the existence of a highly-clustered 6^+ by measuring the excitation function for ^{6}He+α elastic scattering at angles where the state should have highest cross section - close to 180° in c.m (0° in the lab. reference frame).

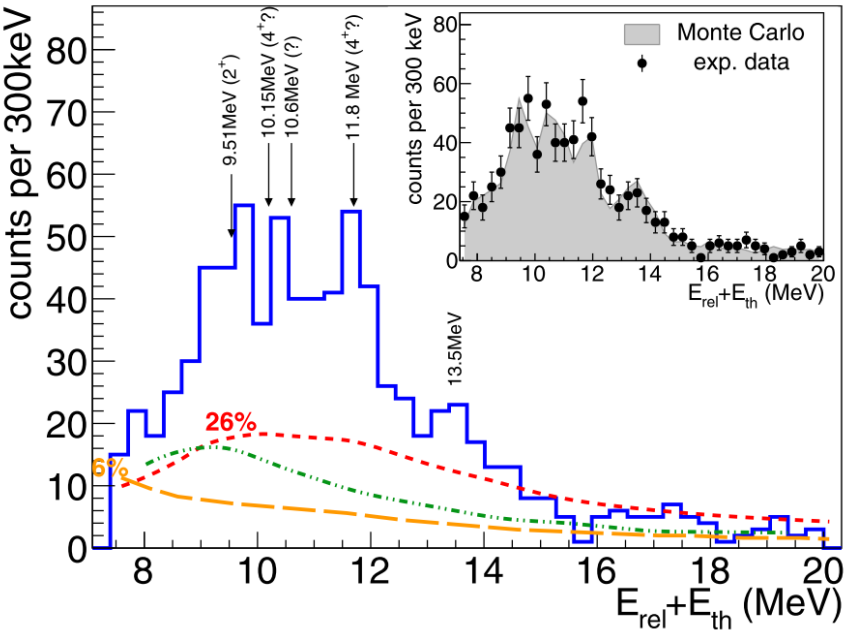

Figure 2.20: ^{10}Be relative energy spectrum from the $\alpha+^{6}$He decay channel. The dashed lines represent the simulated detection efficiencies. The red dotted line assumes hydrogen recoil. Orange dashed line assumes carbon recoil. The green dashed line represents the estimated background by an event mixing procedure. The inset is the Monte Carlo simulation compared to experimental data. Reprinted with permission from Ref. [20].

3. EXPERIMENT

To probe the cluster structure of ^{10}Be, looking for the highly clustered 6^+ state with the ^{6}He(α,α) reaction, an experiment was performed at the Texas A&M University Cyclotron Institute. The goal was to further probe the broad peak of the ^{6}He+α excitation function at $E_{c.m.} = 6.0$ MeV observed in [46] but at angles close to $\theta_{c.m.} = 180^\circ$ where the highly clustered 6^+ state should have a strong maximum in its cross section. A primary beam of ^{7}Li at 60 MeV was produced using the K150 cyclotron. The ^{7}Li primary beam was impinged on a liquid nitrogen cooled gas cell filled with D_2, yielding ^{6}He ions via the d(^{7}Li,^{6}He)^{3}He reaction with an energy of 35.4 MeV. The ^{6}He, our beam of interest, was then selected by the Momentum Achromat Recoil Spectrometer (MARS) [48] (Figure 3.1).

3.1 MARS: A momentum achromat recoil spectrometer

MARS was designed for use with cyclotrons available at the Cyclotron Institute at Texas A&M University. The optics were designed to work well for reactions in inverse kinematics. As the primary beam from either of the two cyclotrons (K150 or K500, see Figure 3.2) enters the MARS setup. The SW1 and SW2 dipole magnets form a beam swinger, allowing a deflection angle ranging from 0° to 30°. These magnets are located just upstream of the target chamber (MARS gas cell). The gas cell was filled with D_2 gas at 1,604 Torr and was cryogenically cooled using liquid nitrogen to 77 K. The entrance and exit windows of the target chamber comprised of 0.16 mil (4 μm) Havar.

The primary target chamber is followed by quadrupoles Q1, Q2 and Q3 along with dipoles D1 and D2, which produce an achromatic beam as well as a nearly parallel transport into the velocity filter (Wien filter) V1. The velocity filter can select for velocities based on the electric and magnetic fields. The force experienced by a charged particle (q) in an electric field ($\vec{E}$) is given by:

$$\vec{F} = q\vec{E}. \tag{3.1}$$

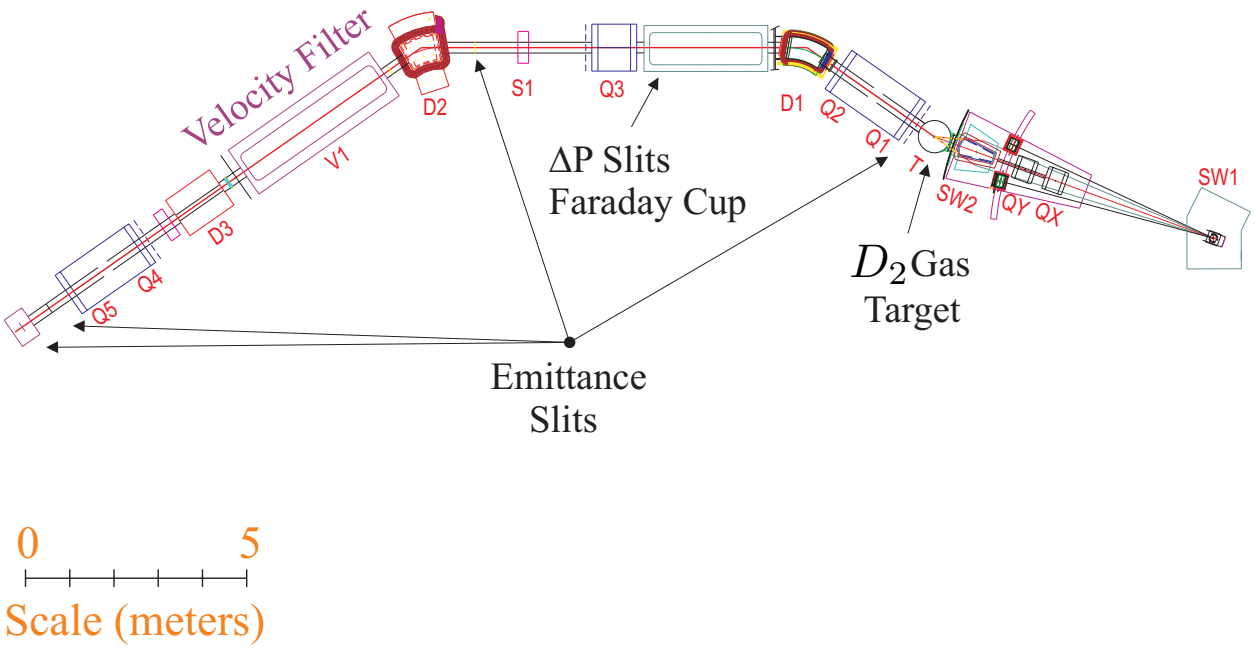

Figure 3.1: Momentum Achromat Recoil Spectrometer (MARS) layout is shown here. MARS is used to produce and separate radioactive nuclei. Radioactive beams are produced with MARS using inverse kinematic reactions with the primary beam being the heavy projectiles that are furnished by either the K150 or the K500 cyclotron [48].

The force experienced by a charged particle (q) in a magnetic field ($\vec{E}$) is given by:

$$\vec{F} = q\vec{v} \times \vec{B}, \tag{3.2}$$

where $\vec{v}$ is the velocity of the particle. In a velocity filter, the magnetic field is always perpendicular to the velocity of the particle. Therefore, Eq. 3.2 simplifies to

$$F = qvB \tag{3.3}$$

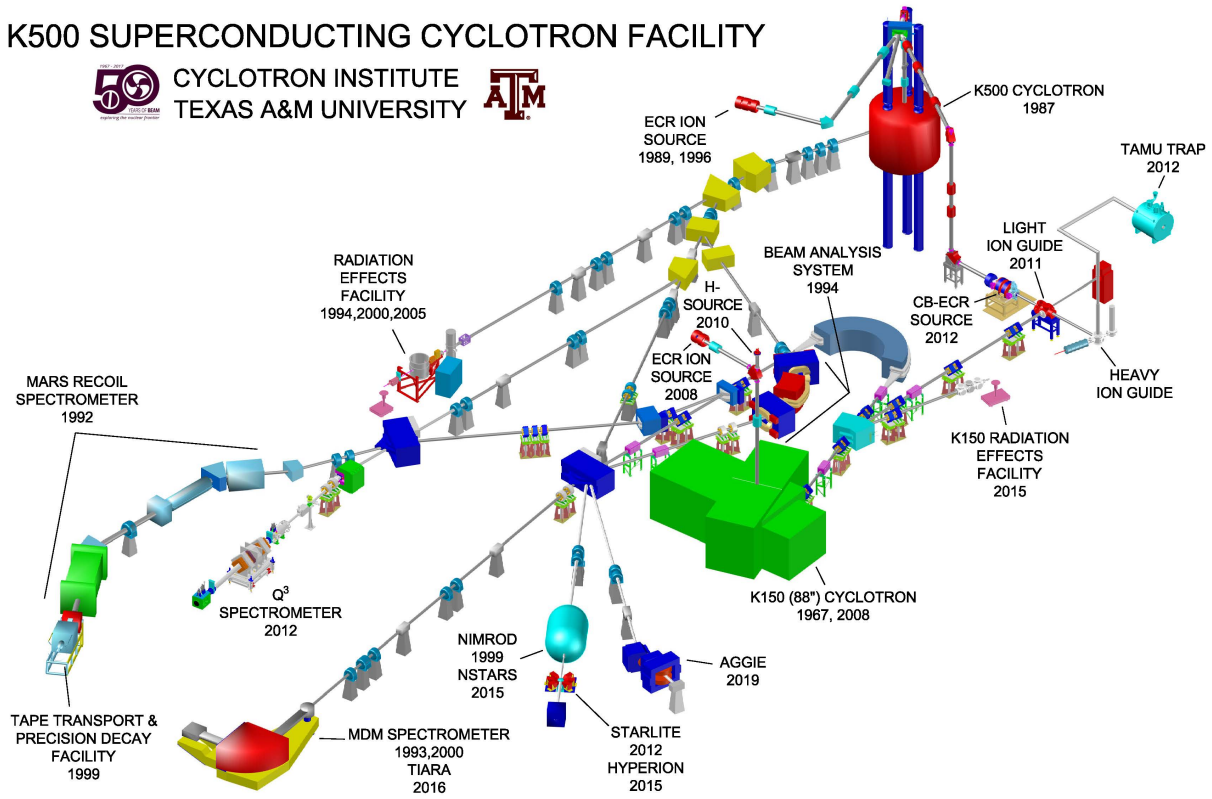

Figure 3.2: Schematic of the Cyclotron Institute at Texas A&M University. This shows the two cyclotrons (K150 and K500) at this facility as well as all the research facilities, spectrometers and detectors [49].

Setting the two forces equal to each other yields:

$$v_f = \frac{E}{B}. \tag{3.4}$$

This means that tuning the $\vec{B}$ field and $\vec{E}$ field will allow particles with velocity $\vec{v}_f$ through. Once past the velocity filter, the beam is bent upwards by the D3 dipole magnet before being focused by the final quadrupole magnets, Q4 and Q5, providing focus in both the vertical and horizontal planes. This gives the first order M/q focus where M is the mass of the particle and q is the charge.

Momentum slits are placed after the quadrupole magnet Q3 in order to define the mo-

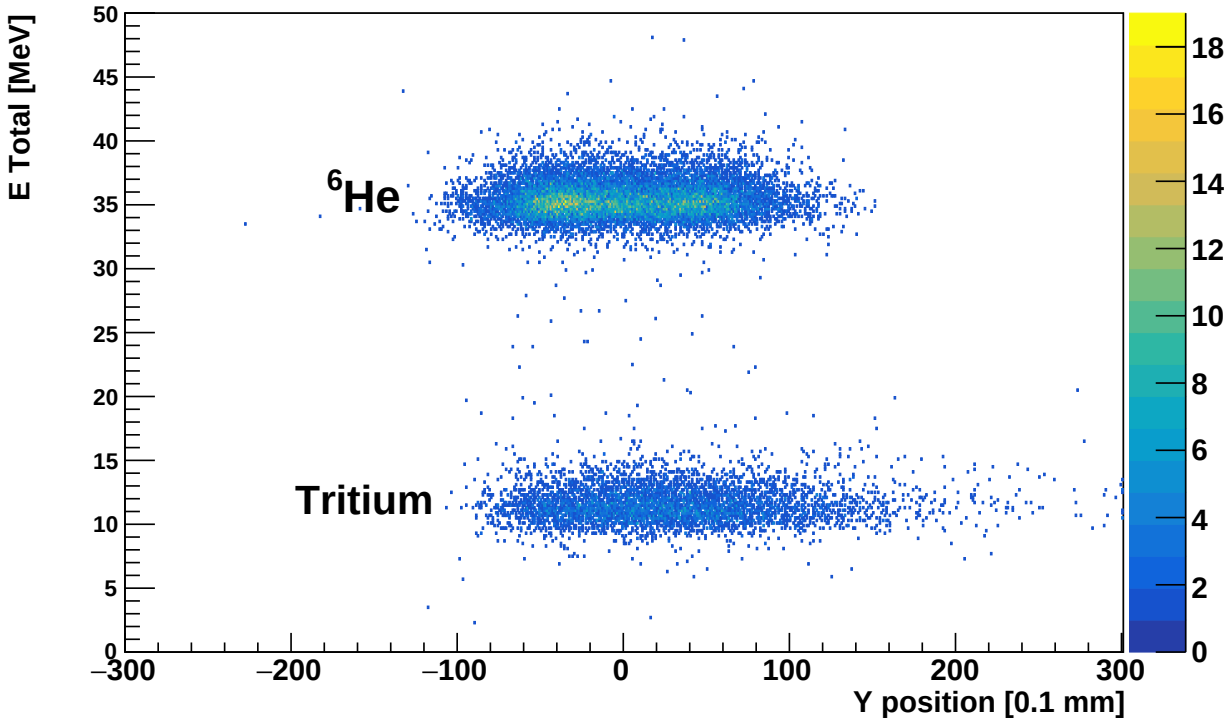

Figure 3.3: Result of the ^{6}He MARS production showing the main contaminant, tritium, at the same focal plane as the ^{6}He. Adapted from Ref. [50].

mentum acceptance of the system and eliminate the primary beam. MARS has a mass resolution of $\delta M/M \simeq 1/300$, and an energy acceptance of $\pm 9\%$ $\Delta E/E$ and a geometric angle of up to 9 milli-steradians [48].

For this experiment, the secondary beam of ^{6}He was produced in inverse kinematics using the d(^{7}Li,^{6}He)^{3}He transfer reaction with a 7 MeV/u ^{7}Li primary beam from the K150 cyclotron. A production rate of 397 events/nC was achieved with the MARS momentum slits at ± 1.5 mm, resulting in a momentum spread of the Δp/p$\approx$ 1.8%. The result was a 35.4 MeV ^{6}He beam. A significant tritium (^{3}H) contamination was present in the secondary beam. The production plot along with the tritium contaminant can be see in Figure 3.3.

3.2 Thick target inverse kinematics technique

The Thick Target Inverse Kinematics (TTIK) approach was used for this experiment. This method was pioneered by Goldberg *et al.* [51] to measure a range of excitation energies for resonance scattering reactions. In a non-TTIK approach, one must aggregate measurements with various beam energies to measure different excitation functions. TTIK accomplishes this by using inverse kinematics ($A_{beam} > A_{target}$), where the target is usually a gas medium (helium (96%) + CO_2 (4%) gas admixture for this measurement).

With the TTIK technique, a heavier beam particle is impinged on a lighter target. As the beam traverses through the target, it looses energy by ionizing the target atoms. The target thickness, or in our case, pressure of the target gas can be adjusted so that the beam ions can achieve the range of excitation energies desired. When a beam ion interacts with a target nucleus, some kinetic energy is transferred from the heavy projectile to the light recoil (^{6}He and α-particles respectively). The light recoil (α-particle) will lose less energy traversing through the target medium than the heavy recoil will. The light recoil particles are measured by a detector at the end of the chamber. The energy of the light recoil particle measured is related to the energy of the beam ion at the vertex location, as well as scattering angle. If there is a resonance present in the excitation function, an increased yield will be observed in the spectrum of light nuclei. If a scattering vertex can be ascertained, one can account for the energy losses of the light recoil particles and extract the excitation function. Another advantage to this technique is the ability to measure at forward angles since the beam can be stopped in the gas. This is an important advantage, since this allows measurements at backward angles in the center of mass frame as described by Eq. 3.5.

$$\theta_{c.m.} = 180^\circ - 2\theta_{lab} \tag{3.5}$$

However, given the similarity in the masses of our beam and target ions, we were unable to capitalize on this. Another advantage of TTIK is the ability to reach lower excitation

energies in the excitation function. At a given center of mass energy, the energy of the recoil particle is around four times greater in inverse kinematics compared to traditional geometry. This makes it easier to measure lower excitation energies. The center of mass energy for traditional and inverse kinematics are as follows:

$$E_{c.m.} = E_{beam}\frac{M}{m+M} \ , \tag{3.6}$$

and

$$E_{c.m.} = E^{'}_{beam}\frac{m}{m+M} \ , \tag{3.7}$$

where E and $E^{'}$ are the beam energies in traditional and inverse geometries, respectively, m and M are the masses of the light and heavy particles, respectively. The lab energies of the light recoil in traditional and inverse kinematics are given by:

$$E_m = E_{beam}\frac{m^2}{(m+M)^2}\left[cos(\theta_{lab}) + \sqrt{\left(\frac{M}{m}\right)^2 - sin^2(\theta_{lab})}\right]^2 \tag{3.8}$$

and

$$E^{'}_m = E^{'}_{beam}\frac{4mM}{(m+m)^2}cos^2(\theta_{lab}). \tag{3.9}$$

If we assuming forward angles in the lab frame, and if we divide $E^{'}_m$ by E_m we arrive at,

$$E^{'}_m = 4E_m\frac{(M/m)^2}{(1+M/m)^2} \ . \tag{3.10}$$

Equation 3.10 can be approximated to $4E_m$ (if $M >> m$). This shows that for the same center of mass energy, the light recoil particle is nearly four times greater for inverse kinematics, compared to traditional geometry.

Since the target medium is usually a gas, there are some drawbacks of using this technique. These drawbacks include energy spread and angular divergence of the beam as well as straggling of the light recoil particles. This results in deteriorating resolution as the scat-

tering angle increases. With the advent of active target detector systems, the relevance of these disadvantages of the TTIK technique are diminishing rapidly. Further details of our experimental setup and conditions is detailed in Section 3.3.

3.3 Experimental setup

The ^{6}He beam entered the scattering chamber, filled with a helium (96%) + CO_2 (4%) gas admixture at 1700 Torr (and low pressure runs at 1100 Torr), through a 5 μm Havar window. The scattering chamber consisted of three 5x5 cm Micron MSQ25 silicon detectors, each of which have four independent quadrants to measure the total energy of an impinging charged particles. There were eight position-sensitive proportional counter wires, staggered in two layers, positioned immediately upstream of the silicon detectors. This array of wires were used for particle identification and scattering angle reconstruction. A windowless ionization chamber was also used for overall normalization in addition to beam contaminant identification. There was a removable 2-cm diameter aluminum disk (located upstream of the proportional counter cells) which was inserted after the beam was characterized in order to avoid permanently damaging the silicon detectors and saturating the data acquisition system (DAQ). This disk blocked 95% of the beam. The setup was optimized to measure the elastic and inelastic ^{6}He+α scattering at angles as close to 180° in the center of mass frame as possible. The scattering chamber and the overall schematic of the setup is shown in Figure 3.4.

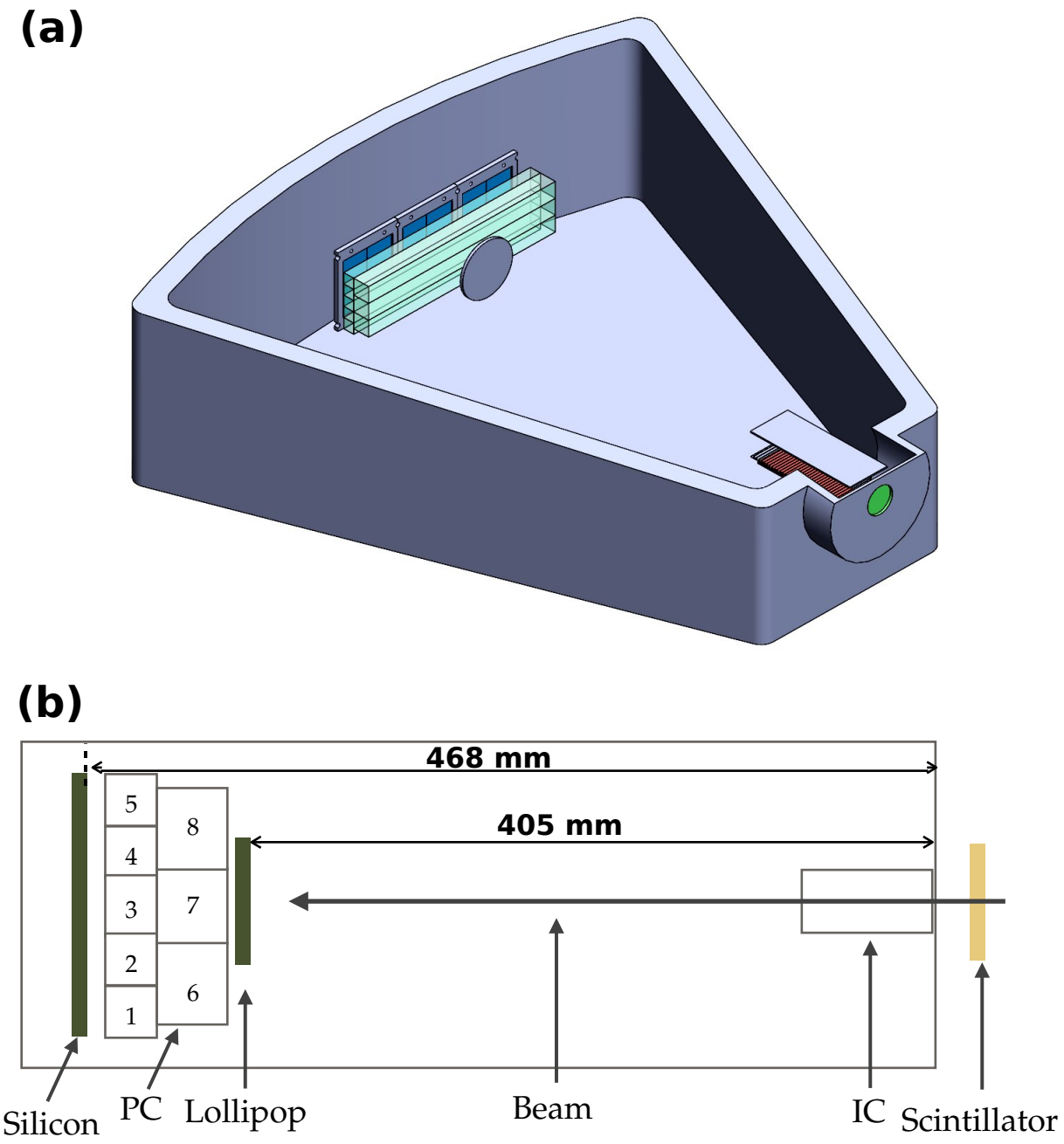

Figure 3.4: (a). CAD rendering of the scattering chamber and detector set up used for this experiment. (b). Cross sectional view of the set up with dimensions from the window to the silicon detectors and the beam stopper. Reprinted with permission from [52].

3.3.1 Scintillator and ionization chamber

The beam first passes through a BC-400 scintillator film of 10 mil (254 μm) thickness, placed at 45° to the beam axis, that is read out by two photomultiplier tubes (PMTs). Scintillators are materials that emit a small flash of light when exposed to radiation. This flash of light is then amplified using a device such as a PMT, which are then converted to electrical pulses and fed into our data stream. Once the beam enters the scattering chamber, it interacts with a windowless ionization chamber. This apparatus consists of an anode, a cathode, and a Frisch-Grid. When a particle traverses through a gas, electron-ion pairs are created along the path. The ionization chamber works by measuring the total charge of these electron-ion pairs. The ionization chamber, used in conjunction with the scintillator allows us to select the particles associated with our beam and cut out the contaminants by measuring the specific energy losses of the different particles. This setup is further used to count the number of ^{6}He beam ions for overall normalization. Figure 3.5, which plots the scintillator energy vs. ionization chamber energy, shows the ^{6}He beam enclosed within the red contour along with the tritium contaminant.

3.3.2 Proportional counters

Following the ionization chamber and the removable aluminum disk which was used as a beam stopper, are eight position sensitive, resistive proportional counter wires made from carbon fiber. The field near a wire is inversely proportional to the distance (r). As a particle traversing through the gas, it produces ionization. The electrons and ions liberated in the process will be drifted due to the electric field, produced by the high voltage applied to the wires. As the electrons approach a high field region near a wire, they are accelerated to produce an avalanche. Positive ions will be liberated in this process, thus inducing a negative signal on the anode wires, which is then further processed through our electronics setup and integrated into our data stream.

Given that the multi-wire proportional counter functions through the ionization process,

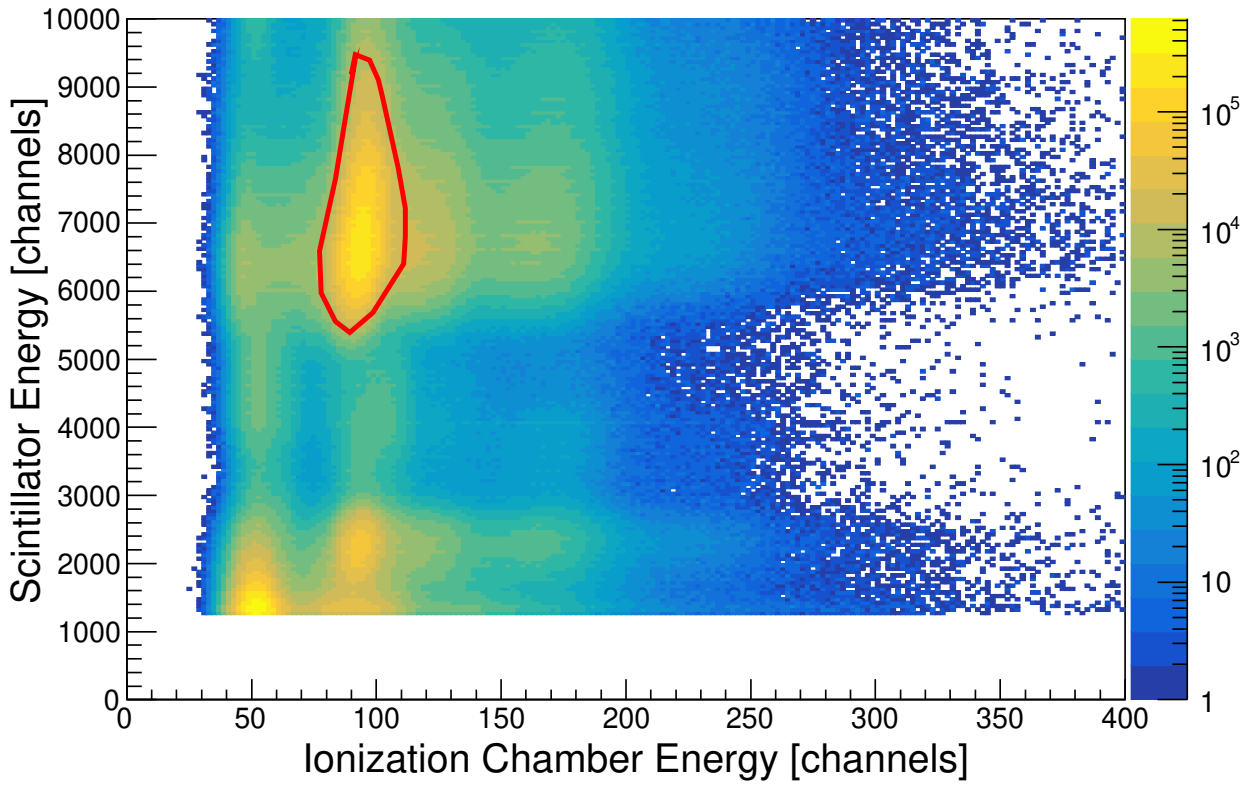

Figure 3.5: The region enclosed within the red line represents the ^{6}He beam particles. Tritium, the main contaminant can be observed at the bottom left of the plot. Reprinted with permission from [52].

it requires a gas to function. Normally, there are several factors that dictate the type of gas that is used for these devices. An ideal gas would have a high gain, and the ability to function at a low voltage. Pure nobel gases are not the ideal candidates due to spurious discharges caused by high energy photons at high gains ($\sim 10^4$). However, since we are using this as an active-target system, which is when the gas in the chamber is used as a target as well as a medium for detection, we are limited to using helium gas. To mitigate this effect we used carbon dioxide gas acting as a quencher. Relatively small amounts of this gas is sufficient to quench the spurious avalanches. In this experiment helium (96%) + CO_2 (4%) gas admixture was used. A schematic of the proportional counter detector is shown in Figure 3.4 [53].

3.3.3 Silicon detectors

There are three MSQ25-1000 Micron Semiconductor silicon (Si) detectors placed at the end of the chamber (CAD representation shown in Figure 3.6). The silicon detectors were used to measure the energy of the recoil particles. Silicon detectors have been around for close to 80 years and have been instrumental in the success of many high-energy experiments. Silicon detectors work as a diode. The difference in energy between the valence band and conduction band, also known as band gap is 1.1 eV (Figure 3.7). These detectors therefore have a great inherent energy resolution. This stems from the fact that energy threshold required to create an electron-hole pair (ionization energy) is as 3.6 eV. This energy is about an order of magnitude lower than the ionization energy of a gaseous detector.

The silicon used for virtually all detection or sensor applications is doped to increase the probability of creating electron-hole pairs. Without these impurities, the valence band is full, while the conduction band is empty. This means that the concentration of electrons in the valence band and holes in the conduction band are the same, creating a charge equilibrium. Since silicon has four valence electrons (group IV), doping can modify the free charge carrier concentration. Silicon can be doped with two different types of materials. Materials with five valence electrons (group V), such as phosphorus can be added, creating a "n-type" silicon. This will create an excess of electrons that can act as charge carriers. The second type of materials are those with three valence electrons (group III) such as boron. These create an excess of holes that can act as charge carriers [54].

The energy deposited in the silicon by any ionizing radiation is acquired by counting the number of electron-hole pairs produced. The noise here is governed by Poisson statistics. The standard deviation is therefore $\sqrt{n}$ for $n >> 1$. However, the detector resolution also has to be scaled by the Fano Factor. Radiation detectors' behavior exhibits fluctuations in the signal that is less than that predicted by Poisson statistics. The Fano Factor is the ratio between observed variance to the Poisson predicted variance. In silicon detector, there are two possible types of collisions that can occur [55, 53]:

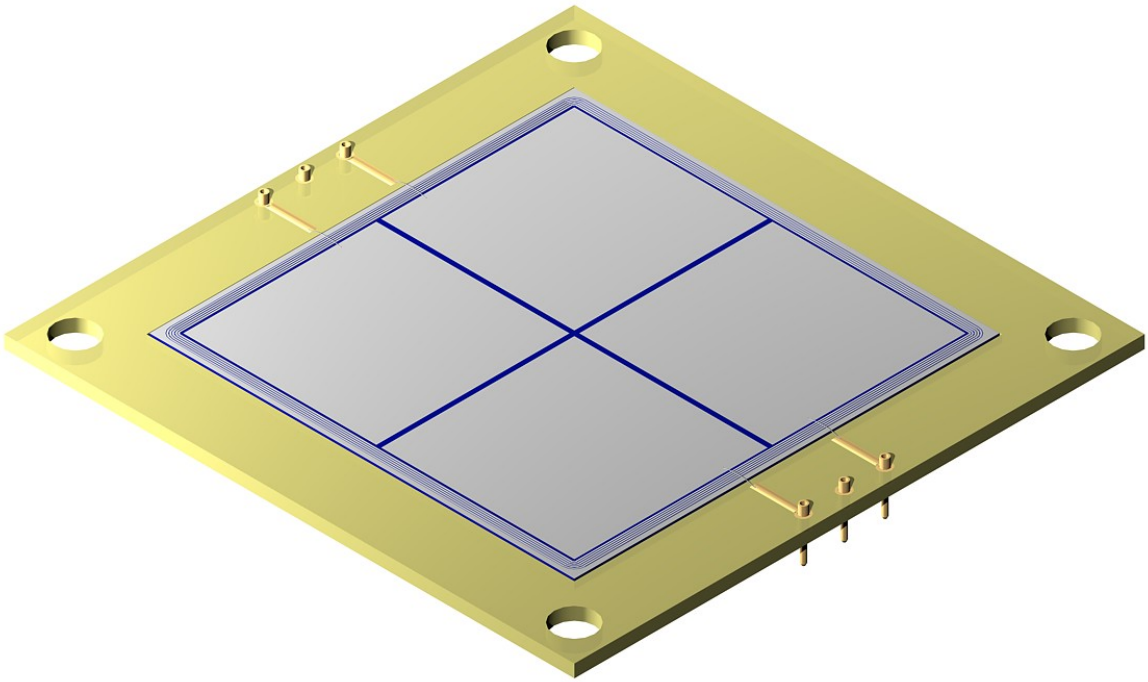

Figure 3.6: CAD representation of the MSQ25-1000 series silicon detector. The four quadrants along with guard-rings on the outer perimeter, wire-bonds, and readout pins are shown here.

(a) Lattice excitations - Phonon production.

(b) Ionization - Formation of electron-hole pairs.

Assuming that n_x excitations produce n_p phonons and n_i ionization interactions produce n_q electron-hole pairs, the average sum of energies deposited by the incident radiation is given by:

$$E_0 = E_i n_i + E_x n_x, \tag{3.11}$$

where E_i and E_x are energies required for a single lattice excitation or a single ionization, respectively. Since, for large numbers, Poisson distribution approaches a normal distribution

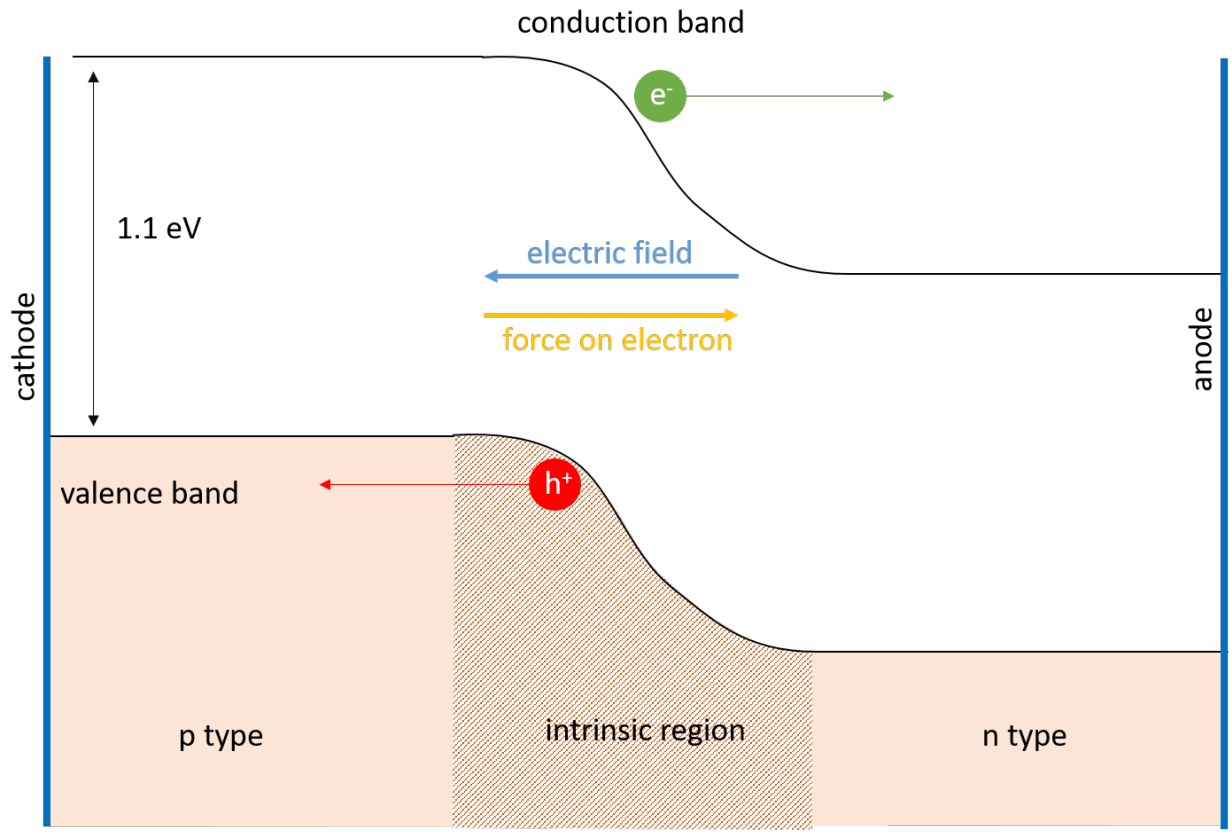

Figure 3.7: Representation of the valence and conduction bands in a silicon detector. This shows the direction of the electric field and the direction of the force on an electron. The electron is drifted towards the anode side, while the hole is drifted towards the cathode side. Reprinted with permission from Ref. [6].

about its mean, we can assume Gaussian statistics. From this, the variance in the number of lattice excitations and ionizations are:

$$\begin{aligned} \sigma_x &= \sqrt{n_x} \quad \text{Lattice excitations,} \\ \sigma_i &= \sqrt{n_i} \qquad\quad \text{Ionizations.} \end{aligned} \tag{3.12}$$

For a given energy deposited, E_0, fluctuations in the lattice excitations and ionizations must balance each other out. If we take the total differential of Eq. 3.11, we get

$$dE_0 = \frac{\partial E_0}{\partial n_x} dn_x + \frac{\partial E_0}{\partial n_i} dn_i = 0 \tag{3.13}$$

Therefore,

$$E_x \Delta n_x + E_i \Delta n_i = 0. \tag{3.14}$$

This ensures that for a given event, if more energy goes into lattice excitation, less energy will be available for charge formation, and vice versa. This will give the proper total energy for the event. When averaging over large statistics, the variances of the two processes must be equal:

$$E_i \sigma_i = E_x \sigma_x. \tag{3.15}$$

Substituting Eq. 3.12:

$$\sigma_i = \frac{E_x}{E_i} \sqrt{n_x}. \tag{3.16}$$

From Eq. 3.11, we get:

$$n_x = \frac{E_0 - E_i n_i}{E_x}, \tag{3.17}$$

giving us

$$\sigma_i = \frac{E_x}{E_i} \sqrt{\frac{E_0}{E_x} - \frac{E_i}{E_x}\frac{E_0}{\epsilon_i}}. \tag{3.18}$$

Since each ionization creates an electron-hole pair that contributes to the signal, we have:

$$n_i = n_Q = \frac{E_0}{\epsilon_i}, \tag{3.19}$$

where ϵ_i is the average energy needed to produce an electron-hole pair, and n_Q is the number of charge pairs. From this, we have:

$$\begin{aligned} \sigma_i &= \frac{E_x}{E_i} \sqrt{\frac{E_0}{E_x} - \frac{E_i}{E_x} n_i} \\ &= \sqrt{\frac{E_0}{\epsilon_i}} \cdot \underbrace{\sqrt{\frac{E_x}{E_i}\left(\frac{\epsilon_i}{E_i} - 1\right)}}_{\text{Fano factor } F}. \end{aligned} \tag{3.20}$$

We can thus rewrite Eq. 3.20 as:

$$\sigma_Q = \sqrt{F n_Q}. \tag{3.21}$$

The nominal Fano factor is 0.1 for silicon detectors [56, 53]. This means that the variance of the signal is significantly smaller than that expected through Poisson statistics [57]. In addition to this, leakage currents in the detector and electronic noise also limit the sensitivity and detection efficiency of the detector by requiring a high energy threshold to avoid erroneous triggering.

To acquire a signal out of the silicon detector, we apply a reverse bias voltage, creating an equilibrium throughout the bulk preventing the electron-hole pairs from being reabsorbed. This also ensures that the electrons and holes are drifted to the anode and cathode regions, where their charge can be collected and read out for further processing. The current signal this creates is then sent out to a preamplifier, followed by a shaper, which is then digitized and integrated into our data stream.

3.4 Calibration

3.4.1 Silicon detectors calibration

The three silicon detectors were calibrated using a four-line α-source containing four radioactive isotopes with well defined energy peaks. The isotopes and their corresponding weighted average energies are: ^{148}Gd - 3.117 MeV, ^{239}Pu - 5.147 MeV, ^{241}Am - 5.474 MeV, and ^{244}Cm 5.787 MeV. The calibrations for these detectors are done on a quadrant by quadrant basis. These peaks in the silicon detector spectra are fit with Gaussian functions. The preamplifier used for the silicon detectors was linear, thus a linear fit was done to extract a function that converts raw channel number to MeV. An example of the calibration run with the four-line α-source is shwon in Figure 3.8.

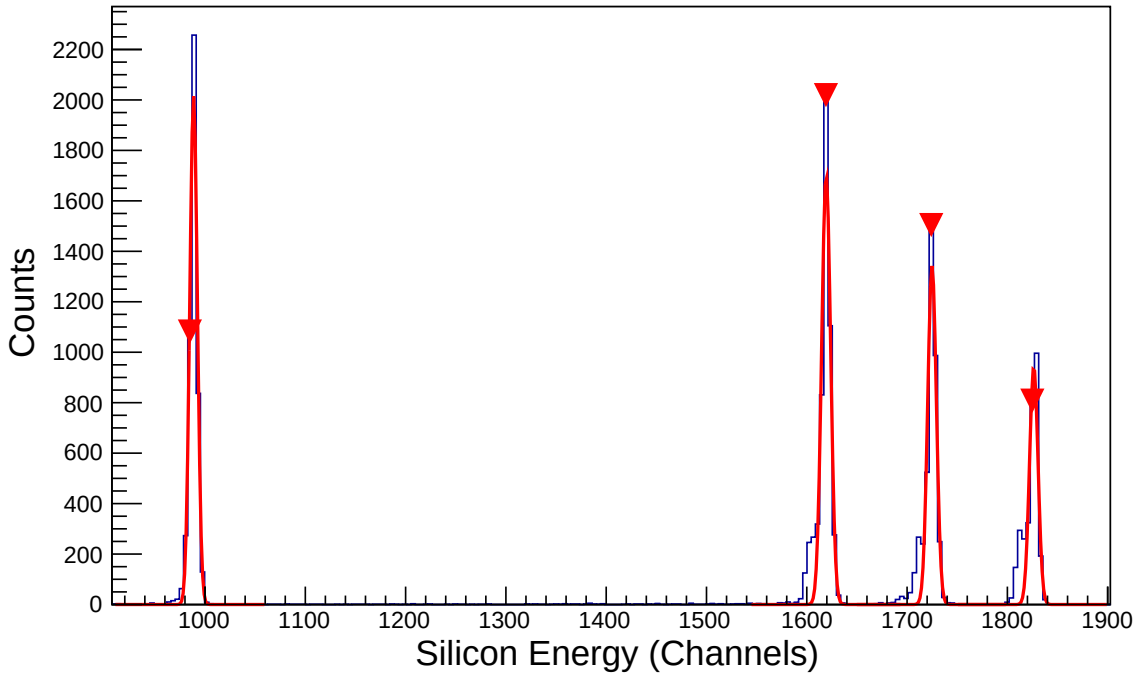

Figure 3.8: Calibration data from the four-peak alpha source with weighted averages of 3.11 MeV, 5.147 MeV, 5.474 MeV and 5.787 MeV for ^{148}Gd, ^{239}Pu, ^{241}Am and ^{244}Cm respectively, fit with Gaussian functions. The mean of the Gaussian function was then used as the corresponding channel number for the corresponding α-particle energy for the calibration. The red arrowhead indicating a peak is from the peak finding routine in ROOT. This technique was used as an ansatz for the Gaussian fit.

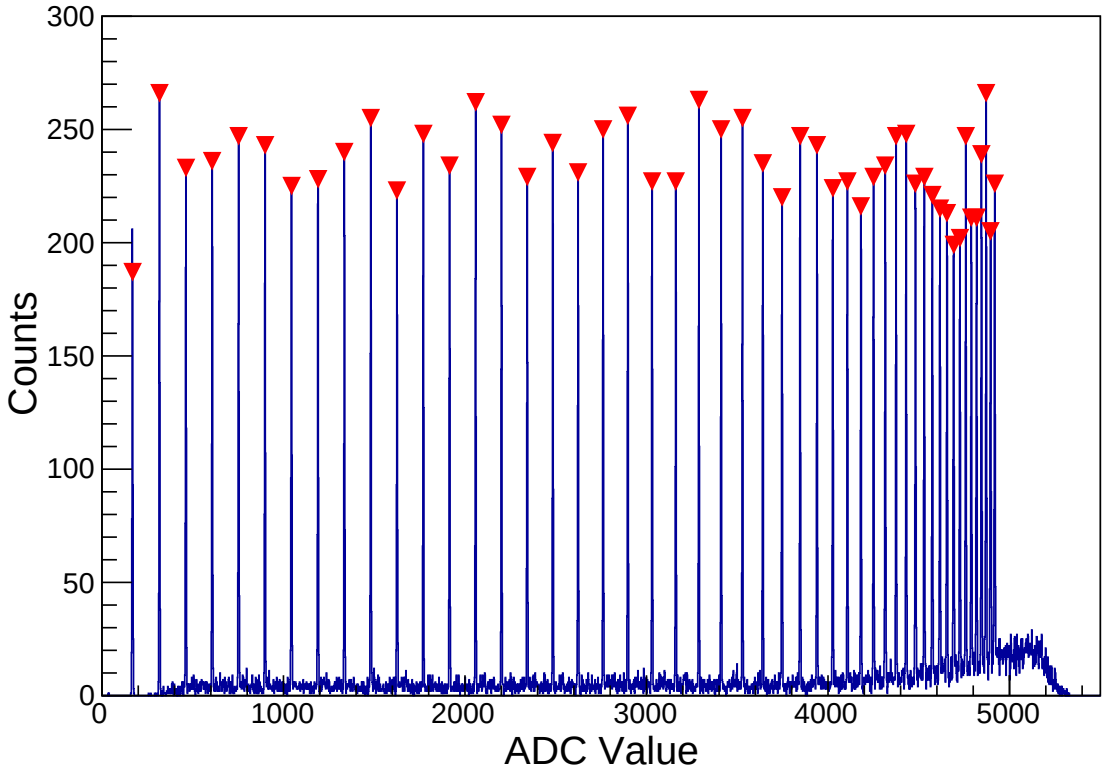

Figure 3.9: Signals from one of the proportional counter cells using evenly-spaced pulser signals. Since the pre-amplifier was in logarithmic mode, the signals can be seen bunching up in the higher ADC channels.

3.4.2 Proportional counter gain matching

While the proportional counter wires were not calibrated for absolute energy, their electronic gains were matched using a pulser. Pulser signals at evenly-spaced intervals were sent to the pre-amplifier, which was set to a logarithmic scale to allow for a larger dynamic range. The centroids for each of the peaks were extracted and fitted with their respective known voltages as shown in Figure 3.9. After the wires have been gain matched, the signals from both sides (left and right) were summed to achieve the specific energy loss of a particle as it traverses through the cell.

3.4.3 Proportional counter position calibration

The proportional counter wires are resistive and read out from both sides. Once the proportional counter wires have been gain matched, the position of the particle passing through the cell was extracted. We used the charge deposited in both sides, Q_L and Q_R for left and right signals respectively, to get the position of the particle in the cell using the formula:

$$x = \frac{Q_R - Q_L}{Q_R + Q_L} a + b, \tag{3.22}$$

where x is the position in a given proportional counter wire, a is the slope and b is the offset introduced to give the real world coordinates inside the scattering chamber. An alpha source was placed in our chamber at a known position in the target gas of helium (96%) + CO_2 (4%) gas admixture, albeit at a lower pressure. A mask with vertical slits was covering the silicon detectors giving us a well-defined position in the silicon detectors. As the alpha particles pass through the proportional counter cells, we extracted a raw position by using Eq. 3.22 without the slope and offset terms. The raw position values along with the known positions of the source and the silicon detector were used to reconstruct the calibrated position of the proportional counter wires. A schematic of the position calibration of the proportional counter wires is shown in Figure 3.10.

3.4.4 Electronics

The electronics scheme for this experiment is shown in Figure 3.11. Signals from the ionization chamber, multi-wire proportional counter detector, and silicon detectors were sent through a pre-amplifier to a MESYTEC MSCF-16 shaper. The shaper amplified and shaped the signal and provided a trigger if needed. The energy signal from the shapers were sent to a MESYTEC analog to digital converters (ADCs) to record the energy. The timing signal was sent to MESYTEC time to digital converters (TDCs) to record the time. Signal from the two PMTs from the upstream scintillator was sent to a CAEN charge-to-digital converter (QDC) to measure the integrated charge of the signals. The signal was also sent

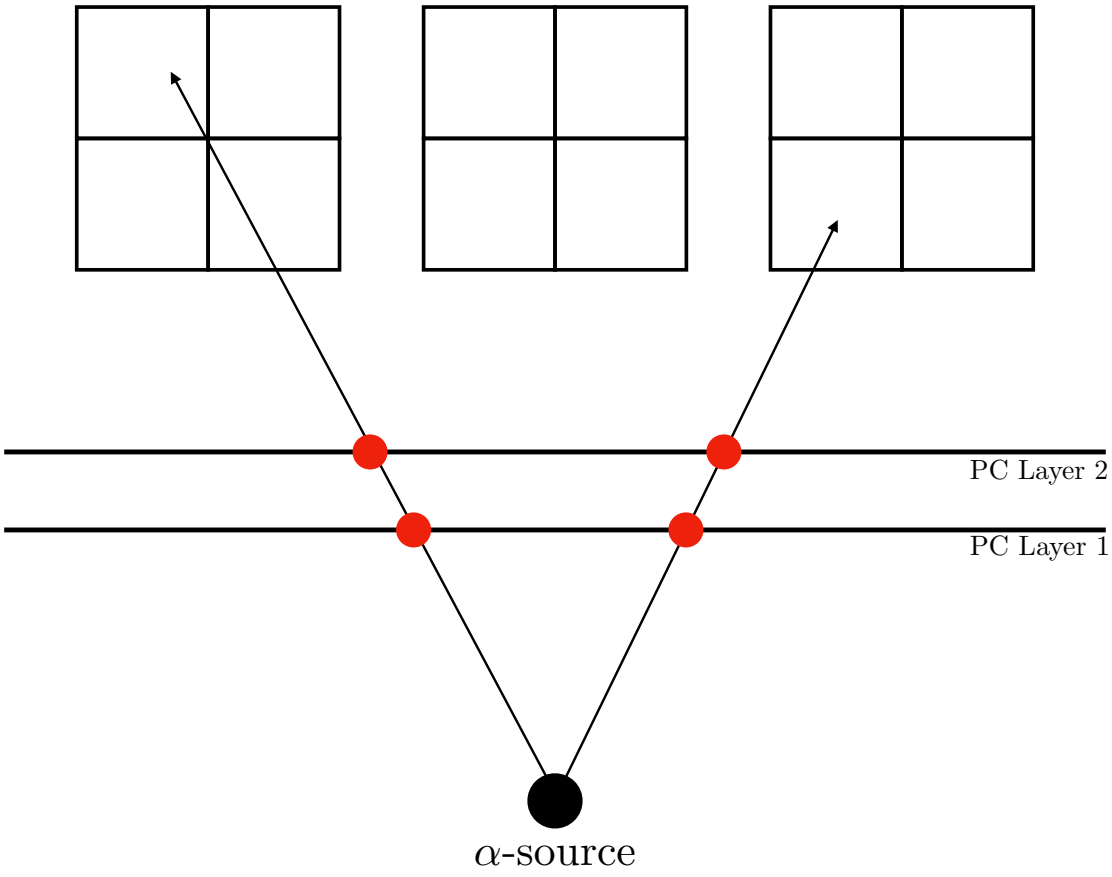

Figure 3.10: This shows a schematic of the position calibration of the proportional counter wires. The α-source was placed at a known distance from the silicon detectors. This distance along with the relative distance of each of the wires was used to calculate the position in each of the wires. This was then used to calibrate the raw position signal in the wires.

to a MESYTEC constant fraction discriminator (CFD) with a pre-determined threshold set. The output from the CFD was then sent to a logic unit when the signals from the PMTs exceeded the pre-determined threshold in coincidence with a signal from a silicon detector. A veto signal from the data acquisition computer was also sent to the logic unit. This prevented the setup from triggering when the data acquisition computer was busy and could not accept a trigger.

The pulse signal that triggered the logic unit was then sent to a gate and delay generator to generate gates for the QDCs, TDCs and ADCs as well as to the data acquisition computer to record the data from all the modules mentioned using the VME-USB module. This data was then processed and analyzed further using the ROOT analysis framework [58].

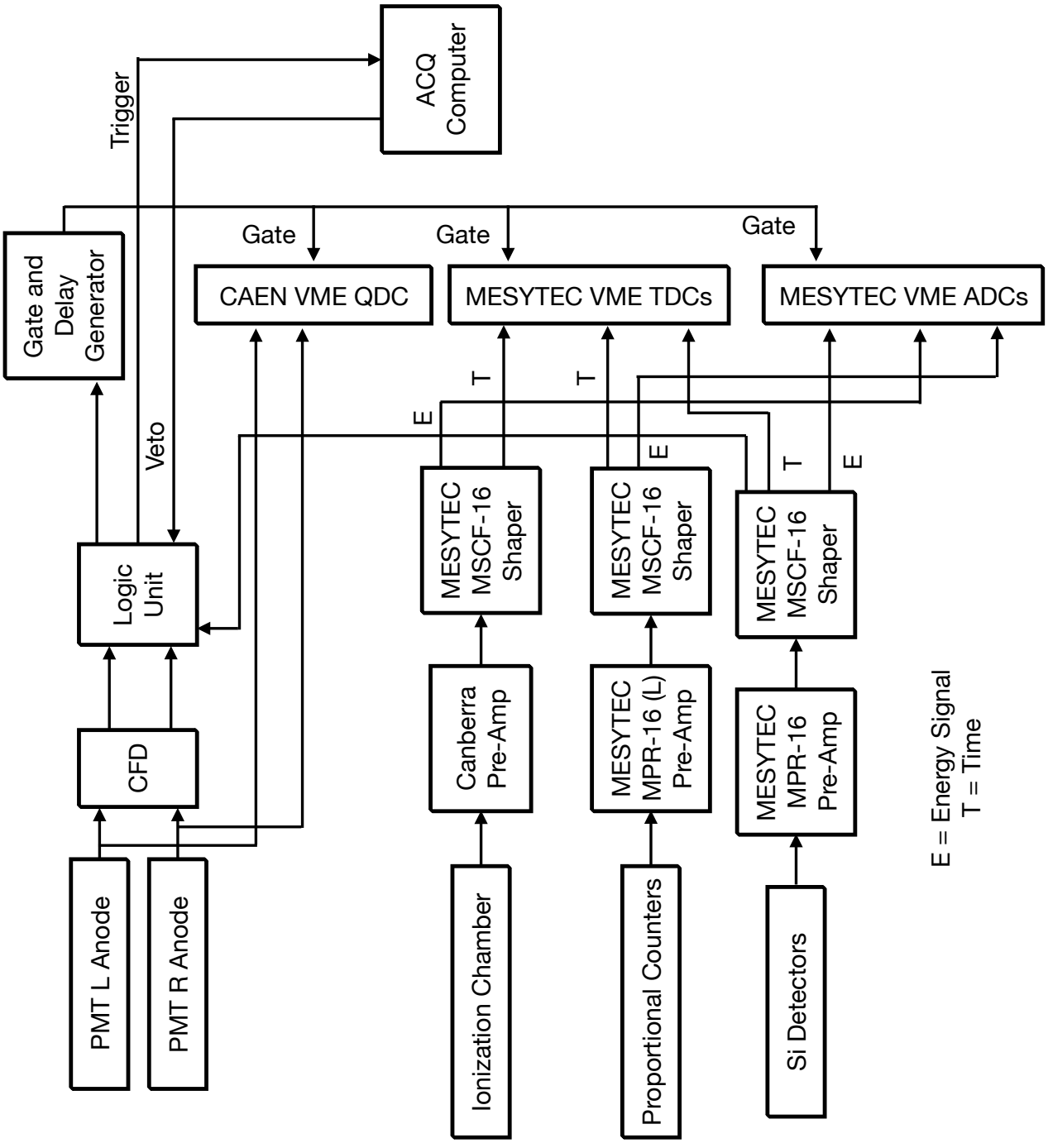

Figure 3.11: Electronics schematic. Reprinted with permission from [59].

The GEANT4 framework [60], along with MINRMATRIX [61] and AZURE2 [62], were used to perform Monte Carlo simulations to better understand our experimental conditions as well as to ascertain the experimental yields of parameters presented in Ref. [44, 47]. In addition to this, the GEANT4 simulations were also used to characterize our background. R-Matrix calculations were performed with MINRMATRIX, yielding cross sections that were then input into the GEANT4 simulations. After the detector and experimental conditions were replicated in the GEANT4 framework, the necessary physics classes were constructed. A generalized reaction process titled `InelasticProcess` was written to handle non-relativistic elastic and inelastic processes. The code to simulate the breakup of ^{6}He as a three body continuum ($^6\text{He} \longrightarrow \alpha + 2n$) was also included to simulate the general shape of the background due to the breakup process. A more detailed treatment of the GEANT4 framework is presented in Section 4.2.

4.1 *R*-Matrix calculations

The two programs that were used to generate cross sections pertaining to this reaction were MINRMATRIX and AZURE2. The bulk of the calculations were performed using MINRMATRIX, while AZURE2 was used to validate the outputs from MINRMATRIX. Details of the MINRMATRIX program are presented comprehensively in Ref. [61]. The relevant resonance parameters that were used in the *R*-Matrix calculations included the energy eigenvalue (resonance energy), spin, parity, angular momentum, boundary condition and the reduced width amplitude for a given channel (γ_λ). Once these values were set, MINRMATRIX was run over a set of angles ($90^\circ - 180^\circ$ for elastic and $0^\circ - 180^\circ$ for inelastic), resulting in an angular distribution as well as the total cross section (angle integrated in the case of elastic). Elastic cross sections were only evaluated between 90° and 180° to avoid the rise in cross sections due to Rutherford scattering at forward angles. The initial parameters for these

calculations were sourced from Ref. [44]. The partial widths, Γ_α and $\Gamma_{\alpha'}$ from Ref. [44], were converted to the reduced width amplitude γ using,

$$\gamma = \sqrt{\frac{\Gamma}{2P_l}}, \tag{4.1}$$

where P_l is the penetrability factor. The other parameter set used was from Ref. [47]. The parameters provided here were the dimensionless reduced width amplitudes θ^2_α and $\theta^2_{\alpha'}$. The respective reduced widths were calculated using,

$$\gamma = \sqrt{\theta^2 \cdot \gamma_w^2} = \theta\gamma_w, \tag{4.2}$$

where,

$$\gamma_w^2 = \frac{\hbar^2}{\mu a^2} \tag{4.3}$$

with μ being the reduced mass and a as the channel radius. A comprehensive discussion of R-Matrix theory is presented in Section 2.2.

4.2 Geant4 simulations

A comprehensive GEANT4 simulation package was created that is able to simulate both elastic and inelastic scattering with their respective cross sections and angular distributions. This allowed for the utilization of the outputs from MINRMATRIX discussed in Section 4.1. The overall structure of this simulations package is shown in Figure 4.1. The goal of this simulation was to simulate the experimental conditions with realistic conditions. The scintillator and the Havar foil at the entrance of the chamber, the beam stopper towards the silicon detectors and the silicon detectors themselves were included in the simulations. The windowless ionization chamber and the multi-wire proportional counter system were not included in the simulation. This is simply because the events are tagged and tracked by the simulation framework, eliminating the need for using these detectors in the simulation.

A visualization of the simulation is shown in Figure 4.2.

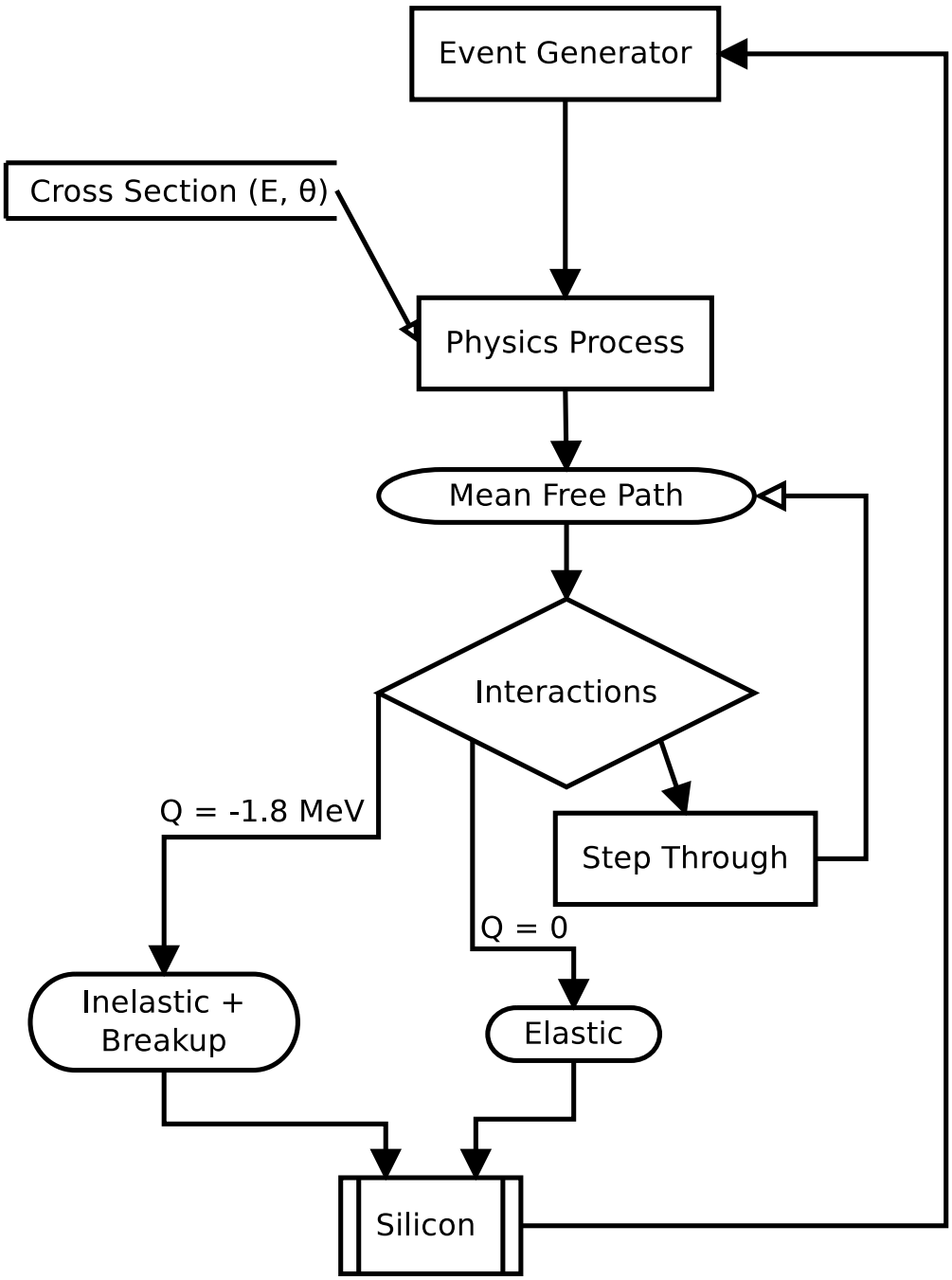

Figure 4.1: Flow chart describing the logic of the GEANT4 simulation used for this analysis.

4.2.1 Event generator

In GEANT4, the primary event, or the beam particle was a ^{6}He ion. It was created to have a certain initial kinetic energy to replicate our beam conditions. The initial beam

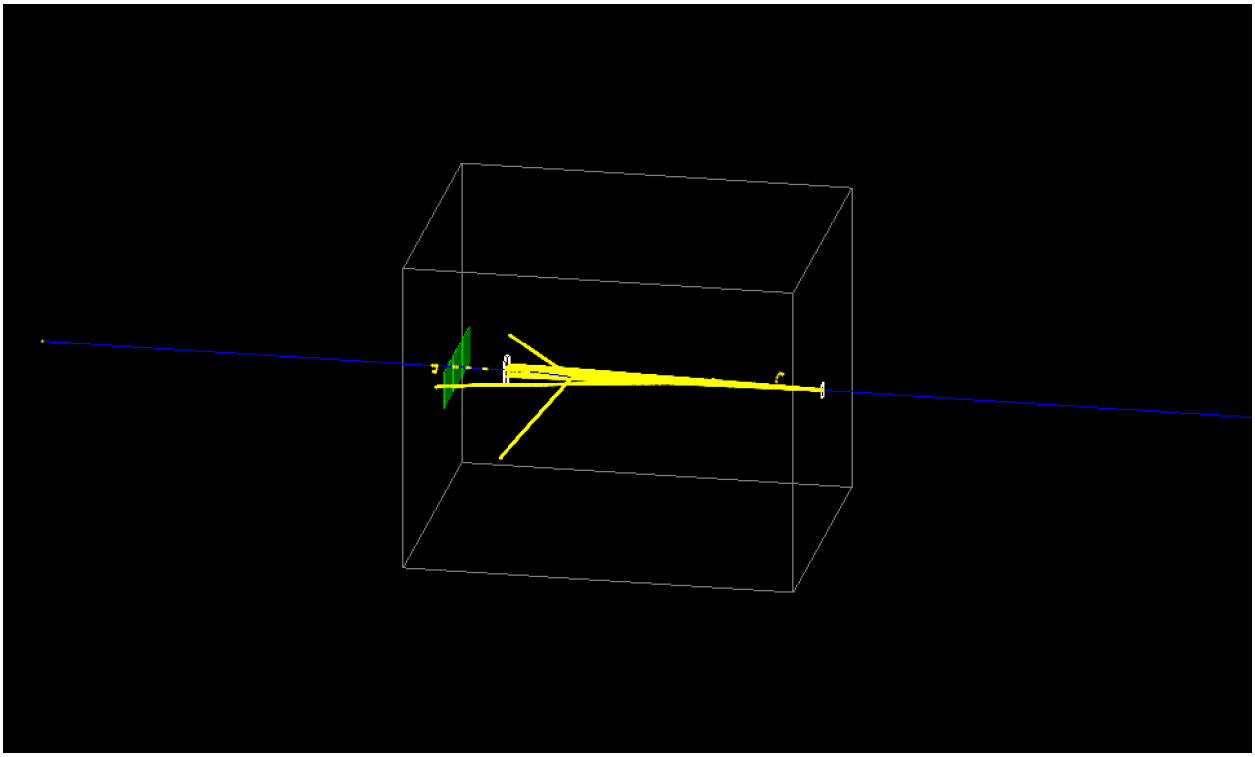

Figure 4.2: A visualization of the GEANT4 simulation. Here, we can see the ^{6}He beam ions interacting with the target gas, as well as being stopped by the beam stopper placed upstream of the silicon detectors. This also shows the three silicon detectors (green squares).

energy and spread are shown in Figure 4.3. The beam contaminant of ^{3}H was not included in the simulation since we effectively selected just the ^{6}He as shown in Figure 3.5 and discussed in Section 3.3.1.

The initial beam energy and the detector set up were verified by ensuring the energy distribution in the silicon detectors was identical for the simulation and the experiment. The simulated beam energy and spread in the silicon detector was nearly identical to our experimental beam characterization, which is shown in Figure 4.4.

4.2.2 Physics processes

The physics process in this simulation encompasses cross section biasing as well as all the reaction processes that will be discussed in further detail below.

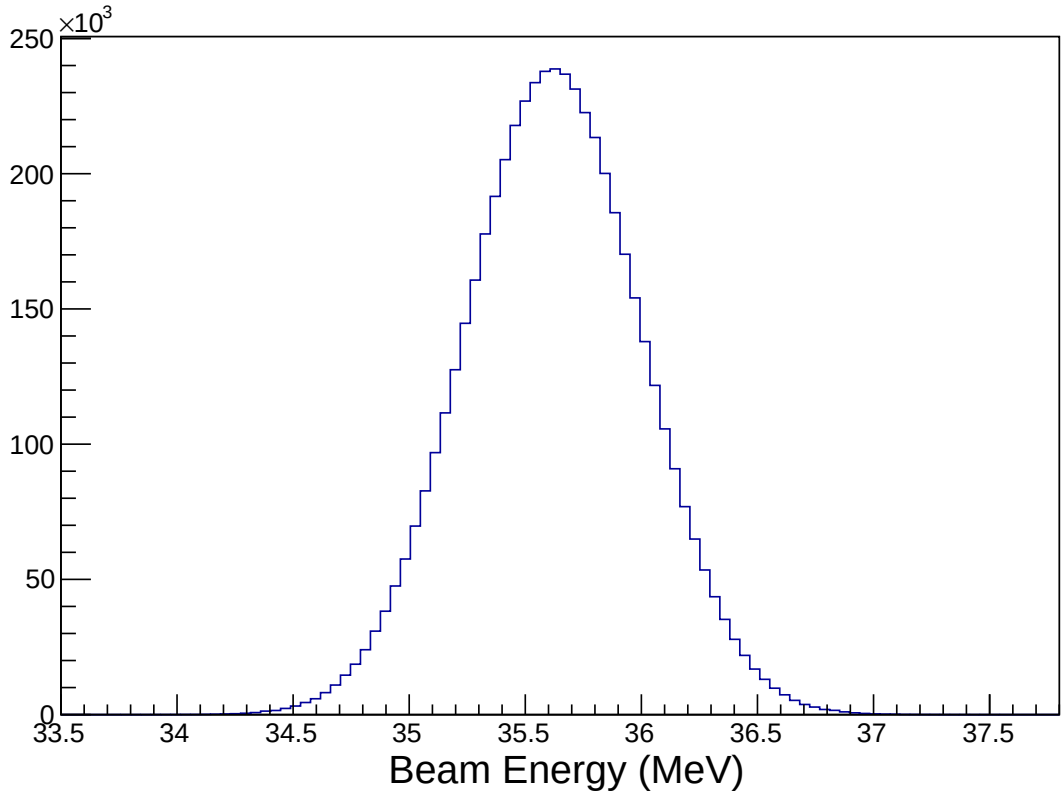

Figure 4.3: Beam energy with a Gaussian profile consistent with the measurements during the experiment was used for the simulations. The full width half maximum (FWHM) for the simulated beam is 0.89 MeV.

4.2.2.1 Cross sections & mean free path

The GEANT4 simulations are biased with cross sections dependent on energy and angle. These are generated using the MINRMATRIX *R*-Matrix software described in Section 4.1. The energy-dependent total cross section provides the energy bias. This, along with simulating 5.3×10^9 ^{6}He ions (which is the total number accumulated during the experiment, determined through the beam integration explained in Chapter 3), gives us the realistic total yield that can be expected with various parameters.

The mean free path (λ) is the average distance a particle traverses between collisions. This is inversely proportional to the density of the gas and the interaction cross section (σ).

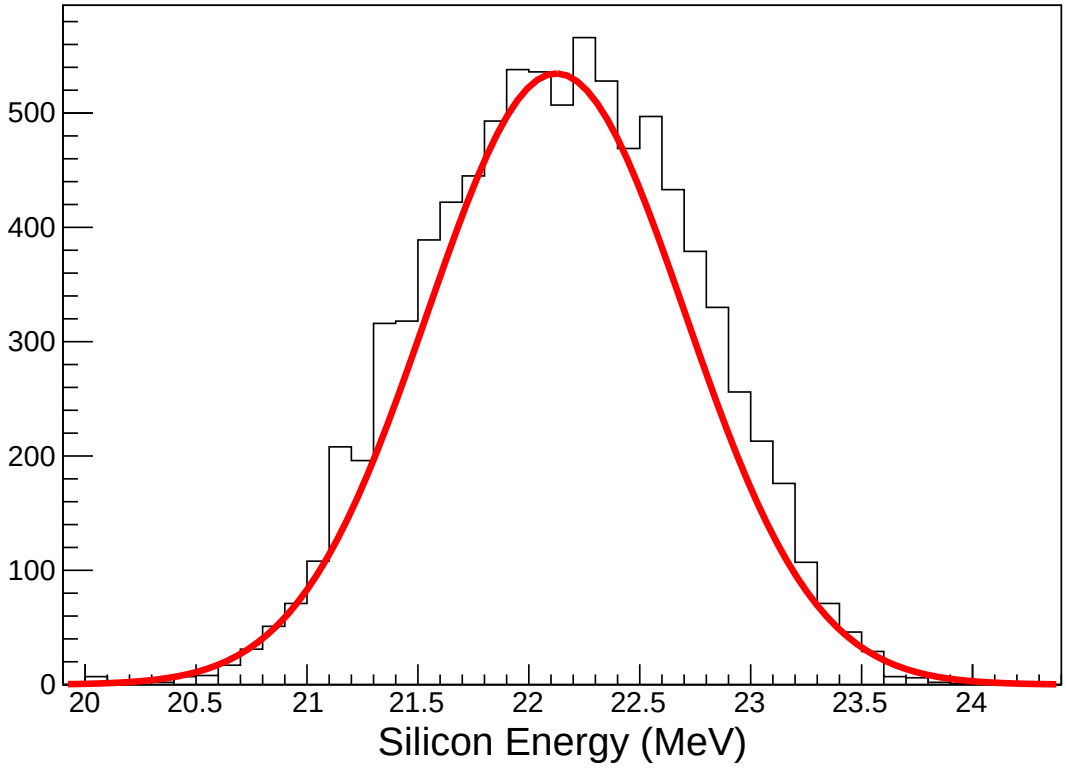

Figure 4.4: The beam energy in the silicon detector while at vacuum as measured during the experiment. This spectrum has a mean of 22.14 MeV and a FWHM of 1.369 MeV. This is comparable to the simulated beam energy in the silicon detector while at vacuum. This energy loss from the simulated beam shown in Figure 4.3 is due to the scintillator and Havar foil near the entrance of the chamber. This produces a mean energy of 22.12 MeV with a FWHM of 1.38 MeV.

A particle that does not interact (zero cross section) has an infinite mean free path. The mean free path (λ) is defined by the following relationship:

$$\lambda \approx \frac{1}{n\sigma}, \tag{4.4}$$

where n is the number density that can be obtained from the ideal gas law as shown in Equation 4.5:

$$n = \frac{N}{V} = \frac{P}{kT}. \tag{4.5}$$

An example of a simulation with a cross section containing a resonance at 6 MeV (center of mass) is shown in Figure 4.5. This figure also highlights center of mass energy range which this setup is sensitive to.

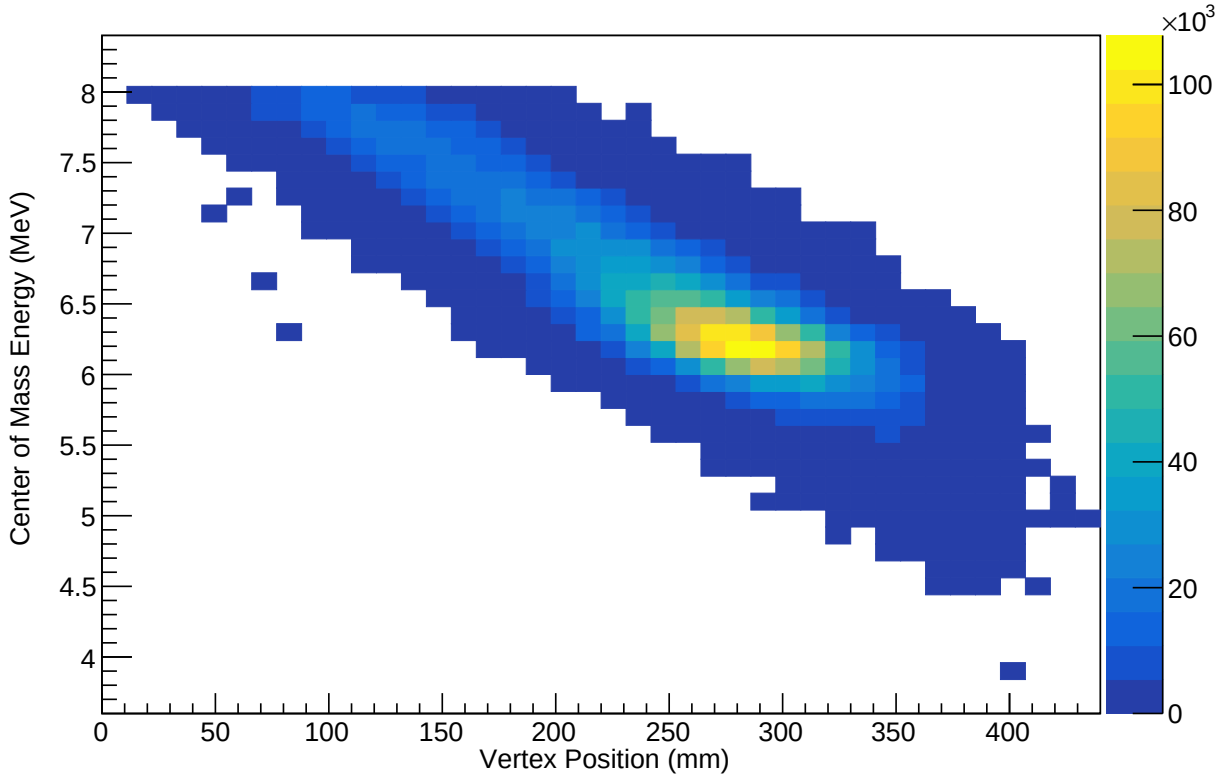

Figure 4.5: Vertex position vs. center of mass energy for a cross section biased simulation. In this figure, a cross section distribution that has a higher cross section at 6 MeV in c.m. was used.

4.2.2.2 Scattering process

Once the mean free path is calculated from the cross section established by the processes discussed in Section 4.2.2.1, the simulation will then step through a finite step size. The probability of an interaction occurring during this step is then calculated and whether this interaction occurs or not is determined according to this probability.

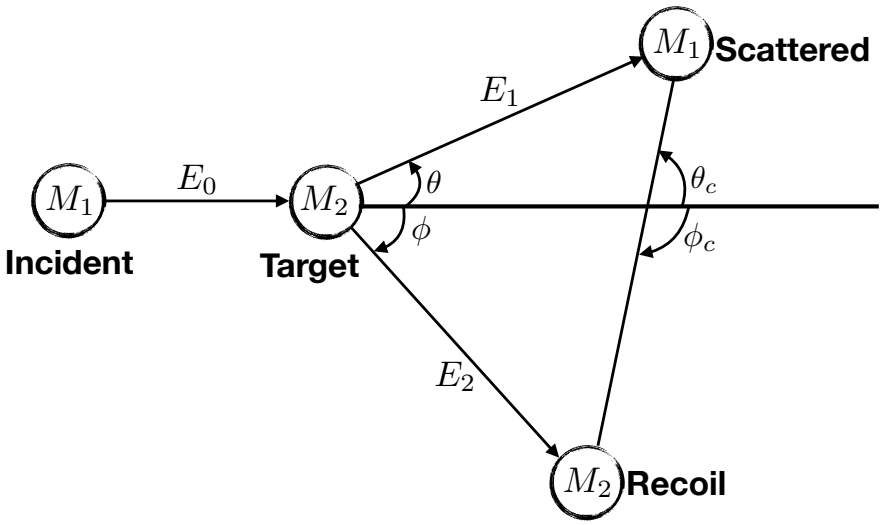

Figure 4.6: Schematic of a scattering event as seen in the lab and center of mass coordinate systems. Scattering angles, energies, and masses are shown for a non-relativistic elastic collision.

Fundamentally, reactions can be classified by their entrance and exit channels, where a channel is a specific nucleus in a specific state. Elastic scattering is defined as a process in which the entrance and exit channels are identical. This means that the Q-value of the reaction is zero. A general schematic of this process is shown in Figure 4.6. Consequently, when $Q = 0$ is given as an input, the reaction process performed by the simulation will be treated as elastic in the GEANT4 framework.

Conversely, for inelastic scattering, shown in Figure 4.7, the entrance and exit channels are not identical, where either one or both of the nuclei from the entrance channel could emerge in the exit channel in an excited state. Inelastic reactions describe reactions where the Q-value does not equal zero and one or both of the nuclei are excited from its ground state.

4.2.2.3 Breakup

To simulate the breakup of ^{6}He as a result of interaction with target nuclei in the gas, a decay process was modelled using the three-body (α-n-n) phase space available in the system. The α-particles energy distribution resulting from the breakup process resembles a

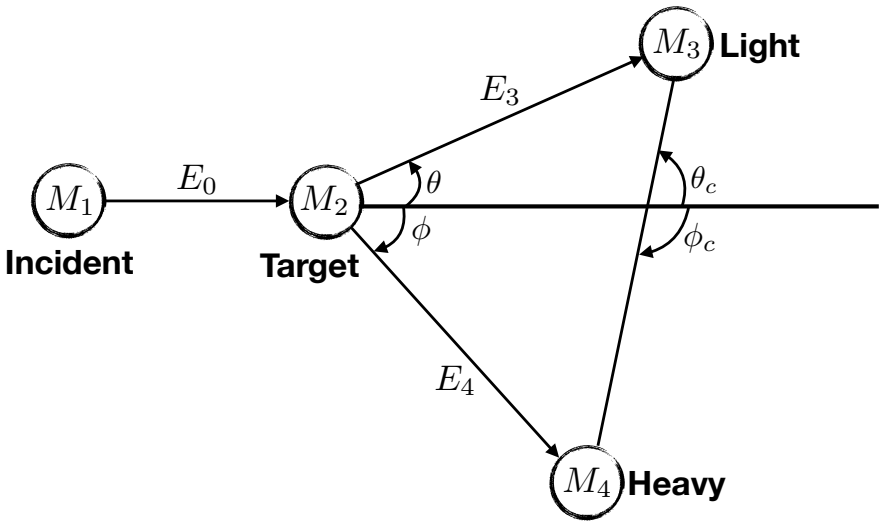

Figure 4.7: Schematic of a scattering event as seen in the lab and center of mass coordinate systems. Scattering angles, energies, and masses are shown a non-relativistic inelastic collision.

Maxwell-Boltzmann distribution as shown in Figure 4.8.

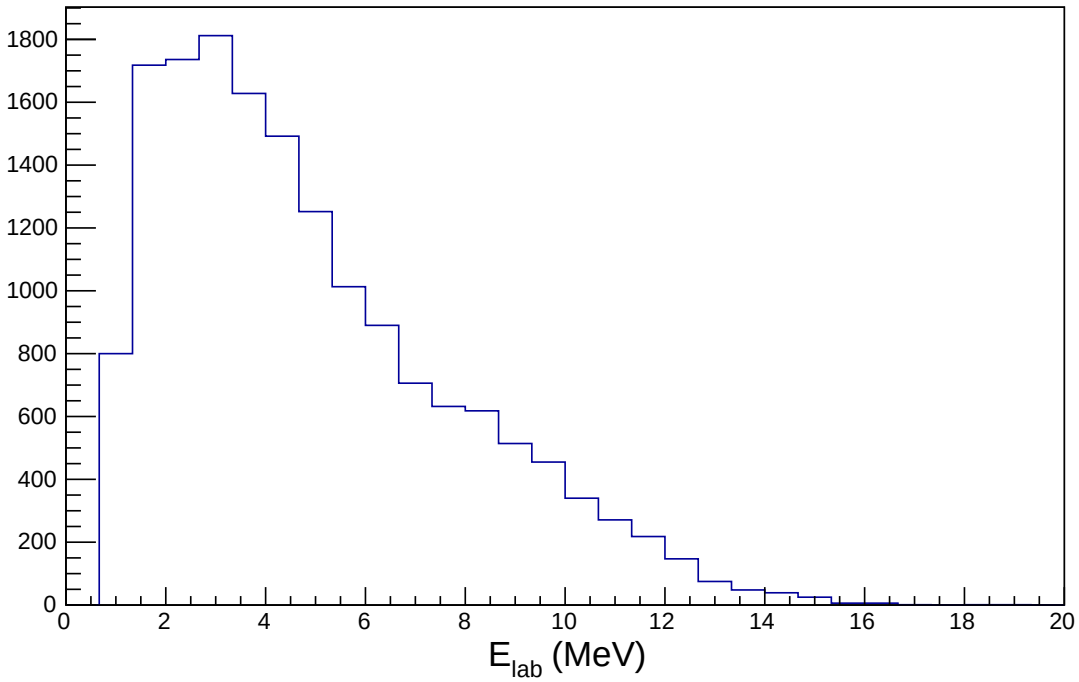

Figure 4.8: Silicon detector energy for region A as a result of the $^6\mathrm{He}^* \longrightarrow \alpha + 2n$ direct breakup at the working gas pressure of the experiment. The distribution shows a phenomenological consistency with a Maxwell-Boltzmann distribution. Inelastically scattered α-particles have a higher energy, with the centroid of the distribution closer to 7 MeV.

5. ANALYSIS *

The analysis of this experiment began with converting the raw data into ROOT data format. The data streams from the VME-USB module were recorded using the Cyclotron Institute's data acquisition software suite, CycApps. This uses a GOOSY data format developed by GSI, which is discussed in detail in Ref. [63]. These files were then converted to the ROOT data format for further analysis. All further analyses were performed using the ROOT data analysis framework [58]. Once the ROOT data files were generated, steps were taken to clean the data and acquire a spectrum of α-particles. Details of this process are described in this chapter.

5.1 Particle identification

The incoming beam had two components to it, ^{6}He and tritium. The tritium contamination was identified in the beam tuning plot in Figure 3.3, as well as the scintillator energy vs. ionization chamber energy plot in Figure 3.5. The "blob" at the lower left corner of the plot is due to the tritium ions in the beam. The part highlighted is due to the ^{6}He ions in the beam. All further analysis is performed after selecting for the ^{6}He ions highlighted in Figure 3.5.

5.2 Extracting the α-particle spectrum

The specific energy loss of ions in a proportional counter cell is given by the Bethe-Bloch formula for stopping power, which is proportional to:

$$-\frac{dE}{dx} \propto \frac{mz^2}{E}\log\left(\frac{4m_eE}{mI}\right), \tag{5.1}$$

*Parts of Sections 5.2, 5.4, 5.5, and 5.6 are reprinted with permission from "Search for the high-spin members of the α:2n:α band in ^{10}Be" by S. Upadhyayula and G. V. Rogachev and J. Bishop and V. Z. Goldberg and J. Hooker and C. Hunt and H. Jayatissa and E. Koshchiy and E. Uberseder and A. Volya and B. T. Roeder and A. Saastamoinen, 2020, *Physical Review C*, 101, 034604, Copyright 2020 by the American Physical Society.

where E is the energy of the particle, z is the charge of the particle, and I is the mean excitation potential [64]. The specific energy loss in the proportional-counter cell was used to distinguish the α-particles of interest vs. ^{6}He beam ions. The specific energy loss in each of the cells can be acquired by summing both sides of the proportional counter cells, given by Eq. 5.2.

$$E_{p.c} = Q_L + Q_R. \tag{5.2}$$

Since the z for an α-particle and ^{6}He is the same, these particles are more difficult to distinguish at higher energies. The multi-wire proportional counter system was divided into two layers. Layer 1 comprised of wires 1-5, and layer 2 included the remaining wires, numbers 6-8. It is possible that some of the particles traversed through more than one proportional counter cell in each of the layers. This would give partial energy losses in two cells of a layer. To address this issue, each event was assigned the wire ID of the wire with the highest specific energy loss. A signal from the neighboring wires belonging to the same layer were then summed. This yielded the total specific energy loss of the particle.

Using the two layers of the proportional counter cells, shown in Figure 5.1, α-particles were selected for. The first layer showed a significant amount of beam ions in addition to α-particles and scattered ^{6}He ions. While these two particles could be separated at lower silicon detector energies, the specific energy loss in the proportional counter cells was less discernible at higher energies in the silicon detectors. We therefore selected for the ^{6}He ions and set an anti-gate for that selection. This process was repeated for each of the quadrants on a wire by wire basis.

The specific energy loss deposited in the proportional counter cells of layer 1 plotted against the energy of a quadrant of the silicon detector is shown in Figure 5.2. The region enclosed by the red line corresponds to ^{6}He particles. The same routine was followed for the proportional counter cells of layer 2, after the anti-gate on the selected region in layer 1. The resulting spectrum is shown in Figure 5.3.

Figure 5.3 shows two distinct bands of particles. The energy loss for the α-particles is

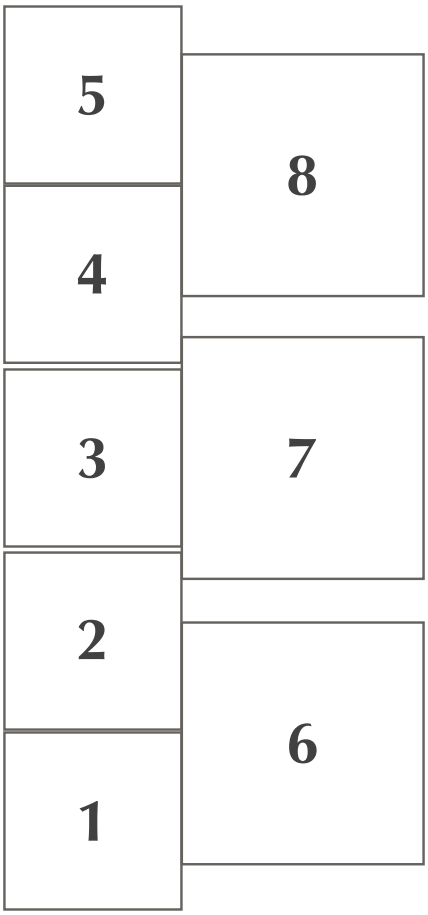

Figure 5.1: Cross-sectional view of the eight multi-wire proportional counter cells. Wires 6-8 make up layer 2, while layer 1 is comprised of wires 1-5. Layer 2 is upstream, while layer 1 is downstream.

lower than that for ^{6}He. Therefore, the band of events enclosed by the red line correspond to α-particles. Using this two layer, anti-gate and gate combination, we were able to extract a clean α-particle spectrum. By gating just above and below the α-band in the second layer, we estimate that no more than 10% of counts in the α-spectrum correspond to the misidentified ^{6}He and virtually all of them are located around the ^{6}He beam energy in the silicon detector between 10 and 12 MeV.

The silicon detector quadrants were split into three different regions for the analysis: the forward angle region, region A, and region B. The forward angle region comprised of the entire center silicon detector. Region A comprised of the inside quadrants of the outside

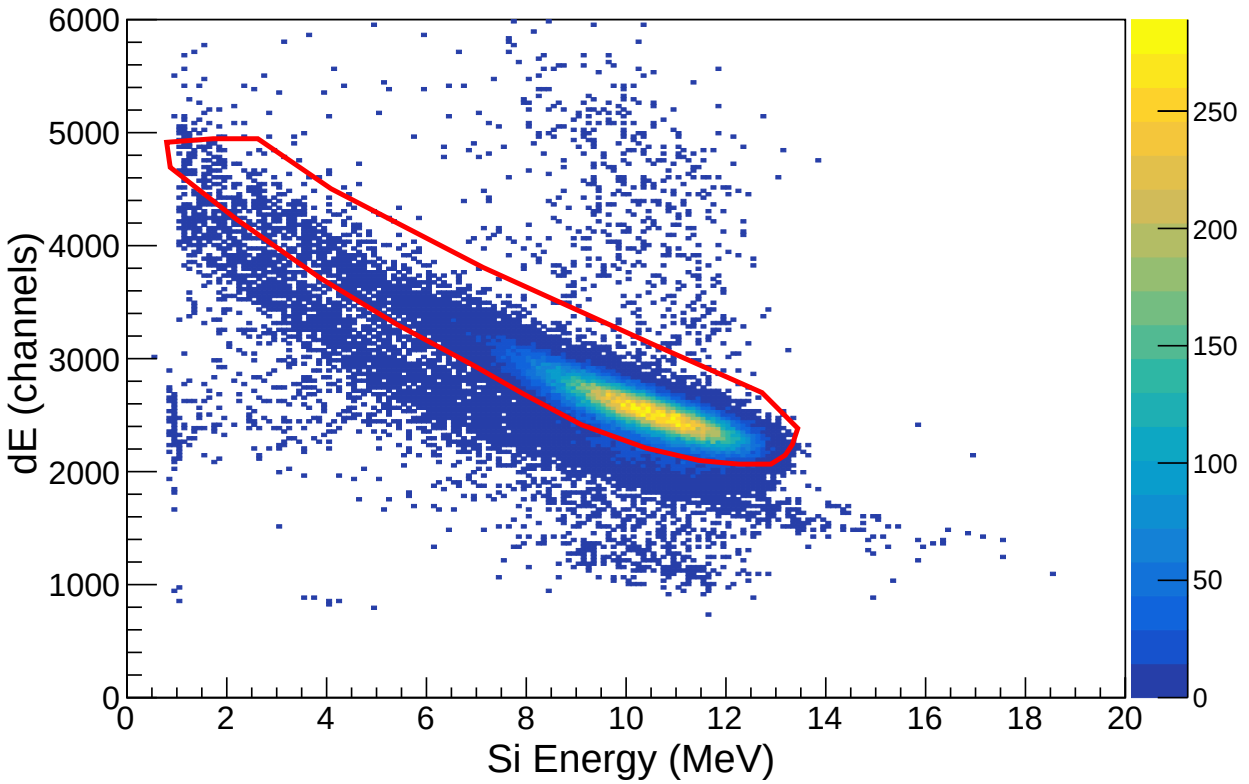

Figure 5.2: Scatter plot of energy losses of the recoil α-particles and ^{6}He ions in the first layer of the proportional counter wires. Events selected here with the red contour are associated with the ^{6}He ions and were anti-gated on to produce a spectrum in the second layer, shown in Figure 5.3.

two silicon detectors. Region B included the remaining quadrants, which are the outside quadrants of the outside two silicon detectors as shown in Figure 5.4.

Due to the beam spread and despite having a beam stopper immediately upstream of the multi wire proportional counter setup, there was still a significant amount of beam which made its way through the proportional counter cells and to the silicon detectors. The forward region was inundated with ^{6}He beam ions. Consequently, we could not achieve a clean separation between the ^{6}He ions and the α-particles in the energy range we are interested in. Thus, we were not able to utilize the data from the forward region in any further analysis. The extent of the beam contamination in our data is shown in Figure 5.5.

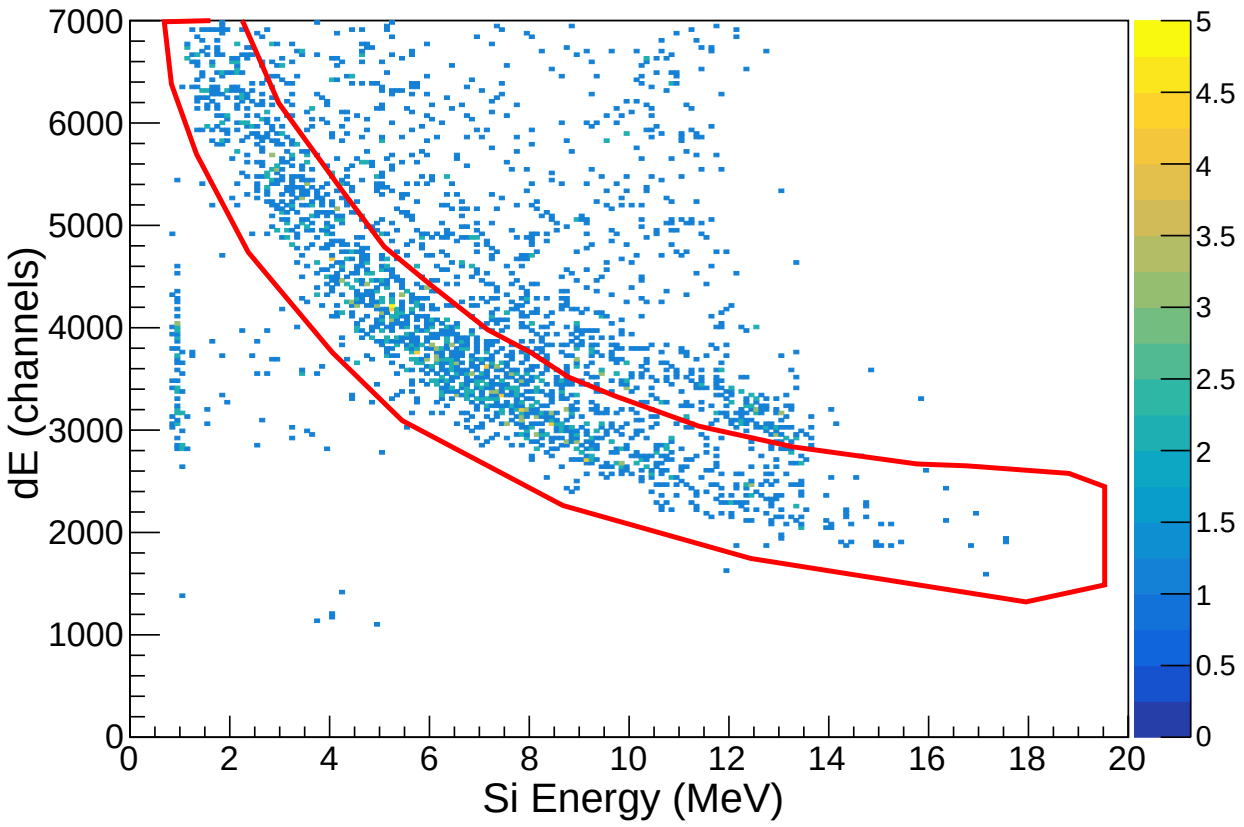

Figure 5.3: Scatter plot of energy losses of the recoil α-particles and the ^{6}He ions that follow from anti-gating on ^{6}He ions in the first layer shown in Figure 5.2. The events selected with the red contour in this layer are the recoil α-particles.

The position calibration of the multi wire proportional counter detector was used to further clean up the data. This was accomplished by plotting possible permutations of the calibrated positions of the two layers of the wires, which yields a linear band, as shown in Figure 5.6. Conditions were then placed on relative wire positions with respect to the two layers to reject outlier events.

The α-particle spectra for the two different regions considered for analysis are shown in Figure 5.7. We assume standard statistical errors here, which scale as $\sqrt{n}$. Region A corresponds to the inside quadrants of the outside two detectors, and region B corresponds to the outside quadrants of the outside detectors. Given the sub-optimum position resolution

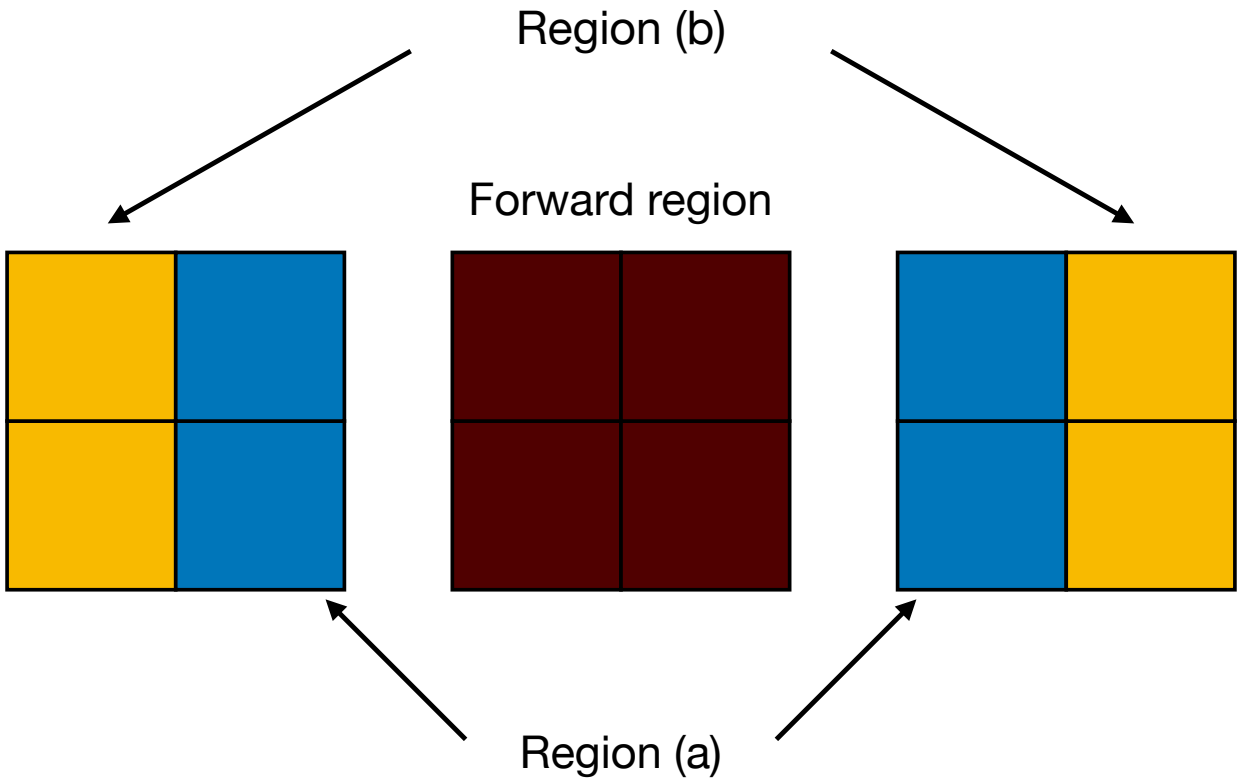

Figure 5.4: Schematic of the three silicon detectors represented as regions for the analysis. The 'forward region' consists of the entire zero degree detector. 'Region A' consists of the inside quadrants of the outside two silicon detectors. 'Region B' consists of the outside quadrants of the outside two silicon detectors.

with our detector set up and the beam spread, it was not possible to reconstruct the scattering vertex on an event by event basis. This made it challenging to ascertain the origins of these α-particles.

However, since the different processes have different kinematic signatures, we made reasonable assumptions to explain the various energy regions of the spectra seen in Figure 5.7. We expect the α-particles between the energies of 8-12 MeV in region A and slightly lower energies of 6-12 MeV in region B to be comprised mostly of elastic scattering. We expect a distribution centering around 5 MeV and 7 MeV in regions A and B respectively to comprise

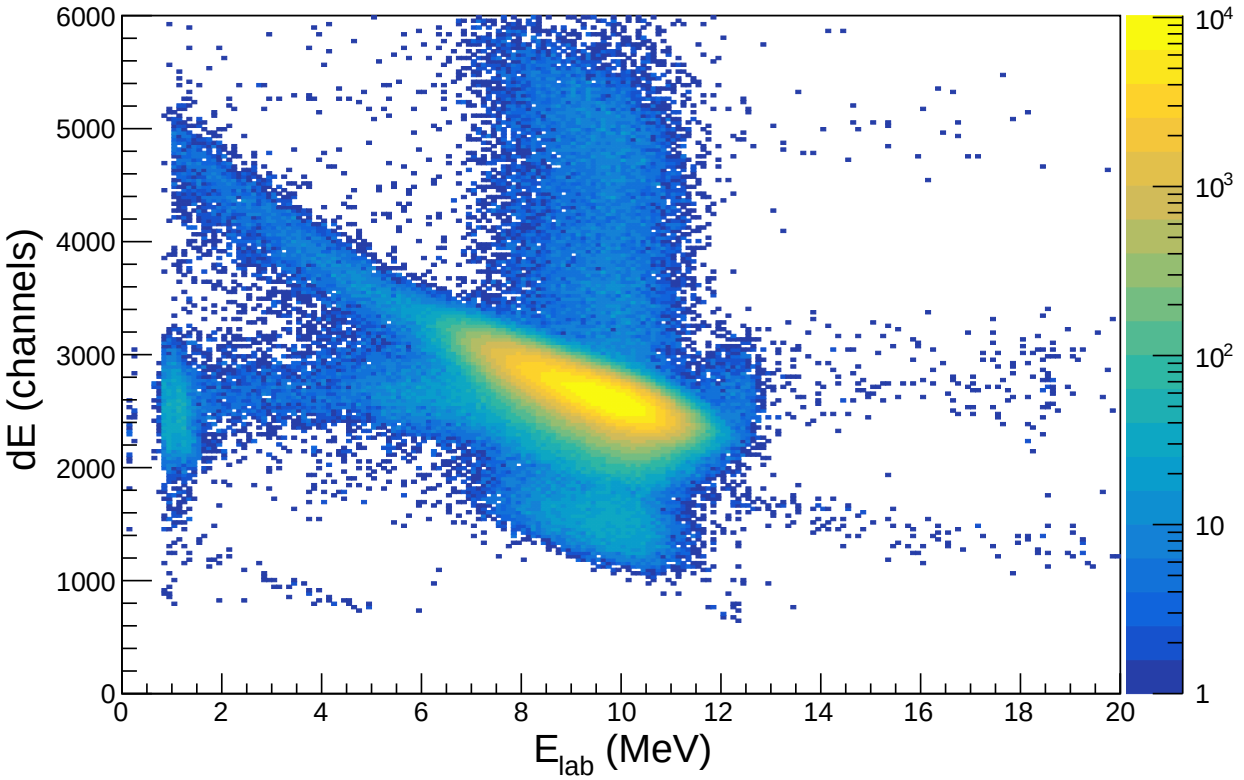

Figure 5.5: dE-E plot from the forward region. The high-intensity region between energies 7 MeV and 12 MeV corresponds to ^{6}He ions from the beam. Since this prevented us from separating the ^{6}He beam ions from the recoil α-particles, particularly in the energy region of interest for us, we had to exclude this region from further analysis.

mostly of ^{6}He(α,α)^{6}He(2^+,1.8 MeV), which is inelastic scattering, where ^{6}He is excited to its first excited state of 2^+. We can also expect some background to contribute to the spectra in Figure 5.7.

5.3 Low pressure data

The origin of α-particles, i.e. the specific reaction that produced them, could not be determined on event-by-event basis in these measurements, except for the highest-energy α-particles which are predominantly produced due to elastic scattering. The obvious feature of the α-spectrum in Figure 5.7 is a strong peak with maximum at 7 MeV in angular region A and at lower energy at larger angles (region B). In principle, this peak may potentially be

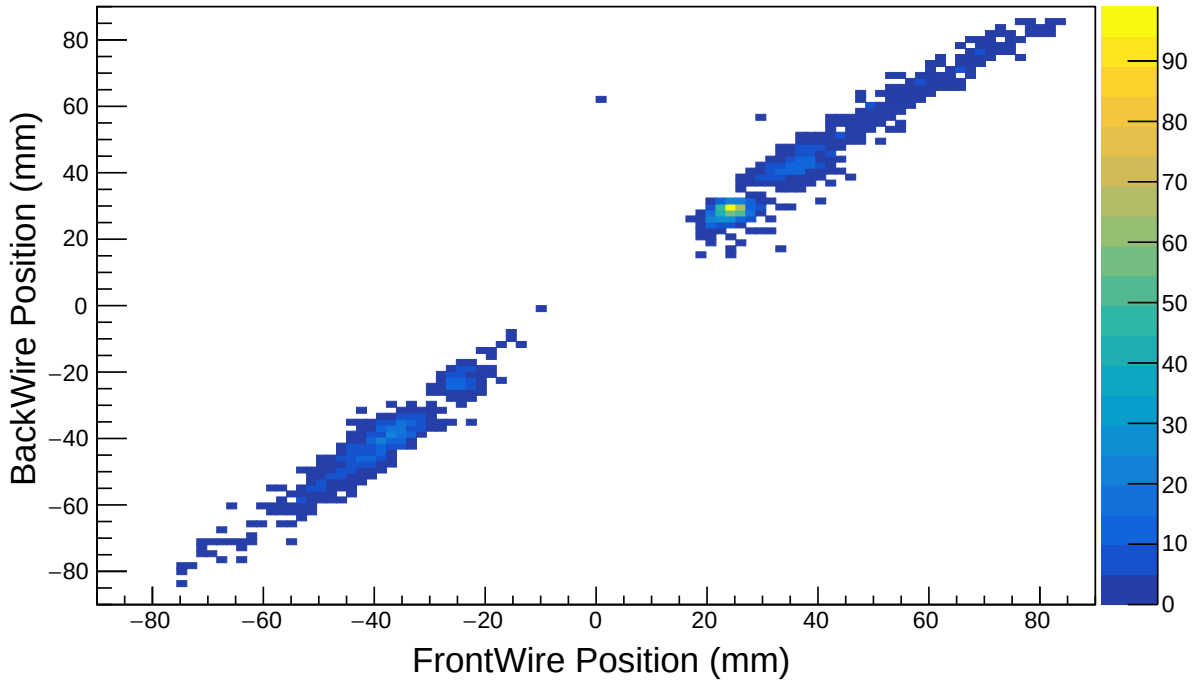

Figure 5.6: Calibrated position of a front layer wire (wire 7) vs. a back layer wire (wire 4). The position in each of the wires depends on the scattering angle. However, given the close proximity of the wires, these are expected to be relatively the same. This plot also shows the forward region covered by the beam stopper, and spaces for the silicon detector frames.

an indication that there is a strong resonance in the excitation function for ^{6}He+α elastic scattering at energy about 6 MeV in c.m. To elucidate the origin of this peak, we performed measurements at lower gas pressure - 1100 Torr. If the peak is due to a resonance then it should not be observed at lower pressure because the energy of the ^{6}He ions never drop below 15 MeV (9 MeV in c.m.) - too high to populate the resonance at 6 MeV in c.m. The spectrum of α-particles from low pressure measurements is shown in Figure 5.8.

A broad feature is observed, therefore evidence of a distinct peak due to a resonance cannot be seen here. The natural explanation for this broad feature is that it is likely due to an energy-independent cross section in the elastic and inelastic channels not populating strong resonances.

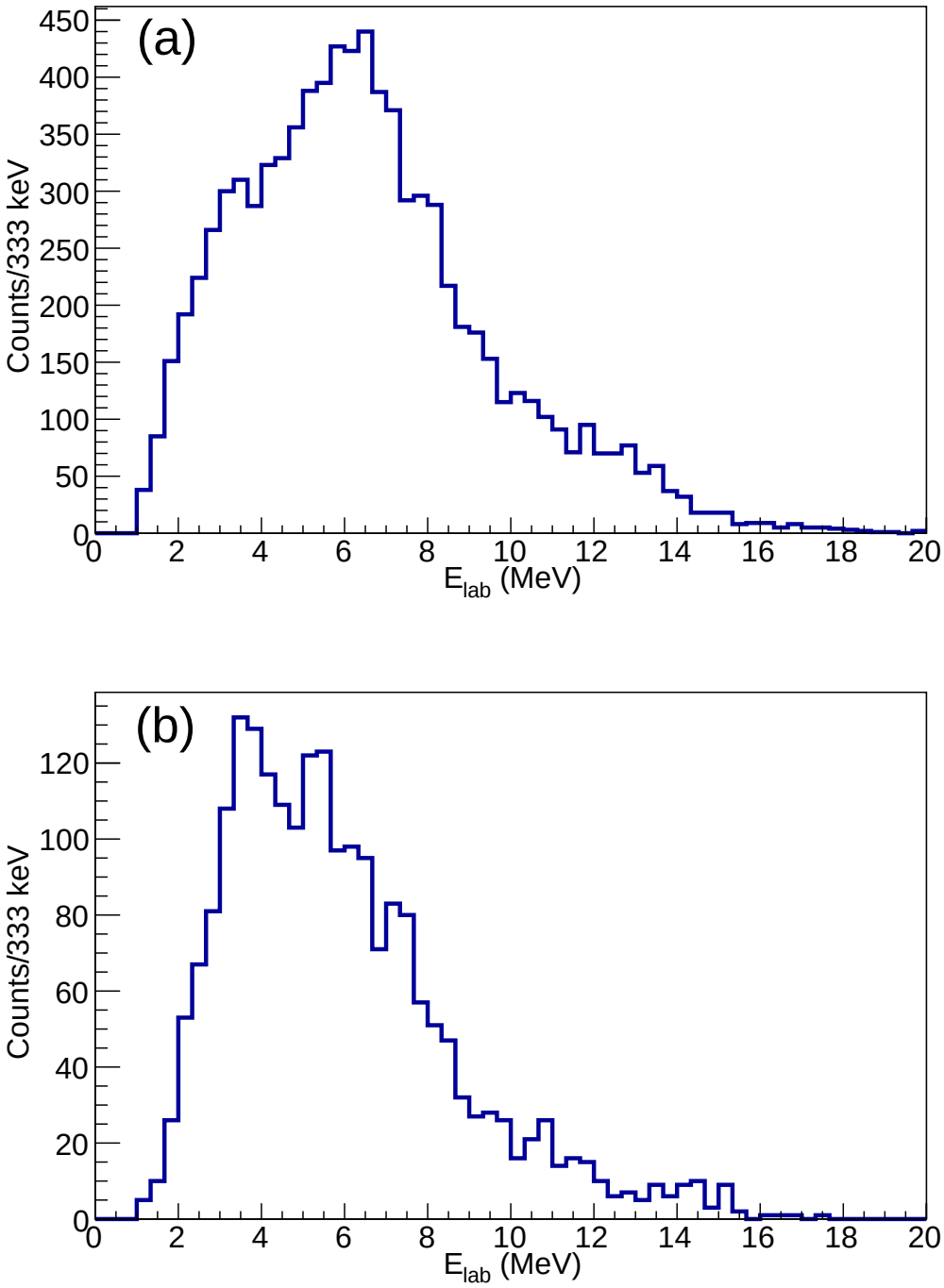

Figure 5.7: Plots (a) and (b) correspond to α-particle spectra for regions A and B of the silicon detectors, respectively. These are particles that have been selected for in layer 2 of the E vs.dE spectra, as described in this section. Region A corresponds to the inside quadrants of the outside two silicon detectors, and region B corresponds to the outside quadrants of the outside silicon detectors.

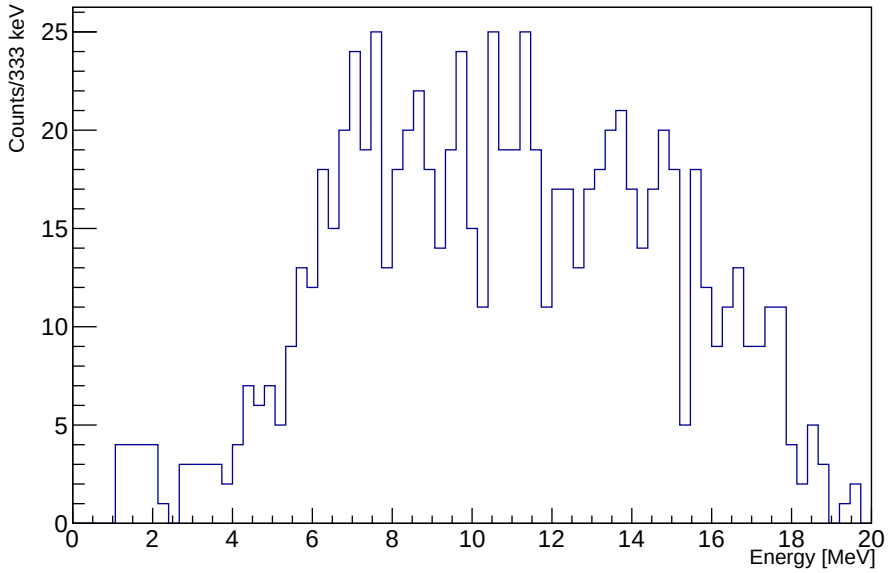

Figure 5.8: Experimental spectrum of α-particles for region A at 1100 Torr. This spectrum shows a broad feature without any discernible resonances. These α-particles have been selected for using the same method of anti-gating and gating on the two layers of proportional counter wires as used for higher pressure data set.

5.4 Hypothesis testing

The spectra of α-particles for two different angular regions are shown in Figure 5.7. The region (a) corresponds to the inside, and the region (b) corresponds to the outside quadrants of the two outside detectors. For an ^{6}He+α c.m. energy of 6 MeV, regions (a) and (b) cover 120°-170° and 100°-150° c.m. scattering angles, respectively.

As discussed earlier, the origin of α-particles, i.e. the specific reaction process that produced them, could not be determined on an event-by-event basis in these measurements. The obvious feature of the α-spectrum in Figure 5.7 is a peak with a maximum at 7 MeV in region (a) and a lower energy in region (b) (smaller c.m. but larger lab. scattering angles). In principle, this peak may potentially be due to a resonance in the excitation function for ^{6}He+α elastic and/or inelastic scattering. To understand our data, we are testing three possible hypotheses: a strong α-cluster 6^+ resonance at 13.5 MeV based on Ref. [44], a

null hypothesis which assumes an energy independent cross section for elastic and inelastic scattering, and a 6^+ resonance at 13.5 MeV that follows parameters obtained in *ab initio* calculations of Ref. [47].

5.4.1 A strong α-cluster 6^+ at 13.5 MeV in ^{10}Be

First, we adopt the parameters for the 6^+ state at 13.5 MeV from Ref. [44] (Table 5.1).

Table 5.1: Resonance parameters for the yrast 6^+ state in ^{10}Be from [44, 20, 21, 47], and this work. θ^2_α and $\theta^2_{\alpha'}$ were calculated using a channel radius of 4.77 fm ($r_0 = 1.4$ fm). The parameters from [44] were determined from a R-Matrix fit.

E_x [MeV]	Γ_{tot} [keV]	Γ_α [keV]	$\Gamma_{\alpha'}$ [keV]	Γ_n [keV]	θ^2_α	$\theta^2_{\alpha'}$	$\Gamma_\alpha / \Gamma_{\alpha'}$	Ref.
13.54	914	99	763	52	0.99	1.25	0.13	[44]
(13.5)	(< 350)	-	-	-	-	-	-	[20]
(13.5)	-	-	-	-	-	-	-	[21]
-	-	-	-	-	0.1	0.66	0.02	[47]
13.5	-	-	-	-	-	-	<0.017	This work

$\Gamma = 2\ \theta^2\ \frac{\hbar^2}{\mu a^2}\ P_l$ and $\theta^2 = \gamma^2/\gamma^2_w$. θ^2 is the dimensionless reduced width. μ is the reduced mass and a is the channel radius, γ is the reduced width amplitude and P_l is the penetrability factor.

These parameters were used with the GEANT4 simulations mentioned in Section 4.2. R-Matrix calculations were performed using codes MINRMATRIX and verified using AZURE2.

The total cross sections for the inelastic scattering and the angle integrated cross section for the ^{6}He + α elastic scattering are shown in Figure 5.9. Both cross sections include just the 6^+ resonance. The cross section for the elastic channel can be described by P^2_6 (sixth order Legendre polynomial squared), where,

$$P_6(\cos(\theta)) = \frac{1}{16}\big(231\cos^6(\theta) - 315\cos^4(\theta) + 105\cos^2(\theta) - 5\big) \tag{5.3}$$

At angles close to 180°, the 6^+ state is expected be manifest as a strong feature (see Figure 5.10). These differential and angle integrated cross sections were then used to generate interactions in the GEANT4-based Monte Carlo simulations. This gave us the total expected

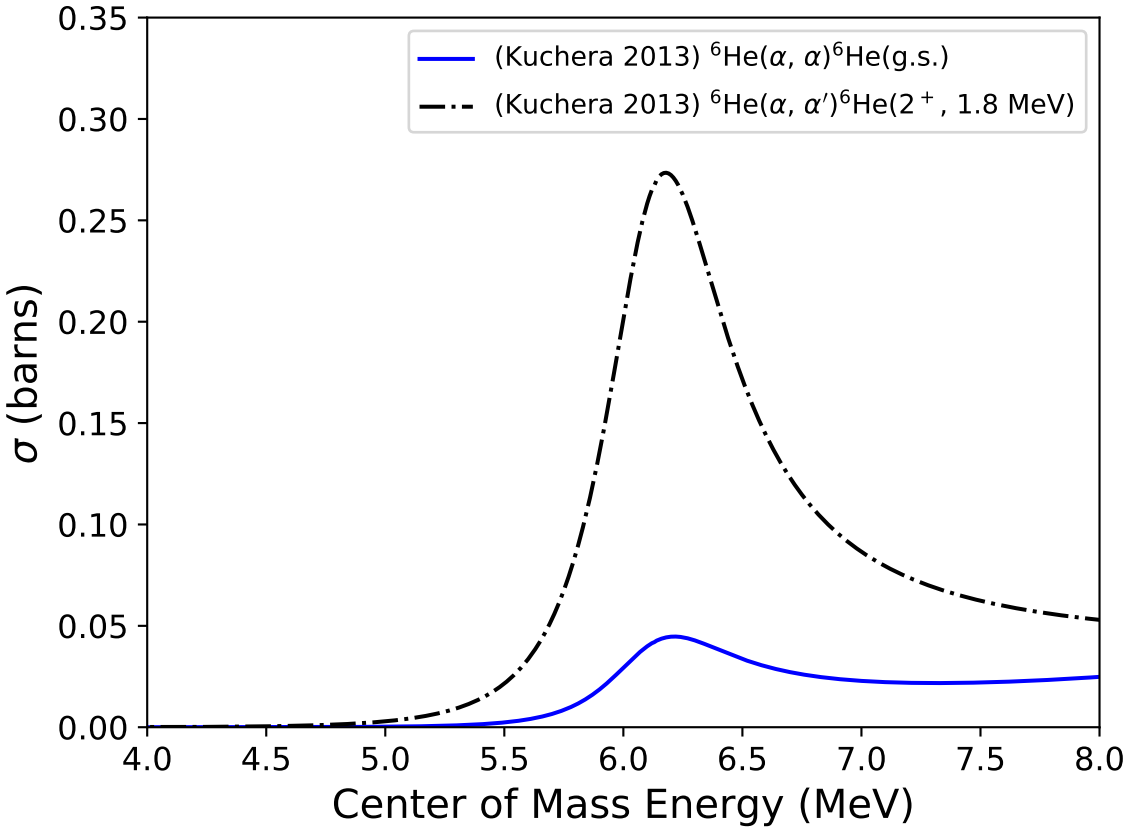

Figure 5.9: Total cross section for inelastic scattering (dash-dotted curve) and 90-180° angle integrated cross section for elastic scattering (solid curve) produced by MinRMatrix calculations using the partial widths the hypothetical 6^+ state only.

yield as well as the α-particle spectrum due to elastic and inelastic channels of the possible 6^+ state. The inelastic scattering simulation included the α-particles resulting from the decay of the first excited state of ^{6}He.

The results from these Geant4 simulations are presented in Figure 5.11. It is evident that the yield produced through the elastic and inelastic processes in the Geant4 simulation far exceeds what we observed in our experiment for both region A and region B. The dimensionless reduced widths for these parameters are $\theta^2_\alpha = 0.99$ and $\theta^2_{\alpha'} = 1.25$. This indicates a strongly clustered state. However, since our experimental yield shown in Figure 5.7 is significantly less than that shown in Figure 5.11, we arrive at two possible conclusions.

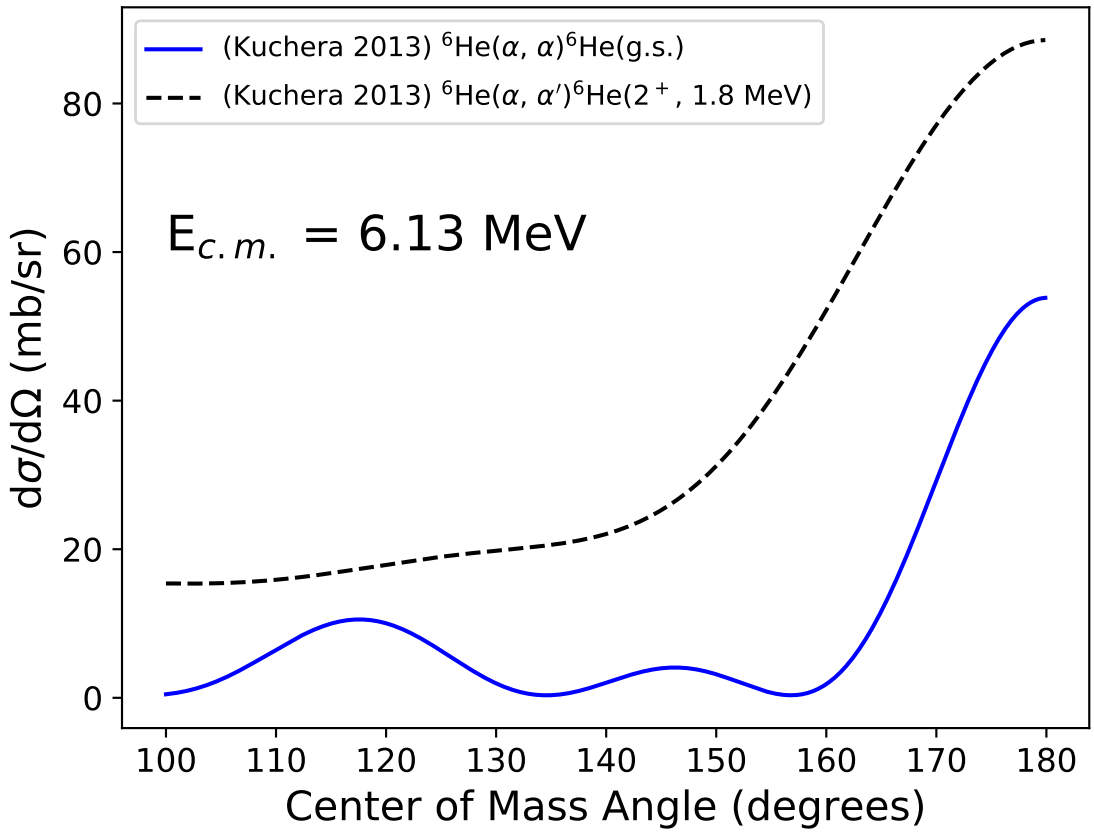

Figure 5.10: Angular distribution for inelastic scattering (dash curve) and elastic scattering (solid curve) produced by MinRMatrix calculations using the partial widths for the hypothetical 6^+ state from Ref. [44]. This plot shows a prominent feature at angles close to $180^{\circ}_{c.m.}$.

We can conclude that either there is no 6^+ state near 13.5 MeV excitation energy in ^{10}Be, or this state's ^{6}He(g.s.) + α partial width is significantly smaller than that mentioned in Ref. [44].

5.5 6^+ state with parameters from microscopic calculations by Kravvaris 2018

Resonating Group Model (RGM) and no-core shell model (NCSM) approach were used by Ref. [47] to calculate the α spectroscopic factors for the states in ^{10}Be. The α spectroscopic factors for the yrast 6^+ state in ^{10}Be are 0.1 and 0.66 for the elastic and inelastic channels respectively. The cross sections were calculated for these parameters using MinRMatrix,

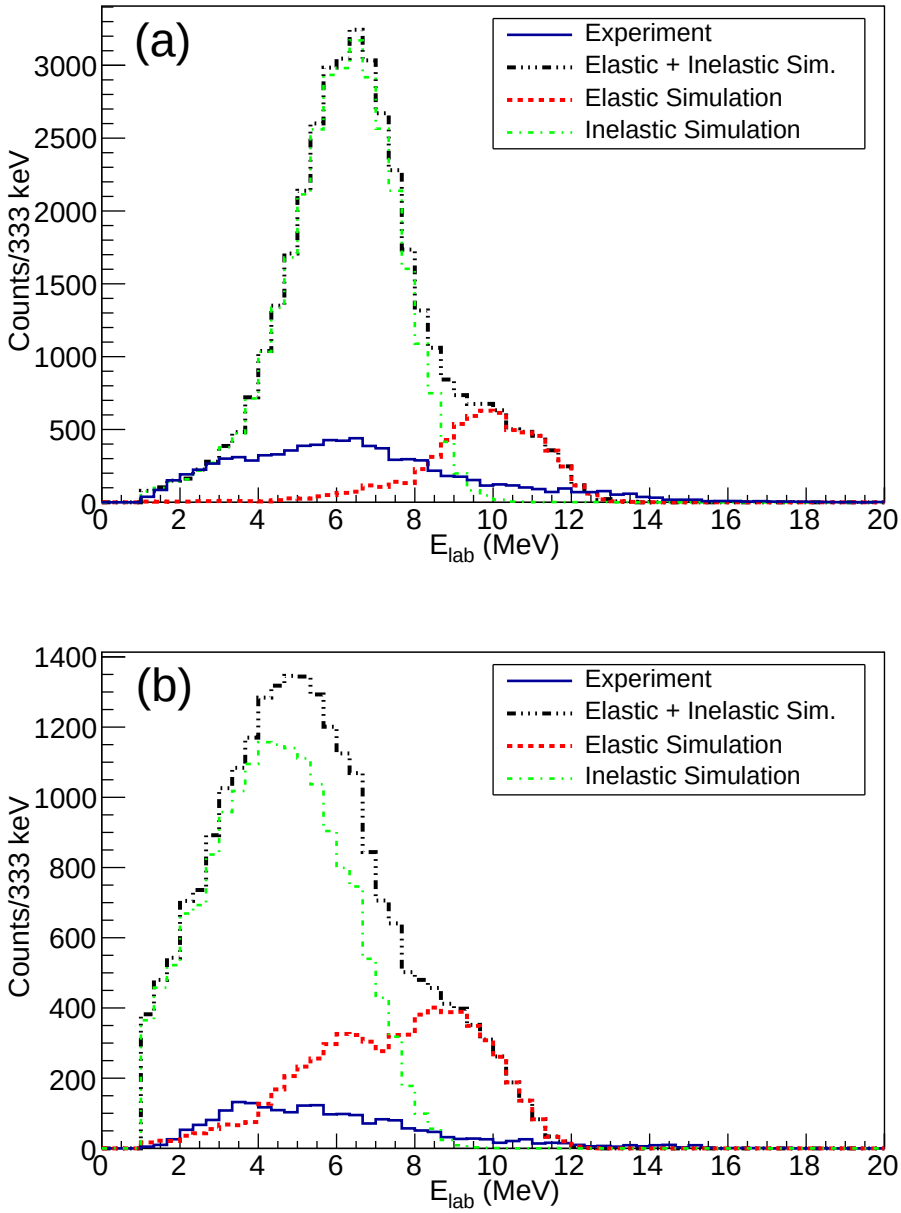

Figure 5.11: GEANT4 Monte Carlo simulations with parameters from Ref. [44] for the elastic (dashed red) and inelastic channels (dashed green), overlaid with this work's experimental spectrum (solid blue) shown in Figure 5.7. The sum of the elastic and inelastic spectrum is represented by the dashed black curve. (a) Experimental, elastic, inelastic, and total spectra for region (a). (b) Experimental, elastic, inelastic and total spectra for region (b).

and subsequently used by GEANT4 to generate realistic spectra that can be compared with our experimental spectrum, in the same way as in Section 5.4.1. Consistent with Section

5.4.1, the angle-integrated cross section for the elastic scattering and total cross section for the inelastic scattering are shown in Figure 5.12. The resulting spectra from the GEANT4 simulations are shown in Figure 5.13 and compared to the experimental data. These cross sections were calculated using the widths of a sole 6^+ resonance.

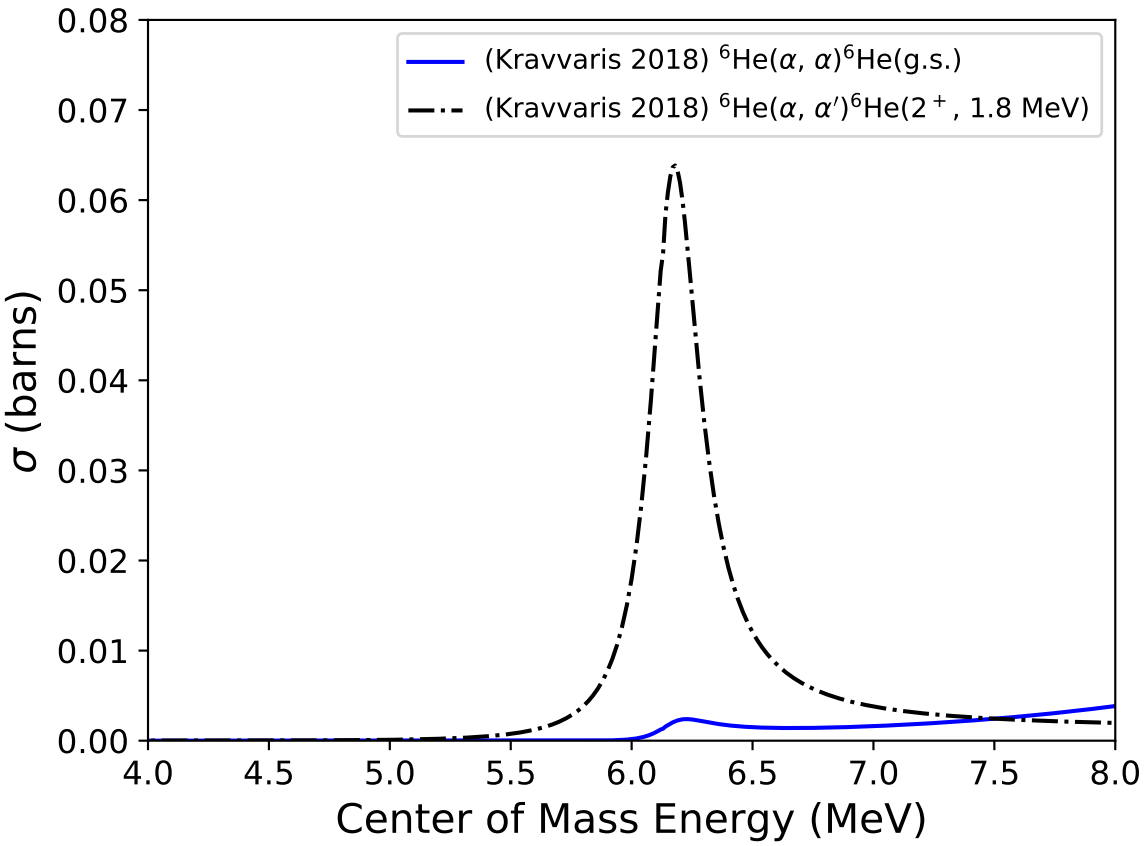

Figure 5.12: MINRMATRIX calculations using the spectroscopic factors provided by [47] to give the total cross sections of the elastic and inelastic channels. In the case of the elastic channel, forward angles were excluded from the calculations to omit the Rutherford contribution. These cross sections were used as input to the GEANT4 simulations, resulting in Figure 5.13.

A 6^+ state with the spectroscopic factors given in Ref. [47] would produce a significantly higher event yield at some energies and the α-spectra that would have a different shape

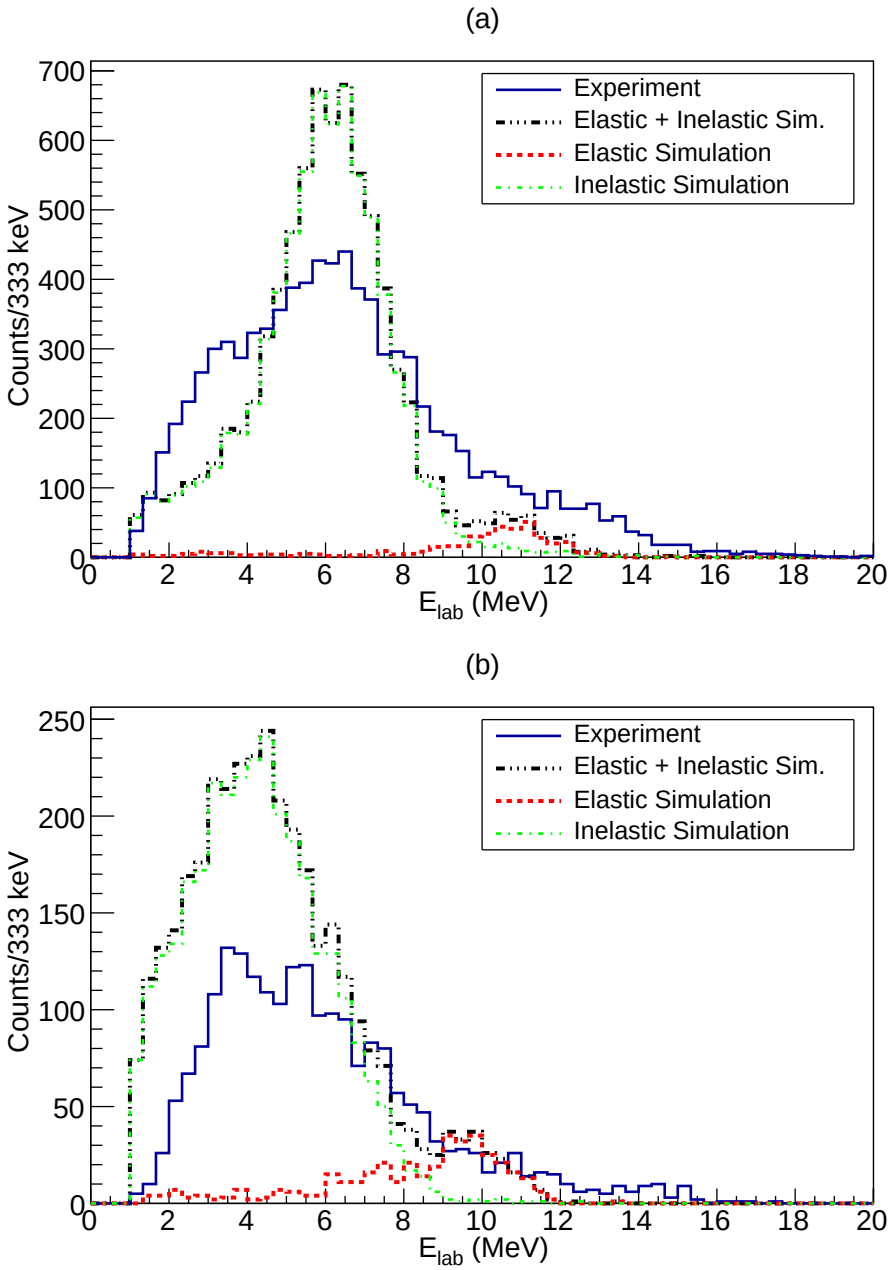

Figure 5.13: GEANT4 Monte Carlo simulations with parameters from Ref. [47], overlaid with this work's experimental spectrum shown in Figure 5.7. While the GEANT4 simulations with parameters provided by Ref. [47] still far exceed the expected yield in this work's experimental spectra as shown here, this setup is still sensitive to the elastic and inelastic channel of the 6^+ state. (a) Experimental (solid blue), elastic (dashed red), inelastic(dashed green), and total spectra (dashed black) for region (a). (b) Experimental (solid blue), elastic (dashed red), inelastic(dashed green) and total spectra (dashed black) for region (b).

than the experimentally observed one and therefore this hypothesis is not consistent with the experimental data either.

5.5.1 Energy-independent cross section

We have thus far compared our data to simulations that assumed existence of the hypothetical 6^+ state with parameters from [44] and [47] and failed to explain the shape and yield of the experimental spectra. Now we assume that the 6^+ state does not exist (or that its ^{6}He(g.s.)+α partial width is negligible) and simulate an energy-independent and isotropic (in the center of mass) elastic and inelastic cross sections. Note that this is generally consistent with the data presented in Ref. [19] for the energy range from 4 to 6 MeV in c.m.

The GEANT4 simulations similar to those described in previous sections were performed, except that now we assumed that the cross section does not depend on energy within the relevant excitation energy region - from 4 to 10 MeV in c.m. An almost perfect fit to the observed experimental spectrum (see Figure 5.14) can be achieved with the following simple assumptions:

- The average differential cross section for the ^{6}He(α,α')^{6}He(2^+,1.8 MeV) reaction is 1.8 mb/sr for the region A and 1.1 mb/sr for region B.
- The average differential cross section for elastic scattering is 0.7 mb/sr for region A and 0.2 mb/sr for region B.
- There is a small background that has a shape of Maxwell-Boltzmann distribution at higher energies that is unrelated to elastic or inelastic channels accounted for in the previous two assumptions.

Note that the assumptions above are generally consistent with the results presented in Ref. [19], in which the ^{6}He+α elastic and inelastic scattering cross sections were measured at energies below 6 MeV in c.m. and in the angular range between 40° and 120° in c.m. Good agreement between the spectrum simulated under the null hypothesis and the experimental

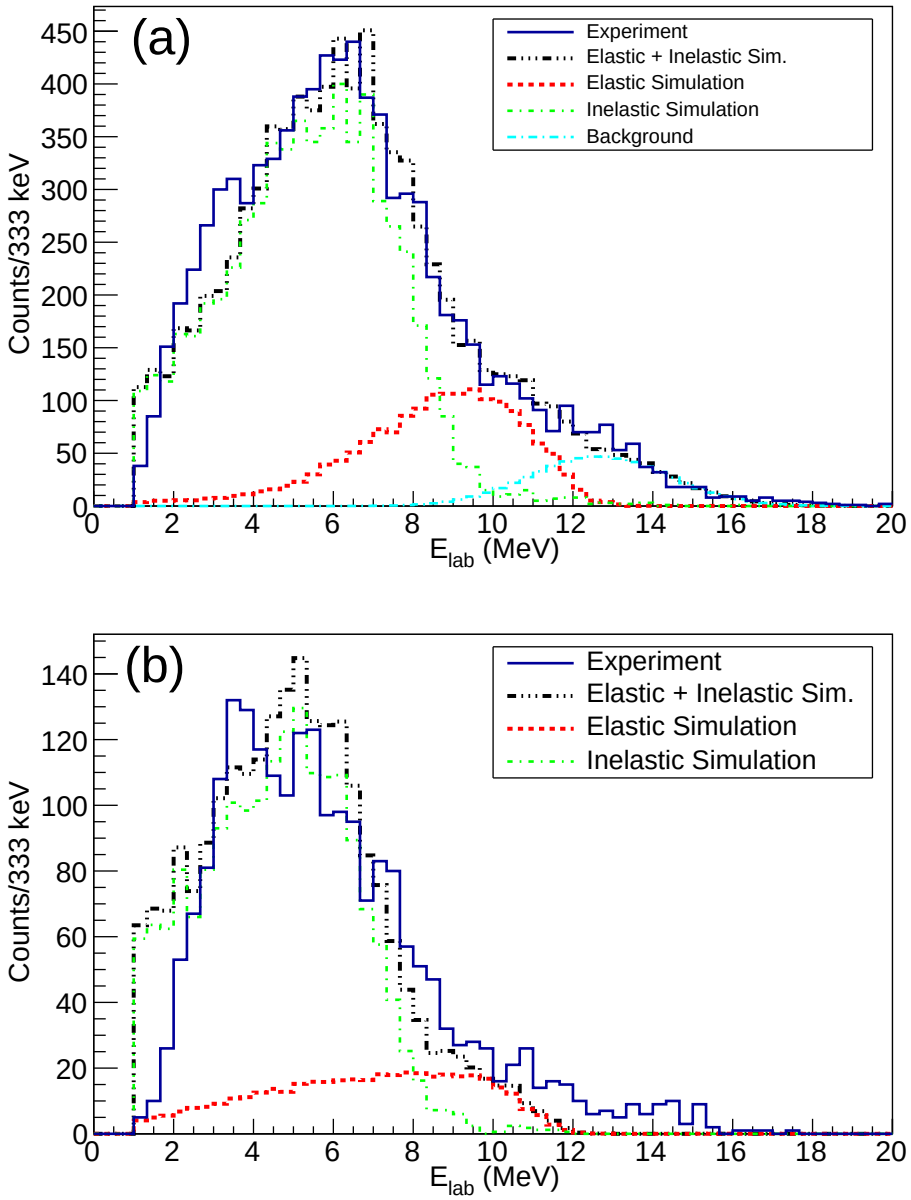

Figure 5.14: GEANT4 Monte Carlo simulations overlaid with this work's experimental spectra. The parameters used for the GEANT4 simulations are consistent with the absence of the 6^+ resonance. (a) Experimental (solid blue), elastic (dashed red), inelastic(dashed green), and total spectra (dashed black) for region (a). (b) Experimental (solid blue), elastic (dashed red), inelastic(dashed green) and total spectra (dashed black) for region (b).

data clearly favors the conclusion that there is no 6^+ state or that its partial α+^{6}He(g.s.) width is very small.

5.6 Establishing an upper limit for the partial width of the hypothetical 6^+ state

The spectroscopic factors from [47] were shown to produce higher yields than those observed in our experimental spectra. Further analysis shows that due to the fact that the cross section for inelastic scattering, which provides the dominant contribution under all of the scenarios considered above, is proportional to the ratio of Γ_α to $\Gamma_{\alpha'}$, we can place an upper limit on this parameter. Figure 5.15 shows a simulated spectrum with $\Gamma_\alpha/\Gamma_{\alpha'} = 0.017$ for the 6^+ state in comparison with the experimental data. It is evident that the event yield already exceeds the experimental one at this ratio and since no background was introduced in these simulations the $\Gamma_\alpha/\Gamma_{\alpha'} = 0.017$ should be considered as a safe upper limit. Note that it is not too far off from the prediction of the microscopic model of Ref. [47], in which the same ratio is 0.02 (see Table 5.1).

A peak at 13.5 MeV excitation energy of ^{10}Be in the ^{6}He(g.s.)+α coincidence spectrum was observed in the breakup of ^{10}Be on a CH_2 target in Ref. [20]. Tentative spin-parity assignment of 6^+ was made for this state in the same work. It is not surprising that the statistics were rather small in that experiment - the branching ratio for the decay that was used to identify this state is below 2%. It appears that conclusive identification of the 6^+ state in ^{10}Be at 13.5 MeV will require another experiment in which the α-decay of this state to the first excited state in ^{6}He is measured. One possible measurement is discussed in Section 6.1.

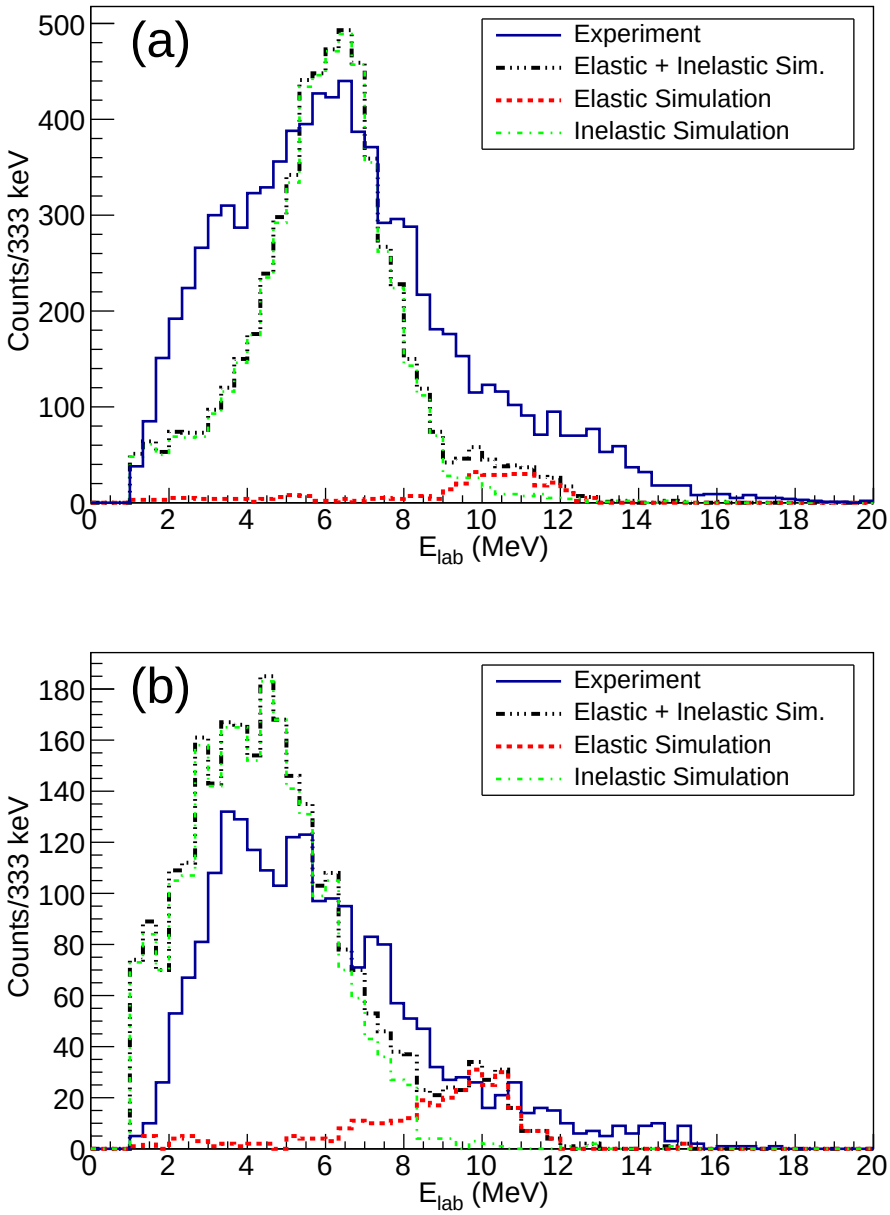

Figure 5.15: GEANT4 Monte Carlo simulations overlaid with this work's experimental spectra. The parameters used for the GEANT4 simulations $\Gamma_\alpha/\Gamma_{\alpha'} = 0.017$. This plot shows the experimental (solid blue), elastic (dashed red), inelastic(dashed green), and total spectra (dashed black) for region (a).

6. CONCLUSION

We showed in Section 2.3.2 that there is strong experimental evidence that some states in ^{10}Be exhibit a molecular-like α:2n:α configuration [18, 17, 19, 44]. Theoretically, these exotic structures can be explored microscopically using the AMD (see Section 2.3.3) plus Hartree-Fock approach [39, 16]. Based on theoretical studies, the 0^+ state at 6.179 MeV in ^{10}Be has a pronounced α:2n:α configuration with an $\alpha - \alpha$ inter-distance of 3.55 fm. This is 1.8 times the corresponding value for the ^{10}Be ground state. The 2^+ state at 7.542 MeV in ^{10}Be is the next member of this highly deformed rotational band [40]. The 4^+ resonance, identified at 10.2 MeV is the next member of this rotational band [18, 17, 44, 19]. The algebraic model detailed in Ref. [45] predicts the 6^+ state to be the next member of the rotational band, and is expected to have an excitation energy of around 13.5 MeV. Identifying this resonance will not only establish this α:2n:α rotational band conclusively, but would also provide a well established case for molecular-like configurations in nuclei and advance our understanding of clustering in atomic nuclei.

In Chapter 3, the measurement performed to search for the 6^+ state at 13.5 MeV in ^{10}Be in the excitation function for ^{6}He + α scattering was detailed. The Cyclotron Institute's K150 cyclotron and the MARS facility were used to produce a secondary beam of ^{6}He at 6 MeV/u from the production reaction of ^{7}Li(d, ^{3}He). The thick-target inverse kinematics approach was used to measure the ^{6}He + α excitation function. Energies between 4.5-8 MeV in the center of mass, along with an angular range of 100° and 170° in the center of mass, were measured.

The α-particle spectrum measured included contributions from elastic and inelastic channels, along with contributions from other processes such as the breakup of ^{6}He$^*(2^+)$ into α+2n. Given the limitations in our setup, the precise origins of the α-particles in this spectrum could not be determined on an event-by-event basis. Consequently, to elucidate the origin of the α-particles, GEANT4 simulations were performed with parameters from

our experimental conditions. In these simulations, the reactions were scaled appropriately using our overall beam normalization from the experiment. These simulations were also scaled with integrated cross sections and angular distributions from R-Matrix calculations performed using MinRMatrix and Azure2. The input parameters for these R-Matrix calculations included parameters from Ref. [44, 47]. The simulation and analysis methods were discussed in detail in Chapters 4 and 5 respectively.

Furthermore, in Section 5.4, we have demonstrated that no evidence for a strong resonance have been observed at the energy of 13.5 MeV in either the elastic or inelastic channels. However, if we assume that the dominant configuration for this state is $^6\mathrm{He}^*(2^+) + \alpha$, and that the coupling to the ^{6}He(g.s.)+α channel is relatively small, as suggested in [47], then the experimentally-observed spectrum can place an upper limit on the ratio between the partial width of the elastic channel to the partial width of the inelastic channels, $\Gamma_\alpha/\Gamma_{\alpha'} < 0.017$. This experimental information provides important constraints on the theoretical models describing the ^{10}Be. We have demonstrated that our data is consistent with the absence of any strong resonances in the cross section (the hypothesis of energy independent cross section) for elastic or inelastic scattering.

6.1 Future work

It is clear, however, that further experiments are needed to elucidate the existence and properties of the 6^+ state at 13.5 MeV in ^{10}Be. It has been demonstrated by [47] that if this resonance were to exist, it would decay strongly in the inelastic channel. Consequently, any proposed measurement would have to take this into consideration. One such measurement could be a breakup reaction with a $^{10}\mathrm{Be}^*$ beam. In this measurement, the $^{10}\mathrm{Be}^*$ would be impinged on a target inducing it to breakup into $^6\mathrm{He}^*(2^+) + \alpha$. The $^6\mathrm{He}^*(2^+)$ would subsequently decay into α + 2n. However, if an active-target detector is used in conjunction with a neutron detector, all four constituents (two α-particles and two neutrons) could be detected in coincidence. This would allow for the Q-value to be determined on an event-by-event basis, thus making it possible to reconstruct an excitation function.

REFERENCES

[1] R. Mould, *A Century of X-Rays and Radioactivity in Medicine: With Emphasis on Photographic Records of the Early Years*, pp. 12–13. Philadelphia, PA: Institute of Physics Publishing, 1993.

[2] J. Thomson, "XXIV. on the structure of the atom: an investigation of the stability and periods of oscillation of a number of corpuscles arranged at equal intervals around the circumference of a circle; with application of the results to the theory of atomic structure," *The London, Edinburgh, and Dublin Philosophical Magazine and Journal of Science*, vol. 7, pp. 237–265, Mar. 1904.

[3] H. Gegier and E. Marsden, "On a diffuse reflection of the apha-particles," *Proceedings of The Royal Society A*, vol. 82, Jul 1909.

[4] J. Chadwick, "Possible existence of a neutron," *Nature*, vol. 129, p. 312, Feb. 1932.

[5] E. Rutherford, "LXXIX. the scattering of α and β particles by matter and the structure of the atom," *The London, Edinburgh, and Dublin Philosophical Magazine and Journal of Science*, vol. 21, pp. 669–688, May 1911.

[6] J. E. Bishop. PhD thesis, University of Birmingham, Birmingham, UK, 2018.

[7] C. F. v. Weizscker, "Zur theorie der kernmassen," *Zeitschrift fr Physik*, vol. 96, pp. 431–458, July 1935.

[8] K. S. Krane, *Introductory Nuclear Physics*. New York, NY: Wiley, 1987.

[9] M. Freer, "The clustered nucleus—cluster structures in stable and unstable nuclei," *Reports on Progress in Physics*, vol. 70, pp. 2149–2210, Nov. 2007.

[10] L. R. Hafstad and E. Teller, "The alpha-particle model of the nucleus," *Physical Review*, vol. 54, pp. 681–692, Nov. 1938.

[11] M. Freer, "Clusters in nuclei," *Scholarpedia*, vol. 5, no. 6, p. 9652, 2010.

[12] S. Okabe, Y. Abe, and H. Tanaka, "Structure of ^{9}Be nucleus by a molecular model. 1.," *Progress of Theoretical Physics*, vol. 57, no. 3, pp. 866–881, 1977.

[13] S. Okabe and Y. Abe, "Structure of ^{9}Be by a molecular-model. 2.," *Progress of Theoretical Physics*, vol. 61, no. 4, pp. 1049–1064, 1979.

[14] M. Seya, M. Kohno, and S. Nagata, "Nuclear-binding mechanism and structure of neutron-rich Be-isotopes and B-isotopes by Molecular-Orbital model," *Progress of Theoretical Physics*, vol. 65, no. 1, pp. 204–223, 1981.

[15] W. von Oertzen, "Dimers based on the alpha+alpha potential and chain states of carbon isotopes," *Zeitschrift für Physik A Hadrons and Nuclei*, vol. 357, no. 4, pp. 355–365, 1997.

[16] Y. Kanada-En'yo, H. Horiuchi, and A. Dote, "Structure of excited states of ^{10}be studied with antisymmetrized molecular dynamics," *Physical Review C*, vol. 60, no. 6, p. 064304, 1999.

[17] M. Freer, E. Casarejos, L. Achouri, C. Angulo, N. I. Ashwood, N. Curtis, P. Demaret, C. Harlin, B. Laurent, M. Milin, N. A. Orr, D. Price, R. Raabe, N. Soić, and V. A. Ziman, "$\alpha : 2n : \alpha$ molecular band in ^{10}Be," *Physical Review Letters*, vol. 96, p. 042501, Jan 2006.

[18] M. Milin, M. Zadro, S. Cherubini, T. Davinson, A. Di Pietro, P. Figuera, . Miljanić, A. Musumarra, A. Ninane, A. Ostrowski, M. Pellegriti, A. Shotter, N. Soić, and C. Spitaleri, "Sequential decay reactions induced by a 18 MeV ^{6}He beam on ^{6}Li and ^{7}Li," *Nuclear Physics A*, vol. 753, pp. 263–287, May 2005.

[19] D. Suzuki, A. Shore, W. Mittig, J. J. Kolata, D. Bazin, M. Ford, T. Ahn, F. D. Becchetti, S. Beceiro Novo, D. Ben Ali, B. Bucher, J. Browne, X. Fang, M. Febbraro, A. Fritsch, E. Galyaev, A. M. Howard, N. Keeley, W. G. Lynch, M. Ojaruega, A. L. Roberts, and X. D. Tang, "Resonant α scattering of ^{6}He: Limits of clustering in ^{10}Be," *Physical Review C - Nuclear Physics*, vol. 87, no. 5, p. 054301, 2013.

[20] D. Dell'Aquila, I. Lombardo, L. Acosta, R. Andolina, L. Auditore, G. Cardella, M. B. Chatterjiee, E. De Filippo, L. Francalanza, B. Gnoffo, G. Lanzalone, A. Pagano, E. V. Pagano, M. Papa, S. Pirrone, G. Politi, F. Porto, L. Quattrocchi, F. Rizzo, E. Rosato, P. Russotto, A. Trifirò, M. Trimarchi, G. Verde, and M. Vigilante, "New experimental investigation of the structure of ^{10}Be and ^{12}C by means of intermediate-energy sequential breakup," *Physical Review C*, vol. 93, no. 2, pp. 1–8, 2016.

[21] W. Jiang, Y. Ye, Z. Li, C. Lin, Q. Li, Y. Ge, J. Lou, D. Jiang, J. Li, Z. Tian, J. Feng, B. Yang, Z. Yang, J. Chen, H. Zang, Q. Liu, P. Li, Z. Chen, Y. Zhang, Y. Liu, X. Sun, J. Ma, H. Jia, X. Xu, L. Yang, N. Ma, and L. Sun, "High-lying excited states in ^{10}Be from the ^{9}Be(^{9}Be,^{10}Be)^{9}Be reaction," *Science China Physics, Mechanics & Astronomy*, vol. 60, p. 062011, jun 2017.

[22] V. F. Weisskopf, "Nuclear physics," *Reviews of Modern Physics*, vol. 29, pp. 174–181, Apr. 1957.

[23] A. M. Lane and R. G. Thomas, "R-matrix theory of nuclear reactions," *Reviews of Modern Physics*, vol. 30, pp. 257–353, Apr 1958.

[24] I. J. Thompson and F. M. Nunes, *Nuclear Reactions for Astrophysics: Principles, Calculation and Applications of Low-Energy Reactions*. Cambridge, UK: Cambridge University Press, 2009.

[25] R. D. Woods and D. S. Saxon, "Diffuse surface optical model for nucleon-nuclei scattering," *Physical Review*, vol. 95, pp. 577–578, July 1954.

[26] C. A. Bertulani, *Nuclear Physics in a Nutshell*. Princeton, NJ: Princeton University Press, 2007.

[27] H. Morinaga, "Interpretation of some of the excited states of $4n$ self-conjugate nuclei," *Physical Review*, vol. 101, pp. 254–258, Jan 1956.

[28] E. M. Burbidge, G. R. Burbidge, W. A. Fowler, and F. Hoyle, "Synthesis of the elements in stars," *Reviews of Modern Physics*, vol. 29, pp. 547–650, Oct 1957.

[29] K. Ikeda, N. Takigawa, and H. Horiuchi, "The systematic structure-change into the molecule-like structures in the self-conjugate $4n$ nuclei," *Progress of Theoretical Physics Supplement*, vol. E68, pp. 464–475, 1968.

[30] Y. Abe, J. Hiura, and H. Tanaka, "A molecular-orbital model of the atomic nuclei," *Progress of Theoretical Physics*, vol. 49, pp. 800–824, Mar. 1973.

[31] Y. Kanada-En'yo, "The Structure of Ground and Excited States of ^{12}C," *Progress of Theoretical Physics*, vol. 117, pp. 655–680, Apr 2007.

[32] Y. Kanada-En'yo, M. Kimura, and A. Ono, "Antisymmetrized molecular dynamics and its applications to cluster phenomena," *Progress of Theoretical and Experimental Physics*, vol. 2012, Aug 2012. 01A202.

[33] J. A. Wheeler, "On the mathematical description of light nuclei by the method of resonating group structure," *Physical Review*, vol. 52, pp. 1107–1122, Dec. 1937.

[34] K. Wildermuth and E. J. Kanellopoulos, "Clustering aspects in nuclei and their microscopic description," *Reports on Progress in Physics*, vol. 42, pp. 1719–1775, oct 1979.

[35] M. Freer, "Molecules in nuclei," *Comptes Rendus Physique*, vol. 4, pp. 475–487, May 2003.

[36] R. Smith, *Experimental measurements of break-up reactions to study alpha clustering in carbon-12 and beryllium-9.* PhD thesis, University of Birmingham, Birmingham, UK, 2017.

[37] M. Ito and K. Ikeda, "Unified studies of chemical bonding structures and resonant scattering in light neutron-excess systems, ^{10,12}Be," *Reports on Progress in Physics*, vol. 77, no. 9, p. 096301, 2014.

[38] M. Ito, "Non-adiabatic dynamics in ^{10}Be with the microscopic alpha + alpha + N + N model," *Physics Letters, Section B: Nuclear, Elementary Particle and High-Energy Physics*, vol. 636, no. 6, pp. 293–298, 2006.

[39] A. Doté, H. Horiuchi, and Y. Kanada-En'yo, "Antisymmetrized molecular dynamics plus Hartree-Fock model and its application to Be isotopes," *Physical Review C*, vol. 56, pp. 1844–1854, Oct 1997.

[40] H. Nishioka, "Two-alpha-particle-plus-dinucleon-cluster model for ^{10}B and ^{10}Be," *Journal of Physics G: Nuclear Physics*, vol. 10, pp. 1713–1729, Dec. 1984.

[41] S. Hamada, M. Yasue, S. Kubono, M. H. Tanaka, and R. J. Peterson, "Cluster structures in ^{10}Be from the ^{7}Li(α,p)^{10}Be reaction," *Phys. Rev. C*, vol. 49, pp. 3192–3199, Jun 1994.

[42] N. Soić, S. Blagus, M. Bogovac, S. Fazinić, M. Lattuada, M. Milin, D. Miljanić, D. Rendić, C. Spitaleri, T. Tadić, and M. Zadro, "^{6}He + α clustering in ^{10}Be," *Europhysics Letters (EPL)*, vol. 34, pp. 7–12, apr 1996.

[43] N. Curtis, D. D. Caussyn, N. R. Fletcher, F. Maréchal, N. Fay, and D. Robson, "Decay angular correlations and spectroscopy for ^{10}Be* $\rightarrow^{4}$ He $+^{6}$ He," *Physical Review C*, vol. 64, p. 044604, Sep 2001.

[44] A. N. Kuchera, *Clustering Phenomena in the A = 10 T = 1 Isobaric Multiplet*. PhD thesis, Florida State University, Tallahassee, FL, 2013.

[45] R. Wolsky, I. A. Gnilozub, S. D. Kurgalin, and Y. M. Tchuvil'sky, "α-cluster and α-binucleon states of 1p-shell nuclei," *Physics of Atomic Nuclei*, vol. 73, pp. 1405–1415, Aug 2010.

[46] G. V. Rogachev, M. L. Avila, A. N. Kuchera, L. T. Baby, J. Belarge, J. Blackmon, V. Z. Goldberg, E. D. Johnson, K. W. Kemper, E. Koshchiy, L. Linhardt, K. Macon, D. Santiago-Gonzalez, and I. Wiedenhöver, "Clustering in non-self-conjugate nuclei ^{10}Be and ^{18}O," *Journal of Physics: Conference Series*, vol. 569, no. 1, p. 012004, 2014.

[47] K. Kravvaris and A. Volya, "Study of clustering in isotopes of beryllium," *AIP Conference Proceedings*, vol. 2038, no. 1, p. 020026, 2018.

[48] R. Tribble, R. Burch, and C. Gagliardi, "MARS: A momentum achromat recoil spectrometer," *Nuclear Instruments and Methods in Physics Research Section A: Accelera-*

tors, Spectrometers, Detectors and Associated Equipment, vol. 285, pp. 441–446, Dec. 1989.

[49] D. Melconian. Private communication, 2020.

[50] B. Roeder. Private communication, 2020.

[51] K. P. Artemov, O. P. Belyanin, A. L. Vetoshkin, R. Wolskj, M. S. Golovkov, V. Z. Goldberg, M. Madeja, V. V. Pankratov, I. N. Serikov, V. A. Timofeev, V. N. Shadrin, and J. Szmider *Soviet Journal of Nuclear Physics*, vol. 52, p. 408, 1990.

[52] S. Upadhyayula, G. V. Rogachev, J. Bishop, V. Z. Goldberg, J. Hooker, C. Hunt, H. Jayatissa, E. Koshchiy, E. Uberseder, A. Volya, B. T. Roeder, and A. Saastamoinen, "Search for the high-spin members of the α:2n:α band in ^{10}Be," *Physical Review C*, vol. 101, Mar. 2020.

[53] W. R. Leo, *Techniques for nuclear and particle physics experiments: a how-to approach*. New York, NY: Springer, 2nd ed., 1994.

[54] F. Hartmann, *Evolution of Silicon Sensor Technology in Particle Physics*. Cham, Switzerland: Springer International PU, 2nd ed., 2018.

[55] U. Fano, "Ionization yield of radiations. II. the fluctuations of the number of ions," *Physical Review*, vol. 72, pp. 26–29, July 1947.

[56] R. C. Alig, S. Bloom, and C. W. Struck, "Scattering by ionization and phonon emission in semiconductors," *Physical Review B*, vol. 22, pp. 5565–5582, Dec. 1980.

[57] H. Spieler, *Semiconductor Detectors Part II*. 1999.

[58] R. Brun and F. Rademakers, "Root an object oriented data analysis framework," *Nuclear Instruments and Methods in Physics Research Section A: Accelerators, Spectrometers, Detectors and Associated Equipment*, vol. 389, no. 1-2, p. 8186, 1997.

[59] J. Hooker. Private communication.

[60] S. Agostinelli *et al.*, "Geant4—a simulation toolkit," *Nuclear Instruments and Methods in Physics Research Section A: Accelerators, Spectrometers, Detectors and Associated Equipment*, vol. 506, pp. 250–303, July 2003.

[61] E. D. Johnson, *The Cluster Structure of Oxygen Isotopes*. PhD thesis, Florida State University, Tallahassee, FL, 2008.

[62] R. E. Azuma, E. Uberseder, E. C. Simpson, C. R. Brune, H. Costantini, R. J. de Boer, J. Görres, M. Heil, P. J. LeBlanc, C. Ugalde, and M. Wiescher, "Azure: An r-matrix code for nuclear astrophysics," *Physical Review C*, vol. 81, p. 045805, Apr 2010.

[63] H. G. Essel, H. Grein, T. Kroll, W. Kynast, M. Richter, H. Sohlbach, W. Spreng, K. Winkelmann, and W. F. J. Muller, "Goosy, the new gsi acquisition and analysis system for experiment data," *IEEE Transactions on Nuclear Science*, vol. 34, pp. 907–911, Aug 1987.

[64] H. Bethe and J. Ashkin, *Experimental Nuclear Physics*. New York, NY: Wiley, 1953.